A&A, 691, A203 (2024)
https://doi.org/10.1051/0004-6361/202450567

Astronomy & Astrophysics

BASS

XLIII. Optical, UV, and X-ray emission properties of unobscured *Swift*/BAT active galactic nuclei

Kriti K. Gupta[1,2,3,⋆], Claudio Ricci[1,4], Matthew J. Temple[1], Alessia Tortosa[5], Michael J. Koss[6,7], Roberto J. Assef[1], Franz E. Bauer[8,9], Richard Mushotzky[10], Federica Ricci[5,11], Yoshihiro Ueda[12], Alejandra F. Rojas[1,13], Benny Trakhtenbrot[14], Chin-Shin Chang[15], Kyuseok Oh[16], Ruancun Li[4,17], Taiki Kawamuro[18], Yaherlyn Diaz[1], Meredith C. Powell[19,20], Daniel Stern[21], C. Megan Urry[22], Fiona Harrison[23], and Brad Cenko[24]

[1] Instituto de Estudios Astrofísicos, Facultad de Ingeniería y Ciencias, Universidad Diego Portales, Av. Ejército Libertador 441, Santiago, Chile
[2] STAR Institute, Liège Université, Quartier Agora - Allée du six Août, 19c, B-4000 Liège, Belgium
[3] Sterrenkundig Observatorium, Universiteit Gent, Krijgslaan 281 S9, B-9000 Gent, Belgium
[4] Kavli Institute for Astronomy and Astrophysics, Peking University, Beijing 100871, PR China
[5] INAF – Osservatorio Astronomico di Roma, via di Frascati 33, I-00078 Monte Porzio Catone, Italy
[6] Eureka Scientific, 2452 Delmer Street Suite 100, Oakland, CA 94602-3017, USA
[7] Space Science Institute, 4750 Walnut Street, Suite 205, Boulder, CO 80301, USA
[8] Instituto de Astrofísica and Centro de Astroingeniería, Facultad de Física, Pontificia Universidad Católica de Chile, Campus San Joaquin, Av. Vicuña Mackenna 4860, Macul Santiago 7820436, Chile
[9] Millennium Institute of Astrophysics, Nuncio Monseñor Sótero Sanz 100, Of 104, Providencia, Santiago, Chile
[10] Department of Astronomy and Joint Space-Science Institute, University of Maryland, College Park, MD 20742, USA
[11] Dipartimento di Matematica e Fisica, Universita Roma Tre, via della Vasca Navale 84, I-00146 Roma, Italy
[12] Department of Astronomy, Kyoto University, Kitashirakawa-Oiwake-cho, Sakyo-ku, Kyoto 606-8502, Japan
[13] Centro de Astronomía (CITEVA), Universidad de Antofagasta, Avenida Angamos 601, Antofagasta, Chile
[14] School of Physics and Astronomy, Tel Aviv University, Tel Aviv 69978, Israel
[15] Joint ALMA Observatory, Avenida Alonso de Cordova 3107, Vitacura 7630355, Santiago, Chile
[16] Korea Astronomy & Space Science institute, 776, Daedeokdae-ro, Yuseong-gu, Daejeon 34055, Republic of Korea
[17] Department of Earth and Space Science, Graduate School of Science, Osaka University, 1-1 Machikaneyama, Toyonaka, Osaka 560-0043, Japan
[18] 6 RIKEN Cluster for Pioneering Research, 2-1 Hirosawa, Wako, Saitama 351-0198, Japan
[19] Kavli Institute for Particle Astrophysics and Cosmology, Stanford University, 452 Lomita Mall, Stanford, CA 94305, USA
[20] Department of Physics, Stanford University, 382 Via Pueblo Mall, Stanford, CA 94305, USA
[21] Jet Propulsion Laboratory, California Institute of Technology, 4800 Oak Grove Drive, MS 169-224, Pasadena, CA 91109, USA
[22] Yale Center for Astronomy & Astrophysics, Physics Department, PO Box 208120, New Haven, CT 06520-8120, USA
[23] Cahill Center for Astronomy and Astrophysics, California Institute of Technology, Pasadena, CA 91125, USA
[24] Astrophysics Science Division, NASA Goddard Space Flight Center, Mail Code 661, Greenbelt, MD 20771, USA

Received 30 April 2024 / Accepted 4 September 2024

ABSTRACT

We present one of the largest multiwavelength studies of simultaneous optical-to-X-ray spectral energy distributions (SEDs) of unobscured ($N_H < 10^{22}$ cm^{-2}) active galactic nuclei (AGN) in the local Universe. Using a representative sample of hard-X-ray-selected AGN from the 70-month *Swift*/BAT catalog, with optical/UV photometric data from *Swift*/UVOT and X-ray spectral data from *Swift*/XRT, we constructed broadband SEDs of 236 nearby AGN ($0.001 < z < 0.3$). We employed GALFIT to estimate host galaxy contamination in the optical/UV and determine the intrinsic AGN fluxes. We used an absorbed power law with a reflection component to model the X-ray spectra and a dust-reddened multi-temperature blackbody to fit the optical/UV SED. We calculated intrinsic luminosities at multiple wavelengths, total bolometric luminosities (L_{bol}), optical-to-X-ray spectral indices (α_{ox}), and multiple bolometric corrections (κ_λ) in the optical, UV, and X-rays. We used black hole masses obtained by reverberation mapping and the virial method to estimate Eddington ratios (λ_{Edd}) for all our AGN. We confirm the tight correlation (scatter = 0.45 dex) between UV (2500 Å) and X-ray (2 keV) luminosity for our sample. We observe a significant decrease in α_{ox} with L_{bol} and λ_{Edd}, suggesting that brighter sources emit more UV photons per X-rays. We report a second-order regression relation (scatter = 0.15 dex) between the 2–10 keV bolometric correction (κ_{2-10}) and α_{ox}, which is useful to compute L_{bol} in the absence of multiband SEDs. We also investigate the dependence of optical/UV bolometric corrections on the physical properties of AGN and obtain a significant increase in the UV bolometric corrections (κ_{W2} and κ_{M2}) with L_{bol} and λ_{Edd}, unlike those in the optical (κ_V and κ_B), which are constant across five orders of L_{bol} and λ_{Edd}. We obtain significant dispersions (∼0.1–1 dex) in all bolometric corrections, and hence recommend using appropriate relations with observed quantities while including the reported scatter, instead of their median values.

Key words. black hole physics – catalogs – surveys – galaxies: active – galaxies: nuclei – quasars: supermassive black holes

⋆ Corresponding author; kkgupta@uliege.be

1. Introduction

Supermassive black holes (SMBHs) are present at the center of almost all massive galaxies (e.g., Kormendy & Richstone 1995). However, only a fraction of these galaxies are observed as active galactic nuclei (AGN), when the central SMBH is in an actively accreting phase. While most of the light coming from a galaxy can be typically attributed to its stellar population that mainly emits radiations from the ultraviolet (e.g., Kinney et al. 1993) to the near-infrared bands, AGN are characterized by their multiwavelength emission spanning the entire electromagnetic spectrum (e.g., Padovani et al. 2017). This multiwavelength emission is generated in different regions of the AGN via various physical processes (e.g., Netzer 2013). The AGN is fueled by the accretion of the surrounding material onto the central SMBH in the form of a disk emitting optical/UV photons. A fraction of these photons can be either absorbed by the dusty torus surrounding the AGN (e.g., Antonucci 1993) and re-emitted in the infrared (IR) or Comptonized by a corona of hot electrons located close to the SMBH, giving rise to high-energy X-ray radiation (e.g., Haardt & Maraschi 1991).

A detailed analysis of the broadband spectral energy distributions (SEDs) of a representative sample of AGN can therefore provide useful insights into the various physical processes at play in the inner regions of AGN, which are otherwise difficult to image with current observational facilities. The AGN SEDs can further be used to investigate relations between emissions at different wavelengths originating in different regions of the SMBH. Additionally, a complete and consistent study of broadband AGN SEDs can be used to constrain AGN accretion models and compute several important quantities such as luminosities in various energy bands (L_λ), optical to X-ray spectral indices (α_{ox}), bolometric luminosities (L_{bol}), mass accretion rates ($\dot{M}_{acc}$), and Eddington ratios (λ_{Edd}) (e.g., Vasudevan & Fabian 2009; Vasudevan et al. 2010; Lusso et al. 2012; Marshall et al. 2022; Mitchell et al. 2023). Moreover, one can also estimate what fraction of the total luminosity of the AGN is emitted at different wavelengths, in terms of bolometric corrections ($\kappa_\lambda = L_{bol}/L_\lambda$; e.g., Marconi et al. 2004; Lusso et al. 2010; Duras et al. 2020; Saccheo et al. 2023; Setoguchi et al. 2023). These bolometric correction factors can be extremely useful when we do not have access to multiwavelength data, as they estimate the total luminosity emitted by an AGN and their Eddington ratios ($\lambda_{Edd} = L_{bol}/L_{Edd}$; $L_{Edd} \propto M_{BH}$). They are widely employed by the scientific community to constrain the accretion history of SMBHs from AGN luminosity functions (e.g., Ueda et al. 2003; Ananna et al. 2020). However, the construction and fitting of AGN SEDs is not trivial and must consider several key points, including:

Effects of obscuration: AGN are majorly classified into two types: type I and type II, based on the presence and absence of broad Balmer emission lines in their optical spectra. According to the unified AGN model, these two classes of AGN are fundamentally similar and their observed optical properties simply reflect their different viewing angles (e.g., Urry & Padovani 1995). Type I AGN are viewed face-on, and hence are less affected by obscuration in the line of sight of the observer, whereas type II AGN are viewed edge-on, through the dusty toroidal structure, due to which the broad optical emission lines are missing in their spectra. Consequently, the SEDs of these two classes of AGN have different shapes, with the type IIs showing higher levels of absorption, which needs to be considered when doing a comprehensive study of AGN SEDs (e.g., Lusso et al. 2012; Duras et al. 2020).

Host galaxy contamination: While analyzing multiband AGN SEDs, one needs to include the contribution from the host galaxy, especially in the optical and UV energy bands, where one can expect mild to severe contamination from the host galaxy light. This contamination can be particularly important in low-luminosity AGN (e.g., Ho 2008). Therefore, to get reliable measurements of the total AGN luminosity, one must separate the AGN light from the host galaxy light. Over the years, different works have employed different approaches to handle host galaxy contamination in their SED fitting, based on their specific science goals. Some of these techniques remove the host galaxy light before the SED fitting, either by using an image decomposition software like GALFIT (e.g., Vasudevan & Fabian 2009; Shang et al. 2011), or by using empirical correction factors based on quantities like the 4000 Å break (e.g., Marchese et al. 2012) or the 5100 Å luminosity (e.g., Saccheo et al. 2023). Others follow a different approach, fitting the entire SED with galaxy + AGN templates to also extract the host galaxy properties (e.g., Assef et al. 2010; Lusso et al. 2012; Duras et al. 2020; Marshall et al. 2022; Setoguchi et al. 2023).

Galactic dust extinction: While studying the SEDs of distant objects, one also needs to take into account Galactic extinction. This is usually handled by including different dust extinction curves during the fitting process like the Cardelli et al. (1989) extinction curve (e.g., Shang et al. 2011), and the Calzetti et al. (2000) reddening curve (e.g., Duras et al. 2020). Additionally, intrinsic extinction at the redshift of the source, due to the host galaxy, can also affect the final estimates of the AGN luminosity and must be included accordingly (e.g., Temple et al. 2021).

Variability: AGN show variability across all wavelengths, with timescales that can range from hours to days to years (e.g., Ulrich et al. 1997). Since the multiwavelength emission in AGN originates in different regions of the AGN located at different physical scales (the optical/UV arising from the sub-parsec accretion disk and the X-rays originating much closer to the central SMBH), they may show uncorrelated variability with distinct intensities and time. These flux variations can have large amplitudes and be associated with strong spectral variability (e.g., Ricci & Trakhtenbrot 2023 and references therein). Hence, to get a consistent picture of the total emission from the AGN at a certain time, simultaneous observations in different bands are required to minimize the effect of variability and to construct well-defined broadband SEDs of AGN. However, due to the difficulties associated with obtaining simultaneous observations, most of the previous studies of AGN SEDs have either included an error term to account for the effects of variability in the SED (e.g., Marchese et al. 2012) or used quasi-simultaneous observations (e.g., Shang et al. 2011; Runnoe et al. 2012a) to limit their impact.

The first large, high-quality atlas of quasar (high-luminosity AGN) SEDs over the whole accessible range of the electromagnetic spectrum, from radio to X-rays, was reported by Elvis et al. (1994). They calculated the bolometric luminosity for their sample by integrating over the full SED, and derived mean bolometric corrections in different bands. Following this milestone work, many significant contributions were made to the investigation of multiwavelength SEDs of AGN by treating the selection effects of Elvis et al. (1994) in the X-rays and removing the contribution of the reprocessed IR emission in the total accretion luminosity of AGN (e.g., Kuraszkiewicz et al. 2003; Risaliti & Elvis 2004; Marconi et al. 2004; Richards et al. 2006). Vasudevan & Fabian (2009) and Vasudevan et al. (2009) used simultaneous data to study optical to X-ray SEDs of (~30) nearby type I AGN. They successfully estimated the 2–10 keV

bolometric corrections (κ_{2-10}) for their sample and found a strong dependence of κ_{2-10} on the Eddington ratio. A tight correlation between α_{ox} and κ_{2-10} was reported by Lusso et al. (2010), which can be employed to estimate bolometric corrections using only optical and X-ray data. While most of the SED studies in the early 2000s (e.g., Marchese et al. 2012; Runnoe et al. 2012a,b; Krawczyk et al. 2013) primarily focused on calculating bolometric corrections for type I AGN, Lusso et al. (2012) analyzed a sample of both type I and type II AGN and derived their bolometric luminosities and corrections, confirming the dependence of κ_x on λ_{Edd} for both classes of AGN. Additionally, Brightman et al. (2017) presented X-ray bolometric corrections for Compton-thick AGN ($N_H > 10^{24}$ cm^{-2}). More recently, Duras et al. (2020) analyzed ∼1000 AGN SEDs, including both type Is and type IIs, and found that while the X-ray bolometric correction is correlated with L_{bol}, λ_{Edd} and M_{BH}, the optical bolometric correction tends to remain constant with all these parameters.

In this work, we perform a comprehensive multiwavelength study of a large sample of nearby ($z < 0.1$) unobscured ($N_H < 10^{22}$ cm^{-2}), hard-X-ray-selected type I AGN, with the goal of shedding light on AGN accretion. This was done by creating and modeling optical-to-X-ray SEDs of a sample of 236 *Swift*/BAT-detected AGN using simultaneous optical, UV, and X-ray data. A similar effort was made by Vasudevan et al. (2009), who fit the optical-to-X-ray SEDs of 26 hard-X-ray-selected AGN and reported their X-ray bolometric corrections. More than ten years later, we have successfully improved the sample size by 1 dex. To date, this is one of the largest samples of hard-X-ray-selected AGN for which such an analysis has been carried out in a consistent way. We have also refined the GALFIT-based AGN-galaxy decomposition using simulations and upgraded the SED fitting procedure. Based on our analysis, in this paper, we present multiwavelength fluxes and luminosities, along with estimates of L_{bol}, λ_{Edd}, α_{ox}, and κ_λ at multiple energies for our AGN sample. We also discuss some important correlations between these quantities that help us better understand the accretion physics of unobscured AGN in the local Universe.

The structure of the paper is as follows. In Sect. 2, we describe the sample used in this work, while in Sect. 3 we illustrate the data reduction process for the optical/UV (Sect. 3.1) and X-ray data (Sect. 3.2). In Sects. 4 and 5, we explain the fitting analysis of the X-ray spectra and the image decomposition of the optical/UV images to correct for host galaxy contamination, respectively. Section 6 describes in detail the broadband SED fitting procedure. Finally, in Sects. 7 and 8, we present and summarize our main results, including the optical-to-X-ray spectral indices and the X-ray, optical, and UV bolometric corrections over a large range of Eddington ratios [$-5.0 < \log(\lambda_{Edd}) < 0.0$]. We also report the main correlations found for these quantities with various physical properties of AGN, such as their black hole mass, bolometric luminosity, and Eddington ratio. Throughout the paper, we assume a cosmological model with $H_0 = 70$ km s^{-1} Mpc^{-1}, $\Omega_M = 0.3$, and $\Omega_\Lambda = 0.7$. Images are shown adopting the standard astronomical orientation; that is, north is up and east is left. All magnitudes quoted throughout the text are AB magnitudes. All errors and uncertainties listed in the tables or shown as error bars or shaded regions in the figures are one sigma, unless otherwise stated. All the correlations were obtained using various functions from the `statistics`[1] module of the Python library `scipy` (Virtanen et al. 2020) and the Python package `linmix`[2] (Kelly 2007).

[1] https://docs.scipy.org/doc/scipy/reference/stats.html
[2] https://linmix.readthedocs.io/en/latest/

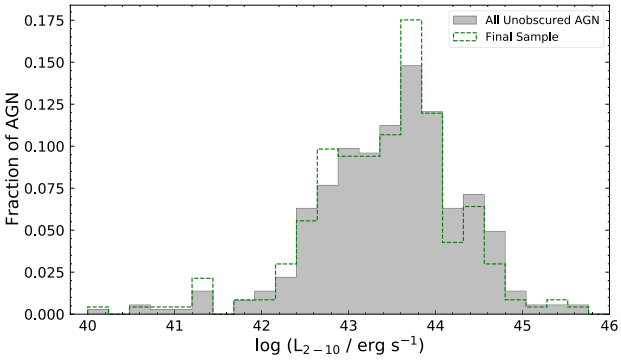

(a)

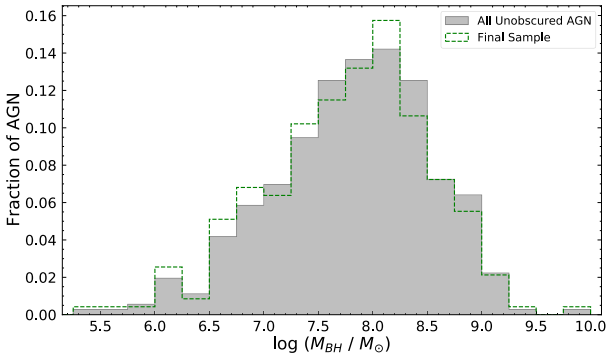

(b)

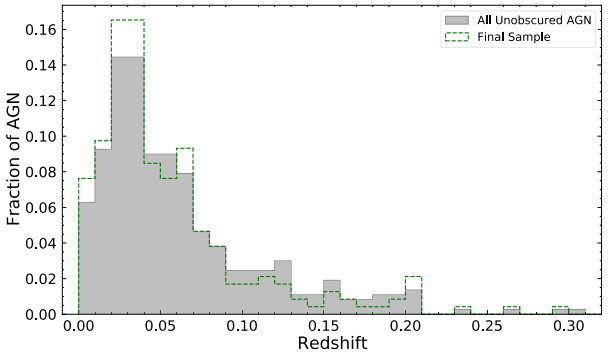

(c)

Fig. 1. Distribution of the (a) 2–10 keV intrinsic X-ray luminosity, (b) black hole mass, and (c) redshift of the total sample of unobscured *Swift*/BAT AGN (in gray) and our final sample of 236 unobscured AGN (dashed green histogram). The figures show that our sample covers the parameter space probed by the full unobscured *Swift*/BAT AGN sample, in terms of redshift, black hole mass, and luminosity.

2. Sample

Unlike the optical/UV and soft X-ray radiation ($E < 10$ keV), which are highly sensitive to extinction by the circumnuclear and interstellar dust, the hard X-rays ($E > 10$ keV) are much less affected by obscuration (up to $N_H \sim 10^{24}$ cm^{-2}; see Fig. 1 of Ricci et al. 2015) due to their high penetration power. They are also less contaminated by stellar emission from the host galaxy and can therefore be used to obtain a more complete and unbiased sample of AGN, including the most

obscured sources, which could be missed by optical/UV surveys. In this work, we use a sample of hard-X-ray-selected AGN detected in the 14–195 keV band by the Burst Alert Telescope (BAT: Barthelmy et al. 2005; Krimm et al. 2013) on board NASA's *Neil Gehrels Swift* Observatory. *Swift* is a multiwavelength space observatory with two additional instruments: the X-ray Telescope (XRT; Burrows et al. 2005) operates in the 0.3–10 keV energy range, while the UV/Optical Telescope (UVOT; Poole et al. 2008; Breeveld et al. 2010) observes the sky in six filters spanning 170–650 nm. Most of the sources detected by BAT in the hard X-rays have eventually been simultaneously observed (over ∼2 days) in the soft X-rays by *Swift*/XRT and in the optical/UV band by *Swift*/UVOT. A systematic multiwavelength study of all the *Swift*/BAT AGN has been carried out by the BAT AGN Spectroscopic Survey (BASS[3]). BASS recently published their second data release (DR2; Koss et al. 2022a) with a complete, optical spectroscopic analysis of all the 858 *Swift*/BAT AGN in the 70-month catalog (Koss et al. 2022b), thanks to a dedicated campaign. BASS also provides a comprehensive study of *Swift*/BAT AGN in the X-rays (Ricci et al. 2017), near-IR (Lamperti et al. 2017), mid-IR (Ichikawa et al. 2019), millimeter (Kawamuro et al. 2022; Ricci et al. 2023), and radio (Baek et al. 2019). Other data products from this release include measurements of the broad emission lines (Mejía-Restrepo et al. 2022), narrow emission lines (Oh et al. 2022), velocity dispersions (Koss et al. 2022c), and NIR spectral properties (Ricci et al. 2022; den Brok et al. 2022).

In this study, we use the 70-month *Swift*/BAT catalog (Baumgartner et al. 2013), consisting of 858 hard-X-ray-selected local (median redshift, $z = 0.037$) AGN. We focus on unobscured AGN to mitigate host galaxy contamination and carefully study the very central optical and UV emission associated with the AGN. We start with an X-ray-selected sample of unobscured AGN to have minimum obscuration due to the material in the line of sight, and to do so we use the X-ray column densities ($N_{\rm H}$). As part of the first data release (DR1) of BASS, Ricci et al. (2017; hereafter R17) performed a detailed X-ray spectral analysis of all BAT AGN and reported the $N_{\rm H}$ values for 836/858 sources. For our primary sample, we shortlist all AGN with $N_{\rm H} < 10^{22}$ cm^{-2}, which gives us a set of 367 unobscured AGN. This sample excludes the sources that are flagged as blazars following the classification presented in Koss et al. (2022b) based on the Roma Blazar Catalog (BZCAT; Massaro et al. 2009) and the study done by Paliya et al. (2019). We also have black hole mass estimates for most of these sources from the BASS DR2 (Mejía-Restrepo et al. 2022).

We used the HEASARC archive[4] to compile the available *Swift* observations for our AGN sample. To obtain the best possible estimates of the optical/UV fluxes, we used the observation with maximum exposure and coverage in all the six *Swift*/UVOT filters (V, B, U, UVW1, UVM2, and UVW2; see Table 1). A total of 226/367 (∼62%) sources had *Swift* observations in all UVOT filters plus simultaneous *Swift*/XRT observations. For the remaining 141 (∼38%) sources, we checked for *Swift* observations with maximum wavelength coverage. 67/141 (∼47%) sources had *Swift* observations with at least one optical and one UV filter, and simultaneous X-ray observations. In total, we recovered 293/367 (∼80%) sources (see Table A.1) with simultaneous optical/UV and X-ray observations (Table A.2) that can be used to extract multiwavelength fluxes and construct optical-to-X-ray SEDs, with ∼76% of these sources having observations in all *Swift*/UVOT filters. We performed the broadband SED fitting for a final sample of 236/293 (∼80%) sources, after removing (i) two sources with strong contamination from a nearby source affecting the optical/UV or X-ray data extraction (discussed in Sect. 3), (ii) one source with a strongly variable X-ray spectrum (see Sect. 4), and (iii) 54 sources with fewer than four points in the optical/UV wavebands making them unsuitable for the SED fitting (explained in detail in Sect. 6). We show the range of redshift, black hole mass, and X-ray luminosity covered by our final sample, as well as by the total unobscured, *Swift*/BAT AGN sample in Fig. 1. Our sample is representative of the *Swift*/BAT parent sample in terms of black hole mass, luminosity and redshift, as it covers the same ranges for these parameters as the original *Swift*/BAT sample.

3. Data reduction

3.1. Optical/UV photometric data from Swift/UVOT

The reduction and analysis of the *Swift*/UVOT data for our sample of unobscured AGN was done following the steps recommended by the *Swift*/UVOT Software Guide Version 2.2[5] (released in March 2008). Although the calibrated and pipeline processed images are available in the archive for all our sources, to take into account the possible changes in the data analysis due to the 2020 update in the *Swift* calibration database[6] (CALDB), we recreated the fully calibrated images from the raw images for all the sources in our sample. The final sky images were eventually used to extract the flux and magnitudes of the sources. We only used image or event files in the pointing mode. We started with the raw image HDUs in each filter provided in the HEASARC archive and created the corresponding bad pixel maps using the latest UVOT CALDB (`uvotbadpix`). Next, flat field images were created for each filter using the attitude file and CALDB (`uvotflatfield`). The bad pixel maps and the flat field images were both used to create the sky images in each filter (`swiftxform`). One must note that some raw images might consist of multiple image HDUs corresponding to multiple exposures in the same filter that need to be summed to get the final, deeper image. In the case of single HDUs, the resultant sky image was used to extract the source and sky region with radii of ∼5 and ∼20 arcseconds, respectively, to obtain the source and background fluxes, magnitudes, and errors (`uvotsource`). The size of the regions is based on the average curves of growth[7] of the UVOT point spread function (PSF) for the six UVOT filters. For source images with crowded fields, smaller background regions (∼10″) were selected. In the case of multiple image HDUs corresponding to multiple exposures in the same filter, all the image HDUs were first aspect-corrected (`uvotskycorr`) and then summed using the `uvotimsum` tool to create the final, deeper image. These images were all visually inspected to make sure that the source of interest was perfectly aligned. The summed images were then used to extract the source and background regions, as is illustrated above, in order to get the source and background fluxes and magnitudes along with statistical errors. The `uvotsource` command includes corrections for coincidence loss, which can become significant for

[3] www.bass-survey.com
[4] https://heasarc.gsfc.nasa.gov/cgi-bin/W3Browse/w3browse.pl
[5] https://swift.gsfc.nasa.gov/analysis/UVOT_swguide_v2_2.pdf
[6] https://heasarc.gsfc.nasa.gov/docs/heasarc/caldb/swift/
[7] https://heasarc.gsfc.nasa.gov/docs/heasarc/caldb/swift/docs/uvot/uvot_caldb_psf_02.pdf

Table 1. Characteristics of *Swift*/UVOT filters.

Filter	Central Wavelength (Å)	FWHM (Å)	AB Zero-point [(a)] (mag)	Counts to Flux (F_λ) Ratio (10^{-16} erg count^{-1} cm^{-2} Å^{-1})
UVW2	1928	657	19.11 ± 0.03	6.225 ± 0.1300
UVM2	2246	498	18.54 ± 0.03	8.489 ± 0.0530
UVW1	2600	693	18.95 ± 0.03	4.623 ± 0.1400
U	3465	785	19.36 ± 0.02	1.663 ± 0.0250
B	4392	975	18.98 ± 0.02	1.480 ± 0.0056
V	5468	769	17.88 ± 0.01	2.611 ± 0.0087

Notes. The central wavelength corresponds to the mid-point between the wavelengths at the full width at half maximum (FWHM). The zero-point magnitude represents the magnitude of a source producing one count per second. [(a)]https://heasarc.gsfc.nasa.gov/docs/heasarc/caldb/swift/docs/uvot/uvot_caldb_AB_10wa.pdf

sources with fluxes >20 counts s^{-1}. All the source fluxes and magnitudes thus measured are listed in Tables A.3 and A.4 and their distributions are shown in Fig. 2a. The systematic uncertainties in the flux values are ∼1.5% and always smaller than the reported statistical errors.

One source in our sample, SWIFTJ1940.4-3015 (BAT ID = 1045), has a V = 11.3 magnitude star (CD-30 17265) close to it (distance between centroids = 11.2″). Due to strong contamination from the star within the 5″ region of our source of interest, we are unable to extract reliable fluxes for this source in any of the *Swift*/UVOT filters. Moving forward, we have removed this source from our sample, which now consists of 292 sources.

3.2. X-ray spectroscopic data from Swift/XRT

We downloaded the level 2 *Swift*/XRT event files in photon counting mode from the HEASARC archive to extract the X-ray spectra for our sources. Following the standard procedures reported in the *Swift*/XRT Data Reduction Guide Version 1.2[8] (April 2005), we used the `xselect` package to select, from the event files, circular source and annular background regions with radii of ∼50 and ∼150 arcseconds, respectively. For context, 90% of the XRT PSF at 1.5 keV is enclosed by a circular region of ∼47″. These regions were then used to extract the source and background spectra. The `xrtmkarf` tool was used to create the ARF (ancillary response file) and get the RMF (response matrix file). The source spectra were binned, using `grppha`, with a minimum of one count/bin. All the source spectra were visually examined to check that the background counts were overall lower than the source counts.

One AGN in our sample, SWIFTJ1043.4+1105 (BAT ID = 512), has strong contamination from an unidentified nearby X-ray source (within 18″). Therefore, we decided to remove this source from our sample, giving us an updated sample size of 291 sources.

4. X-ray spectral fitting

In this section, we describe in detail the fitting procedure for the 0.3–10 keV X-ray spectra of the sources in our sample. A detailed broadband X-ray (0.3–150 keV) spectral analysis of 836 AGN in the 70-month *Swift*/BAT catalog was carried out using XSPEC (Arnaud 1996) as part of the BASS DR1 and is presented in R17. Following their analysis, we employed the models they used to fit the unobscured AGN in their catalog to fit the AGN in our sample. We used models A1 and A2, which were used by R17 to fit most (∼77%) of the unobscured AGN in their sample. These two models are defined as follows:

- Model A1 ($\texttt{TBABS}_{\texttt{Gal}} \times \texttt{ZPHABS} \times \texttt{CABS} \times \texttt{PEXRAV}$): This model has a component that accounts for the primary X-ray emission along with reflection by optically thick, neutral circumnuclear material (`PEXRAV`; Magdziarz & Zdziarski 1995). It also includes Galactic absorption ($\texttt{TBABS}_{\texttt{Gal}}$), and absorption by neutral material via photoelectric absorption (`ZPHABS`) and Compton scattering (`CABS`).
- Model A2 [$\texttt{TBABS}_{\texttt{Gal}} \times \texttt{ZPHABS} \times \texttt{CABS} \times (\texttt{PEXRAV} + \texttt{BB})$]: This model is the same as model A1 with an additional blackbody component (`BB`) to account for the soft excess.

We began the fitting for the 291 sources in our sample by using the best-fit values estimated by R17 as starting values for most of the model parameters. These include $N_{\rm H}$ for `ZPHABS` and `CABS`, photon index (Γ), high-energy cutoff ($E_{\rm c}$), and a reflection parameter (R) for `PEXRAV`, and the temperature ($kT_{\rm bb}$) of the `BB` component. In the cases where values for R, $E_{\rm c}$, or $kT_{\rm bb}$ were not reported by R17, either because they were not constrained or because a different model was used to fit the source, we used as starting values R = 0.0, $E_{\rm c}$ = 200 keV, and $kT_{\rm bb}$ = 0.1 keV, respectively. The redshift parameter for both `ZPHABS` and `PEXRAV` was fixed using the values reported in Koss et al. 2022b. The inclination was fixed to 30°, the metallicity (Z) was fixed to solar, and the iron abundance was fixed at its default value, as was done in R17. The $E_{\rm c}$ and R parameters were also frozen to the values reported by R17. Hence, only the column density (which was tied to have the same value for `ZPHABS` and `CABS`), the photon index, and the normalization ($K_{\rm x}$: for `PEXRAV`) were free parameters in the fitting process. The $N_{\rm H}$ for Galactic absorption was also fixed at the value obtained at the coordinate of the source from the HI 4-PI Survey (HI4PI; HI4PI Collaboration 2016), a 21-cm all-sky survey of neutral atomic Hydrogen. In the case of model A2, the temperature ($kT_{\rm bb}$) and normalization ($K_{\rm bb}$) of the blackbody component were allowed to vary during the fitting.

The spectra were fit using Cash statistics (C-stat; Cash 1979). The best-fit values of all free parameters were checked using the `steppar` command in XSPEC. Additionally, the 90% confidence intervals for all parameters were estimated using the `error` command in XSPEC. All the fit residuals were visually inspected and for ∼90% of the sources we obtained good fits (see Table A.5 for goodness of each fit) using either model A1 or A2. For the remaining 10% of the sources, we investigated the best-fit model and the fits individually. In some cases (∼7%), a component to account for absorption by ionized gas, `ZXIPCF` (Reeves et al. 2008), was added to the model to improve

[8] https://swift.gsfc.nasa.gov/analysis/xrt_swguide_v1_2.pdf

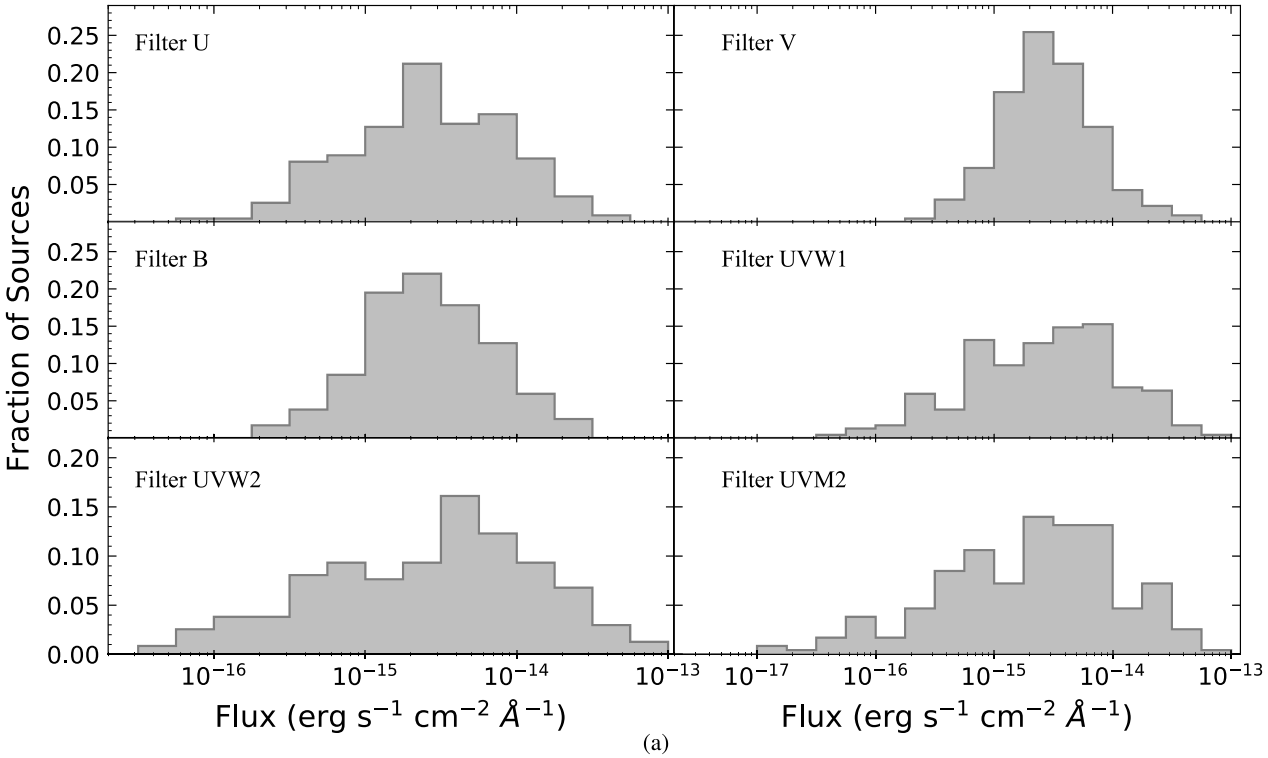

(a)

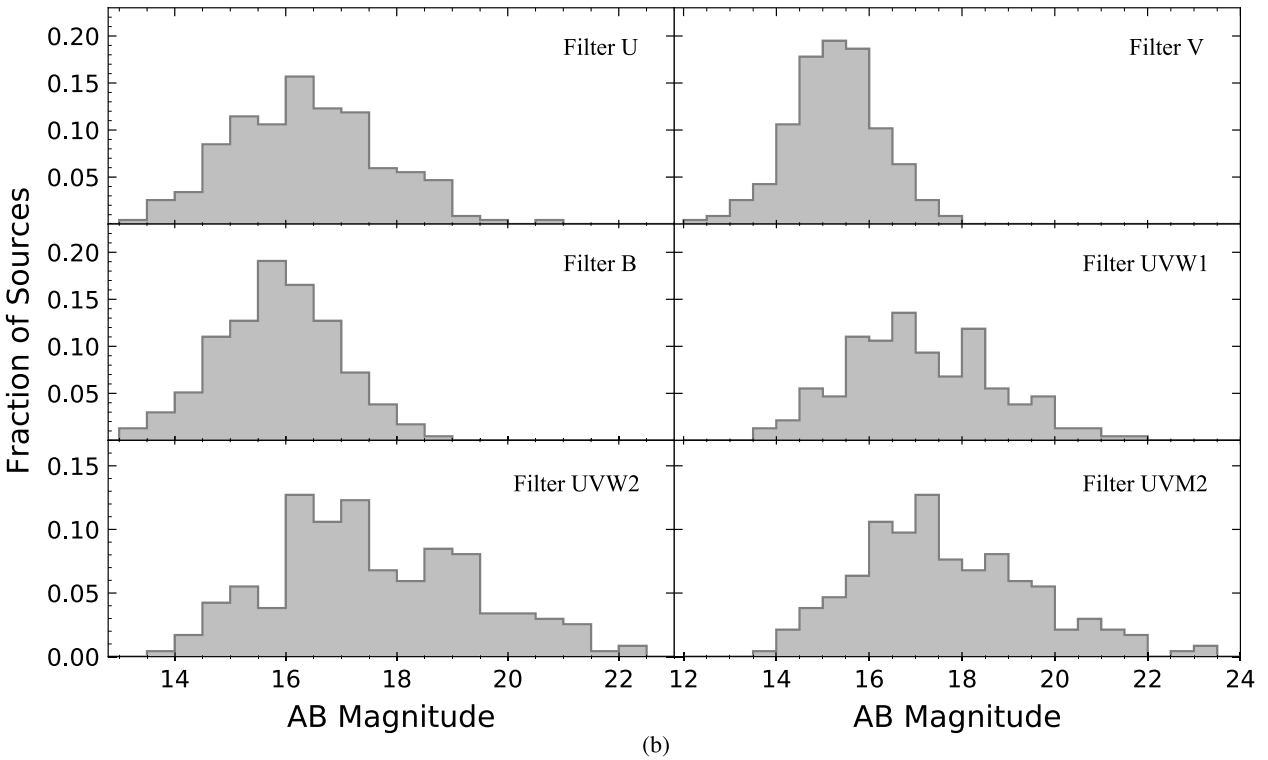

(b)

Fig. 2. Distribution of the source (a) fluxes and (b) AB magnitudes in the six *Swift*/UVOT filters estimated using aperture photometry for our sample of 292 AGN (Sect. 3.1).

the fits. This component assumes a partial covering geometry of a partially ionized warm absorber. The photon index and normalization of the power law along with the three parameters (column density [$N_{\rm H}^{\rm W}$], ionization parameter [ξ], and the covering factor [$f_{\rm cov}^{\rm W}$] of the warm absorber) corresponding to the ZXIPCF component were allowed to vary during the fitting. After the fitting, the best-fit values of all the free parameters were checked using the steppar command to avoid local minima in the fitting. One of the sources, SWIFTJ1844.5-6221 (BAT ID = 995; more commonly known as Fairall 51), is known to

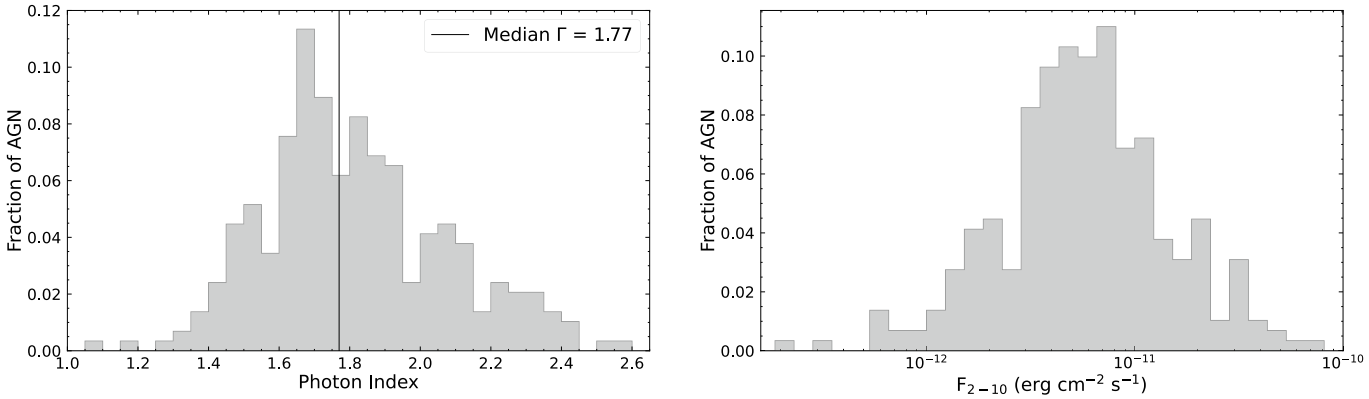

(a) (b)

Fig. 3. Outputs of the 0.3–10 keV X-ray spectral fitting (Sect. 4). (a) Distribution of the best-fit values of photon index (Γ). The vertical line marks the median value of Γ = 1.77. (b) Histogram of the intrinsic 2–10 keV flux for our AGN sample.

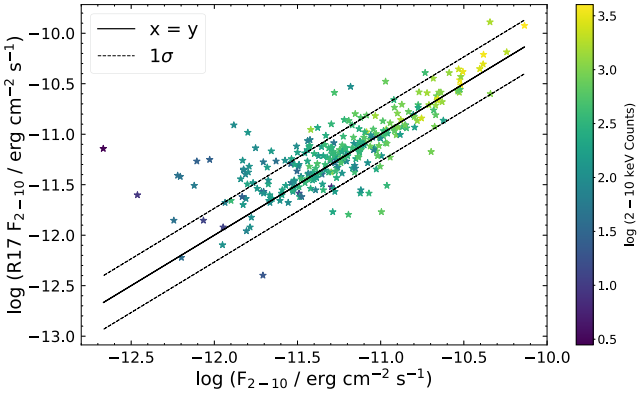

Fig. 4. Comparison between the 2–10 keV intrinsic flux we obtained and that obtained by R17 following a detailed broadband X-ray spectral analysis. The points are color-coded with the counts in the 2–10 keV energy range showing that the maximum offset with 1:1 line is observed in sources with least counts. The $x = y$ line is shown in black and the 1σ dispersion line is shown as a dashed black line. The typical uncertainties on F_{2-10} calculated from our work are less than 5%.

show spectral variability on small timescales, due to the presence of a variable absorber, probably located in the broad line region (BLR; see Svoboda et al. 2015 and references within). We found features of a possible changing-obscuration transition (e.g., Ricci & Trakhtenbrot 2023) in its spectrum with a very low photon index ($\Gamma \sim 0.4$). A detailed analysis of the X-ray spectrum of this object is beyond the scope of this work, so we decided to remove it from the final sample (updated sample size = 290). One source, SWIFTJ0335.4+1907 (BAT ID = 187), was fit using just a power law due to a low number of counts. Four sources (SWIFTJ0021.2-1909, SWIFTJ0945.6-1420, SWIFTJ1334.8-2328D2, and SWIFTJ1345.5+4139) showed signatures of strong obscuration in their spectra, corresponding to them being at the high end of the column density distribution of our sample. Hence, for these sources, we used model B1 from R17, which was specifically used to fit obscured sources. This model consists of additional components to account for the reprocessed primary X-ray emission and Thomson-scattered X-ray radiation (e.g., Gupta et al. 2021; McKaig et al. 2023).

For all objects, we obtained the best-fit values for parameters including the photon index (Fig. 3a) and normalization of the primary power law, line-of-sight column density of the neutral material responsible for absorption, and temperature and normalization of the blackbody component (see Table A.5), from the X-ray spectral fits. To ensure that our results were consistent with those reported by R17, we compared the best-fit values of Γ of the primary power law and obtained a linear relation with a dispersion of 0.2 dex, expected due to variability. We calculated the observed and intrinsic (rest-frame and absorption-corrected) 2–10 keV and 14–195 keV fluxes (Fig. 3b) and luminosities for all our sources. All luminosities were calculated using the best estimated distances (including redshift-independent distances) listed in Table A.1. The upper and lower uncertainties in the flux were estimated using the `cflux` command in XSPEC.

In Fig. 4, we show a comparison between the 2–10 keV fluxes from this work and those reported by R17 to confirm that we get similar values. We obtain a 1:1 correlation (shown as a black line) with a 0.2 dex dispersion (similar to Γ; shown as a dashed black line), which could be an effect of the variability in the X-rays between the time of the observation used in our analysis and those used by R17. The visible scatter also emphasizes the need for a new X-ray spectral analysis that is contemporaneous with the optical/UV data for this specific work. The points are color-coded with the 2–10 keV counts to show that the sources with maximum offset from the 1:1 line are indeed the ones with lower counts. The total X-ray luminosity (L_X; to be later combined with the optical/UV disk emission, to finally estimate the bolometric luminosity) was computed from the 0.1 to 500 keV energy range. The lower bound of this energy range was determined based on the X-ray spectrum generated by the thermal model `NTHCOMP` (Zdziarski et al. 1996; Życki et al. 1999), which describes the X-ray corona. We assumed a photon index of 1.8 (Ricci et al. 2018), coronal electron temperature (kT_e) of 100 keV (Ricci et al. 2018), and seed photon temperature (kT_{bb}) of 0.032 keV based on the median black hole mass ($\log [M_{BH}/M_\odot] = 7.9$) of our sample. The X-ray spectrum thus created shows a sharp drop at 0.1 keV, indicating the lack of significant X-ray emission beyond those energies.

5. AGN-galaxy image decomposition using GALFIT

When estimating the optical/UV fluxes and magnitudes for AGN, one needs to correct for contamination due to the host galaxy light. Even though our sample consists of nearby unobscured AGN, where the central AGN is typically brighter than the host galaxy at optical/UV wavelengths, the fluxes calculated

by selecting 5″ regions around the AGN can have a significant contribution from the host galaxy starlight. To obtain accurate measurements of the AGN flux devoid of any host galaxy light, we employed GALFIT[9] (Peng et al. 2002, 2010) to fit the 2D surface brightness profiles of the sources and decompose them into AGN and galaxy light. GALFIT is an image analysis tool that can be used to model light profiles of galaxies by separating them into different parts such as disk, bulge, and point source, and using different radial distributions like a PSF, Sérsic profile and Gaussian function, to fit them. For our analysis, we used a PSF profile to fit the AGN and a Sérsic profile to reproduce the host galaxy emission, if and when needed. The size of the *Swift*/UVOT PSF ranges between 2–3 arcseconds, which translates to physical scales of ~0.04–4 kpc for the redshift range of the sources in our sample. This is comparable to the typical sizes of bulge components of large galaxies (e.g., Freeman 2008), where most of the optical/UV emission can be attributed to the central AGN. For eight nearby sources with extended galaxy features, we adopted two Sérsic profiles to better estimate the AGN flux, while in most of the faintest sources, GALFIT was not able to fit a Sérsic profile to the images, and hence we only used the PSF profile to estimate their AGN flux. Due to the flux-limited nature of the *Swift*/BAT AGN sample, the sources with the lowest fluxes are also the farthest and appear more point-like in the images, and hence are suitable to be fit with a PSF profile due to their comparatively small host galaxy contamination. In all cases, a uniform background component was also included in the fits.

GALFIT consists of a function-fitting algorithm and gives the best-fit results based on least-squares statistics. Therefore, the user is expected to provide the necessary inputs needed to do the fitting. GALFIT requires a template file that consists of all the details about the input image, including the name and location of the image file, size of the image region to fit, bad-pixel mask, zero-point magnitude, and plate scale. GALFIT needs some specific information for the input source image and looks for these in the image header corresponding to the keywords EXPTIME (the exposure time), GAIN (electrons/counts), and NCOMBINE (number of images combined to create the source image). Therefore, the input image file has to be edited to include these keywords and their values in the image header. There is also the option to add a bad-pixel mask, which is useful to discard very nearby sources such as bright stars and stray objects contaminating the source of interest or its immediate surroundings.

If the user wishes to fit a PSF, they have to provide the PSF image as well as the PSF fine sampling factor relative to the data in this template file. Additionally, all the functions or profiles corresponding to different parts of the galaxy that the user wants to fit along with the initial values of their fitting parameters are also defined in this template file. The user can also specify if a particular parameter is fixed or free to vary during the fitting. In the next section (Sect. 5.1), we describe in detail the different components we used for the image decomposition.

5.1. Light profiles used in GALFIT

In our work, we use three different profiles to fit the source images. For most sources, this three-component model yields good fit residuals (fitting details provided in Sect. 5.2). Using more than three components typically results in overfitting of the images and over-subtracted residuals. The three components used for the fitting are:

Background sky. The background in the *Swift*/UVOT images is quite uniform for all the filters. Hence, we used a constant sky value to fit it. For the starting value, we used the background value as estimated by the Astropy (Astropy Collaboration 2022) package `photutils`[10] (used for photometry; Bradley et al. 2021), using the sigma-clipping method. By using a source detection threshold specified by the user, the median background value is calculated by removing the sources with source counts above the threshold and recalculating the background. Since this is just an input estimation for the background to be better fit by GALFIT, we used a value of two sigma above the median for source clipping. As input, GALFIT requires the user to provide an image region of the background without any sources to fit the sky. Whenever possible, we used offset background regions as close as possible to the source of interest to reduce small deviations across the area of the detector. For the majority of sources, a region of 100×100 pixels[11] was selected, which was otherwise modified according to the availability of larger regions without any sources in the image.

PSF profile for the AGN. To fit a PSF profile in GALFIT, one needs to provide as input a PSF image, which is then convolved with the model to create the PSF function used to fit the point source in the image. For our analysis, we created the PSF images for each source in each filter using the `EPSFBuilder` task in the `photutils` Astropy package, which uses bright stars in the source image to create an effective PSF. This method involves a series of steps, starting from finding the appropriate stars to create the PSF, extracting them, and finally iterating over the selected stars to build the PSF. Firstly, a few stars within a certain range of the count rate of the source of interest are selected. We used the `find_peaks` function to do this by specifying a threshold count rate slightly below that of the source, such that we have at least five to ten stars with count rates similar to that of the source to begin with. We then used the `extract_stars` function to extract 25×25 pixel cutouts of these stars that were visually inspected for distortions, fake detections, saturated pixels, and bad quality, and to ensure that they were sufficiently isolated. Finally, three to six stars were selected to create the PSF using the `epsf_builder` function with an oversampling factor of unity and ten iterations. The PSF image thus created was used as input in GALFIT along with the input source image and the bad-pixel mask. One needs to specify the region of the source image to be fit in the GALFIT template file. For most of the sources, we used a 100×100 pixel image region around the source, which is almost 25 times the size of the PSF and is sufficient to include the extended wings of the PSF. In the case of more extended sources, we used image regions large enough to include the source as well as some background. The PSF profile has only three free parameters in the GALFIT template file: the x and y coordinates and the total PSF magnitude. We specified the initial x and y coordinates based on the location of the center of the source and the input magnitude value as the one calculated for each source within the 5″ aperture using the `uvotsource` command of the *Swift*/UVOT data reduction pipeline.

Sérsic profile for the host galaxy. The host galaxy light in our sources, if and when needed, was fit using a Sérsic profile. The free parameters for this profile include the x and y

[9] https://users.obs.carnegiescience.edu/peng/work/galfit/galfit.html

[10] https://photutils.readthedocs.io/en/stable/index.html

[11] The plate scale of *Swift*/UVOT is 0.502 arcseconds.

coordinates of the source, the integrated magnitude, the Sérsic index[12], the effective radius, the axis ratio, and the position angle (PA). In most cases, we left all the parameters free to vary, unless the fit did not converge due to one specific parameter going out of bounds, in which case we fixed that parameter to an appropriate value (see Sect. 5.2). For most of the sources, a single Sérsic profile along with a PSF was sufficient to reproduce all the light coming from the galaxy. However, for some extended sources (8/290), we employed two Sérsic profiles, one for the bulge ($n \sim 4$) and one for the disk ($n \sim 1$), to fit the overall host galaxy light. On the contrary, for most of the distant sources ($z > 0.05$), the PSF was almost as large as the host galaxy, and hence we only used a PSF profile to fit the source.

5.2. GALFIT-ing procedure

For our sample of 290 unobscured AGN across the six *Swift*/UVOT filters, we decomposed images into galaxy and AGN light profiles using GALFIT, following the procedure stated below:

1. We first fit a 100 × 100 pixel region of the blank sky in the source image with a constant sky background.
2. Next, we selected a 100 × 100 pixel (or larger if needed) region around the source of interest to fit the central AGN and the background together using a sky + PSF profile. The input value for the sky was kept the same as the one obtained from the previous step. For the PSF profile, all the parameters were kept free during the fit.
3. Finally, we fit the same source region as the previous step with a sky + PSF + Sérsic profile. The best-fit values estimated in the second step were used as input values for the sky and PSF parameters in this step, while they were allowed to vary. This was mainly done because in almost all the cases the residuals in the second step showed over-fitting, especially in the central pixels. Hence, in this step we allowed the PSF and the Sérsic profiles to adjust to each other and simultaneously fit the source light profile. For the Sérsic profile, the starting values for the x and y coordinates and the integrated magnitude were kept the same as those of the PSF profile. The input value for the Sérsic index (n) was set at 2.5, the axis ratio (b/a) at 1.0, the effective radius (half-light radius; R_e) at 5.0 pix, and the PA at 0.0 deg. In most cases, if the fit does not converge, it was due to the Sérsic index or the effective radius reaching their limits[13]. In the case of the Sérsic index, we repeated the fits with different input values, going in the following order: $n = 2.0$, 1.5, 1.0, 0.5, 3.0, 3.5, and 4.0. In the case of the effective radius, we repeated the fits with various values depending on the source but noticed that the input value of R_e does not affect the PSF (AGN) magnitude. Since this work aims to construct and fit AGN SEDs to obtain reliable estimates of the quantities describing AGN physics, we focused on extracting good measurements of AGN magnitudes through the image decomposition process. Hence, during the fitting, the Sérsic profile was primarily used to apply constraints on the PSF profile, instead of exactly describing the host galaxy light profile. The input values used for parameters like R_e, b/a, and PA were always kept the same as they do not affect the final estimates of the PSF magnitude. In this respect, in cases when the fit with sky + PSF + Sérsic profile does not converge due to one of the Sérsic profile parameters going out of bounds, we still get reliable estimates for the PSF magnitude that we can use to construct the SEDs (see Fig. B.1). We have flagged such cases while reporting the best-fit values from the fitting.

We visually inspected the residuals of all fits. We show a few examples of the fitting with GALFIT and the obtained residuals in Figs. A.1 and A.2. As expected, considering the wide variety of light profiles in our source sample in terms of spatial extension and brightness, there were instances when the fit residuals were not good or some parameters like the Sérsic index or the effective radius were not constrained. There were cases when either the residuals still contained significant source emission that GALFIT was not able to model or the three component fit resulted in over-fitting of the source. For example, in the case of the farthest sources ($z > 0.1$) with very faint host galaxy profiles compared to the central AGN (predominately point source-like), the fit residuals with GALFIT were negative at the central pixels, showing over-subtraction from the fitting. In such cases (∼14%), we adopted the magnitudes estimated using the `uvotsource` command of the *Swift*/UVOT data reduction pipeline for an aperture of 5″ around the source, since within the defined region the flux was dominated by the central AGN. For the remaining sources, with a non-negligible contribution from the host galaxy, we wanted to be consistent in our image decomposition and quantify GALFIT's response to *Swift*/UVOT images. Hence, we carried out numerous simulations to check the reliability of PSF magnitudes estimated by GALFIT. As is described in detail in Appendix B, we simulated a fake population of type I AGN by placing a point-source (star) with varying relative magnitudes at the center of a type II AGN (similar to the procedure followed by Koss et al. 2011). We then fit these fake type Is with GALFIT and compared the PSF magnitudes computed by GALFIT with the initial magnitude of the star. We did this for a total of ten sources spanning the redshift range of our sample and also including different galaxy morphologies, and with ten different magnitudes for the central star to achieve ten different AGN light to host light ratios (5% to 95%). Based on these simulations, we concluded that for sources at redshifts >0.05 and with fluxes $<10^{-15}$ erg cm^{-2} s^{-1} Å^{-1}, the AGN magnitudes reported by GALFIT were brighter than the actual values (see Figs. B.2, B.3, and B.4). This was primarily attributed to the fact that GALFIT was not able to fit a Sérsic profile for these sources and as a result, the PSF magnitudes and fluxes estimated by GALFIT also included contributions from the host galaxy. From these simulations, we calculated the necessary corrections needed to obtain improved estimates of PSF magnitudes for these sources. In Sect. 5.3, we describe in detail how we estimated and employed these corrections in this work.

We also did some tests to check how the GALFIT-estimated AGN magnitudes for our *Swift*/UVOT images compare with those obtained by fitting the *Hubble* Space Telescope (HST) images for the same sources. In Appendix C we describe these tests in detail. Our main conclusion from these tests was that, even if the HST images show detailed and extended host galaxy profiles, if we just fit a small region around the nucleus with GALFIT, the estimated magnitudes are within 0.1 mag of those calculated using the lower resolution *Swift*/UVOT images. This is acceptable, considering the difference in the central wavelengths of the overlapping HST and UVOT filters.

[12] In a Sérsic light profile, the Sérsic index (n) defines the curvature of the light profile with distance from the center. Larger values of n indicate steeper inner light profiles and more extended outer wings, while low values of n indicate flatter corelight profiles and sharper truncation at large radii.

[13] GALFIT allows the Sérsic index to vary from 0.01 to 20 and the effective radius from 0.01 onward.

5.3. Corrections to GALFIT-estimated point spread function magnitudes

Based on the simulations (described in Appendix B) performed to understand how GALFIT decomposes the *Swift*/UVOT images and how reliable the estimated fluxes are, we reached some important conclusions. Firstly, for sources with very high counts (>1000 counts/pixel), GALFIT was unable to fit all the flux in the central pixels. This was primarily due to a poorly defined PSF. For these sources, the stars in the field of view that were used to create the PSF always had lower counts than the AGN itself. Therefore, the PSF was not suitable to fit such bright sources. However, the fit residuals in these cases were mostly <20% of the source image, and therefore, the estimated PSF magnitudes were consistent with the expected AGN magnitudes within their error range. Secondly, in the case of more distant sources ($z > 0.05$) with lower fluxes ($F < 10^{-15}$ erg cm^{-2} s^{-1} Å^{-1}), most of the time GALFIT was unable to converge while fitting a sky + PSF + Sérsic profile to the source image. As a result, the estimated PSF fluxes were higher than expected. Even in cases when GALFIT successfully fit a Sérsic profile to the source, the estimated PSF fluxes were higher than the expected values. We flagged such sources from our sample, to eventually be corrected before the final broadband SED fitting.

To calculate the appropriate corrections for different sources in the various optical and UV filters, we first plotted the difference in the PSF magnitude estimated by GALFIT and the actual magnitude of the point source used to replicate the AGN at the center of the simulated type I AGN population (ΔM) with respect to the AGN light ratio [$R_{\rm light}$ = AGN Light/(AGN Light + Host Galaxy Light)]. We use this particular representation ($R_{\rm light}$ vs. ΔM) because the simulations performed previously showed that the reliability of GALFIT's PSF flux prediction depends on the brightness of the AGN relative to the host galaxy (represented by $R_{\rm light}$). As is shown in Fig. 5, it is evident that the cases in which GALFIT was able to fit a Sérsic profile occupy a different parameter space compared to those where a Sérsic profile fit was not achieved. Therefore, we used two separate functions to fit these two trends for all six filters. Compared to a second-degree polynomial, a cubic polynomial provided a better fit, as it was able to better cover the sources at the higher end of $R_{\rm light}$. Based on these fits, we derived equations to calculate the value of ΔM for every filter corresponding to the two scenarios, whether a Sérsic fit was achieved or not. We would like to point out that a definite caveat of this analysis is the systematic uncertainties introduced in the final AGN magnitudes of the sources for which these corrections are applied. Therefore, one needs to be careful when using these corrections for individual source analysis. We emphasize that in order to minimize the effect of the systematic uncertainties in the corrected AGN fluxes (especially, in the optical bands), one should only use them for large sample studies, like this one.

In our final sample, for 46 sources (~20%) we used the corrections defined above to improve the PSF magnitudes estimated by GALFIT image decomposition. For 33 sources (~14%), we used the magnitudes estimated during the data reduction process instead of the GALFIT estimated PSF magnitudes due to over-subtracted residuals in at least one of the optical/UV filters. All these sources were visually confirmed to be point-like with negligible contribution from the host galaxy. The final AGN magnitudes, fluxes, and errors are listed in Tables A.6 and A.7. The sources for which GALFIT magnitudes were corrected and the sources for which we used the UVOT pipeline magnitudes are flagged accordingly in the tables. As is mentioned in Sect. 5.2, we do not report the values for the Sérsic profile (host galaxy) parameters, as the focus of this work is solely to constrain the AGN light to construct the corresponding AGN SEDs.

6. Broadband SED fitting

In this final part of the analysis, we use the optical and UV magnitudes calculated for each source to populate the optical/UV part of their SED. We start by using the PSF magnitudes estimated by GALFIT after the source image decomposition. As an initial step, we do not include the corrections computed on these magnitudes for the sources at $z > 0.05$, to understand how the results change before and after applying the corrections. The original source PHA[14] files for each source in each filter were edited to include the AGN magnitudes instead of the total source magnitudes estimated during the data reduction. The background PHA files were edited to have a value = 0.0 since the final magnitudes estimated by GALFIT are already corrected for the background in the first step of the decomposition (see Sect. 5). The response files from *Swift*/UVOT were edited to include the appropriate energy ranges (see Table 1) for respective filters.

The optical/UV part of the SED is fit in XSPEC (Arnaud 1996) using the `DISKPN` model, which is a thermal accretion disk model comprising multiple blackbody components (e.g., Mitsuda et al. 1984; Makishima et al. 1986). While it can successfully describe the optical/UV disk emission in many AGN sources (e.g., Malkan & Sargent 1982; Malkan 1983), the multi-temperature accretion disk model, which is otherwise assumed to be in a quasi-steady state equilibrium (e.g., Shakura & Sunyaev 1973; Thorne 1974), is inadequate to explain the observed variability timescales in the UV (e.g., Alloin et al. 1985; Collier & Peterson 2001; Lawrence 2012). We also acknowledge that by using a common disk model for all sources, we are making an assumption regarding the type of accretion flow in these sources. Numerous studies have shown that accretion in an AGN changes with its accretion rate, from possible ADAFs to standard thin disks to slim disks, as the accretion rate increases (see Beloborodov 1999 for a review). However, at this point, we cannot assume or define specifically how the surrounding material is accreted onto the central SMBH. Hence, we fit all the SEDs with the widely acceptable thermal disk model, so that we can later evaluate our results in a consistent way. We also ignore any contribution from emission lines in our disk model. Multiple studies on continuum reverberation mapping have shown that emission lines can have a small but non-negligible contribution to the disk continuum emission (e.g., Chelouche 2013; Miller et al. 2023). This contribution increases from <10% to ~30% as we move to photometric bands at higher wavelengths (r and i bands). However, in the context of this work, we can safely ignore this contribution (~10%) up till our highest wavelength V band. SED models that include emission lines (e.g., Temple et al. 2021) can be useful to study their effects on broadband SED fitting analysis, but it is beyond the scope of this work. In addition to the disk model, we include two components of the `ZDUST` model to take into account extinction due to dust grains (Pei 1992) in the optical and UV bands, associated with the Milky Way ($\texttt{ZDUST}_{\rm MW}$) and the host galaxy of the AGN ($\texttt{ZDUST}_{\rm HG}$), respectively. We use the convolution model `ZASHIFT` to shift the disk spectrum to the redshift of the respective source. Hence, the final model used to fit the optical/UV SED is:

$$\texttt{ZDUST}_{\rm MW} \times \texttt{ZDUST}_{\rm HG} \times \texttt{ZASHIFT} \times \texttt{DISKPN}.$$

[14] XSPEC-compatible fits format

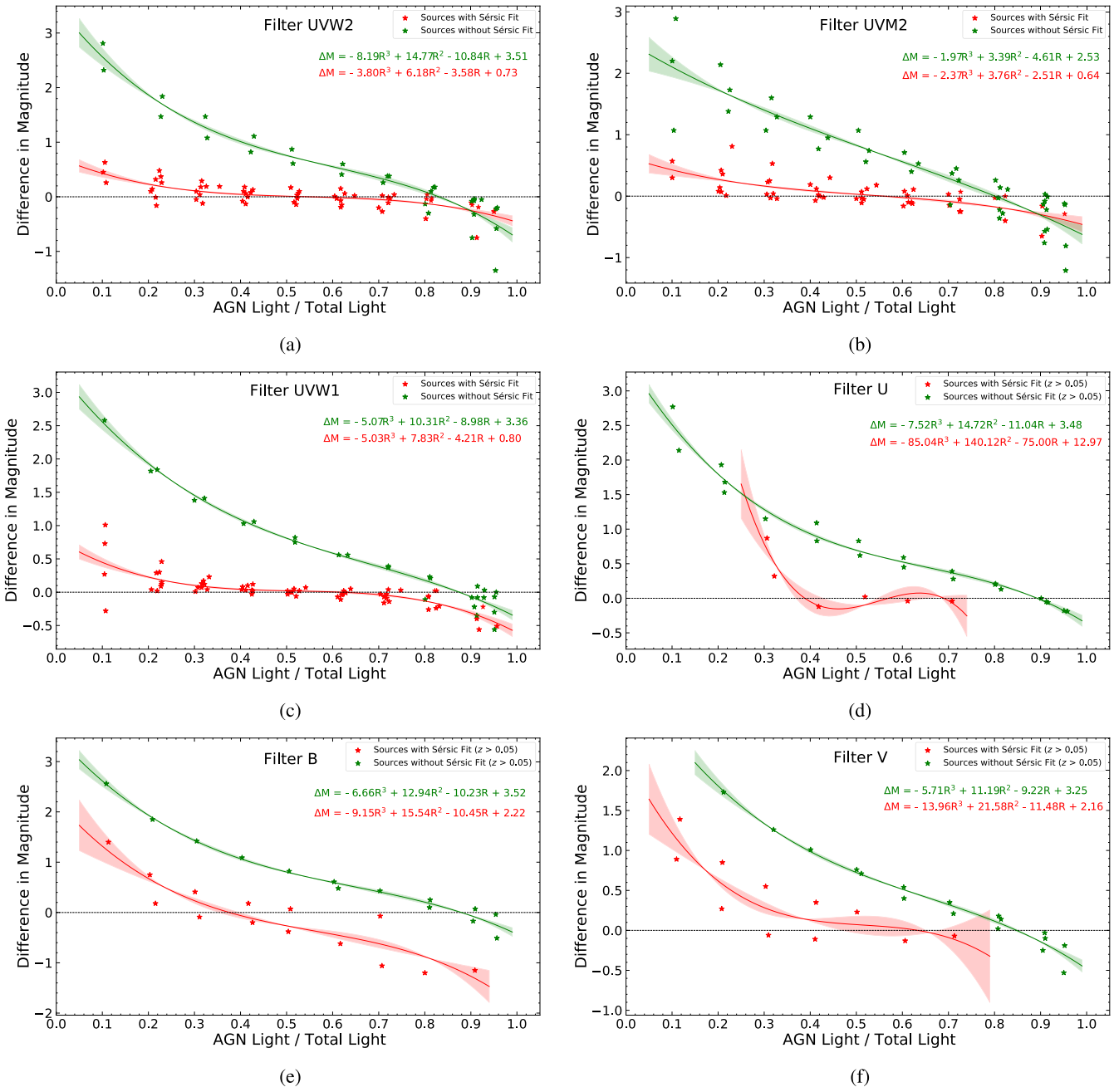

Fig. 5. Difference between the PSF magnitudes estimated by GALFIT and the actual magnitude of the point source used to replicate the AGN at the center of the simulated type I AGN population (ΔM) vs. the AGN light ratio ($R_{\rm light}$) for all six *Swift*/UVOT filters, (a) UVW2, (b) UVM2, (c) UVW1, (d) U, (e) B, and (f) V, based on simulations (described in Appendix B). The plots also show the best-fit function and their equations for both cases: when a Sérsic profile fit was obtained (in red) and when a fit with a Sérsic profile fit was not possible (in green). The equations mentioned in each figure were then used to calculate the corresponding corrections to improve the PSF magnitudes estimated by GALFIT during the source image decomposition to obtain the AGN light devoid of host galaxy contamination (see Sect. 5.3).

For the two reddening components, we adopt a Milky Way (MW) extinction curve (method = 1) and $R_{\rm v} = 3.08$. In the case of dust extinction due to our galaxy, we fix the $E(B-V)$ value to those estimated by Schlegel et al. (1998), who combined the results of IRAS and COBE/DIRBE to create a 100-micron intensity map of the sky. The $E(B-V)$ for the AGN host galaxy is allowed to vary during the fitting. The redshifts for the two components are fixed to 0.0 and the redshift of the source, respectively.

For the DISKPN, the free parameters include the normalization ($K_{\rm uvo}$) and the maximum temperature of the disk ($kT_{\rm max}$; in units of keV). Here, the normalization is defined as

$$K_{\rm uvo} = M^2 \cos(i)/(D^2 \times \beta^4), \quad (1)$$

where M is the mass of the central body (the SMBH in our case) in solar masses, i is the inclination angle of the disk, D is the distance to the source in kpc, and β is the color to effective temperature ratio. The inner radius of the disk ($R_{\rm in}$; in units of $R_{\rm g} = GM/c^2$) is fixed to 6.0 gravitational radii[15]. In

[15] https://heasarc.gsfc.nasa.gov/xanadu/xspec/manual/node169.html

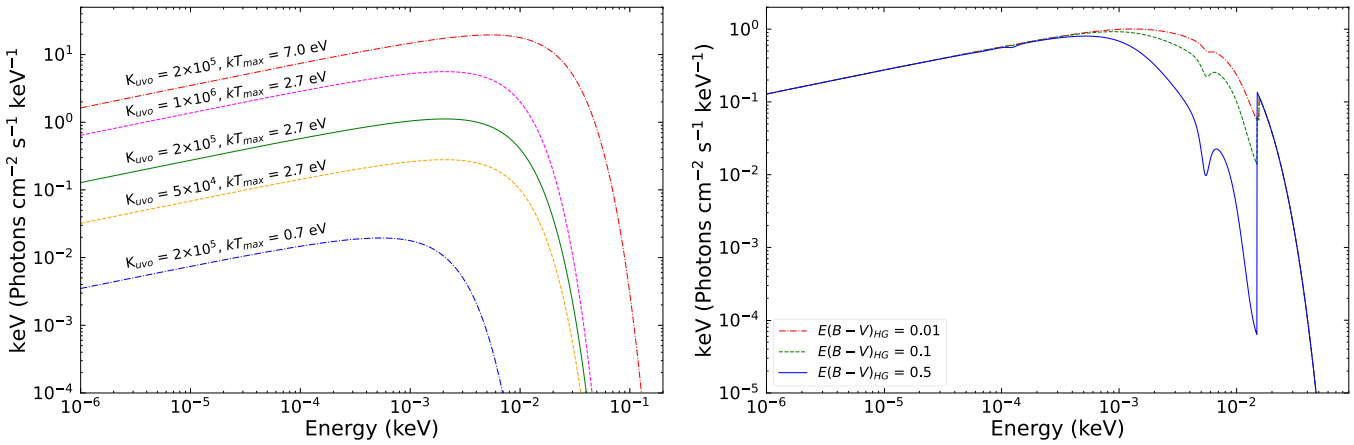

(a) (b)

Fig. 6. Optical/UV SED model adopted for this study (a) without absorption, for different values of $kT_{\rm max}$ (dash-dotted lines), keeping $K_{\rm uvo}$ constant at 2×10^5, and for different values of $K_{\rm uvo}$ (dashed lines), keeping $kT_{\rm max}$ constant at 2.7 eV and (b) with absorption, for different values of $E(B-V)_{\rm HG}$, with $kT_{\rm max}$ = 2.7 eV, $K_{\rm uvo} = 2\times10^5$, and $E(B-V)_{\rm MW} = 0.05$. The former plot shows possible degeneracy between parameters $kT_{\rm max}$ and $K_{\rm uvo}$, while the latter shows effects of host galaxy dust extinction on the optical/UV SED model, almost negligible for $E(B-V)_{\rm HG} \leq 0.01$.

Fig. 6, we show different realizations of our adopted model for the optical/UV SED based on various parameter values. In the left panel (6a), we have plotted the multi-temperature accretion disk model (without absorption) for: (i) three values of $kT_{\rm max}$ (0.7 eV, 2.7 eV, and 7.0 eV), keeping $K_{\rm uvo}$ constant at 2×10^5, assuming $M = 10^{7.9}\,M_\odot$ (median black hole mass), $i = 0°$ (for face-on disks), $D = 176$ Mpc (median distance), and $\beta = 1$ (Vasudevan & Fabian 2009) and (ii) for three values of $K_{\rm uvo}$ (5×10^4, 2×10^5, and 1×10^6), keeping $kT_{\rm max}$ constant at 2.7 eV (median value). In the right panel (6b), we show the effect of dust extinction due to the host galaxy on our SED models for a source at the median redshift of our sample ($z = 0.04$), with $kT_{\rm max} = 2.7$ eV (median value), $K_{\rm uvo} = 2\times10^5$, and $E(B-V)_{\rm MW} = 0.05$ (median value). We note that as we increase the maximum temperature of the disk, the optical/UV emission not only extends to higher energies but the amount of flux emitted also increases. The latter is also visible as an outcome of increasing the disk normalization. Hence, there is a clear degeneracy between the parameters, $kT_{\rm max}$ and $K_{\rm uvo}$. To achieve a good fit of the optical/UV photometric points of a high (low) flux source, the model could either increase (decrease) $kT_{\rm max}$ without changing $K_{\rm uvo}$ or vice versa. To ensure that this degeneracy does not affect our SED fitting results, we make sure that the best-fit values of $kT_{\rm max}$ are reasonable and do not exceed the upper limit of a few tens of eVs ($\sim10^{5.8}$ Kelvin), expected from typical Shakura & Sunyaev (1973) accretion disks around nonrotating Schwarzchild or rotating Kerr black holes (e.g., Bonning et al. 2007, 2013).

After compiling and preparing all the source PHA files, and defining the model to be used, we begin by fitting 223/290 (~77%) sources that have observations in all the six *Swift*/UVOT filters. The best fit is obtained based on the reduced chi-square and visually inspecting the fit residuals. In cases when the host galaxy $E(B-V)$ was of the order 10^{-4} or less, or when it was not constrained, we repeated the fit by fixing it to zero, as effects of host galaxy dust extinction are almost negligible below $E(B-V)_{\rm HG} \sim 0.01$ (see Fig. 6b). The best-fit values of all free parameters were checked using the `steppar` command. The errors in all the free parameters ($E[B-V]_{\rm HG}$, $kT_{\rm max}$, and $K_{\rm uvo}$) were calculated using the `error` command. Next, we fit the sources with observations in at least four of the *Swift*/UVOT filters (13/290 ~4.5% sources) following the same procedure as before. For the remaining 54/290 (~18.5%) sources, we had observations in fewer than four filters. Considering the three free parameters in the model used for fitting, it was not possible to fit these sources (with three or fewer data points), and to get reliable estimates of all the fit parameters. Therefore, we did not fit the optical/UV SEDs for these sources due to missing observations in more than two *Swift*/UVOT filters. We show a few examples of our SED fits, along with the best-fit model and residuals, in Figs. 7 and 8.

Out of the 236 sources for which we perform the optical/UV SED fits, the parameter corresponding to the maximum temperature of the accretion disk ($kT_{\rm max}$) was not constrained for 27 (~11%) sources. As was mentioned previously, these were high flux sources for which the model initially favored extremely high $kT_{\rm max}$ values (≥20 eV; otherwise impossible for AGN disks) to obtain a suitable fit. In these objects, we fixed $kT_{\rm max}$ to its median value (2.7 eV) obtained from the sources that were successfully fit while constraining the disk temperature. The final best fits were used to calculate the observed and intrinsic (rest-frame and absorption-corrected) model fluxes and luminosities in all the six *Swift*/UVOT filters. The total intrinsic optical + UV luminosity ($L_{\rm uvo}$) was estimated in the energy range from 10^{-7} to 0.1 keV, since the standard Shakura & Sunyaev (1973) disk typically has very little to no emission in the X-rays. The luminosity thus computed will later be combined with $L_{\rm x}$ (see Sect. 4) to estimate the total accretion luminosities ($L_{\rm bol}$) of the AGN in our sample. The upper and lower limits of these fluxes were calculated considering the 90% confidence intervals of $K_{\rm uvo}$ and $E(B-V)_{\rm HG}$. The lower limit in the flux of each source corresponds to the best-fit model of that source with the highest $E(B-V)_{\rm HG}$ (most dust extinction) and lowest $K_{\rm uvo}$ as estimated during the fitting, and vice versa (see Table A.8).

We repeat the optical/UV SED fitting, as stated above, for the more distant ($z > 0.05$) sources after applying the corrections to their GALFIT-estimated PSF magnitudes (described in Sect. 5.3). For a total of 46 (~20%) sources, we redo the SED fitting after editing their source PHA files to include the corrected GALFIT PSF magnitudes. We report the best-fit values of $kT_{\rm max}$ and $E(B-V)_{\rm HG}$ along with the various flags regarding the SED fitting in Table A.8. In the next section we discuss in detail

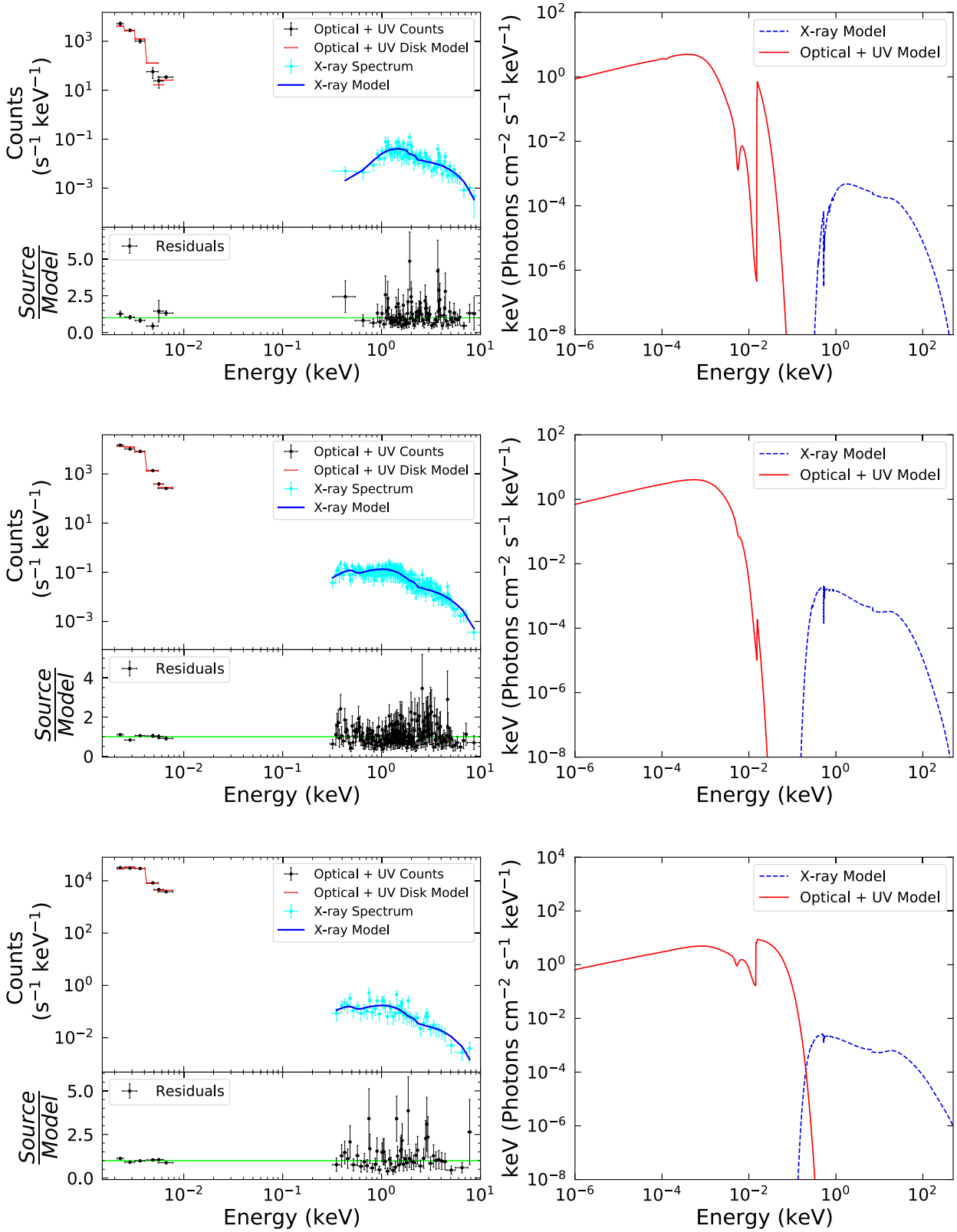

Fig. 7. Examples of the optical-to-X-ray SED fits. From top to bottom, the fits are for SWIFTJ0208.2+4452, SWIFTJ0630.7+6342, and SWIFTJ1421.4+4747. The left panel shows the counts in the optical/UV filters (black points) and the 0.3–10 keV X-ray spectrum (cyan points). The figure also shows the fit obtained using the optical/UV disk model including dust extinction (in red) and the X-ray model (in blue), along with the fit residuals (bottom left panel). The right panel shows the best-fit SED model for each source.

the results we found for all three samples: (a) the total sample of 236 sources without applying corrections to the magnitudes necessary for distant sources, (b) a sub-sample of 190 sources, removing the sources that need to be corrected, and (c) the total sample of 236 sources including corrections to the magnitudes estimated by GALFIT for the distant sources.

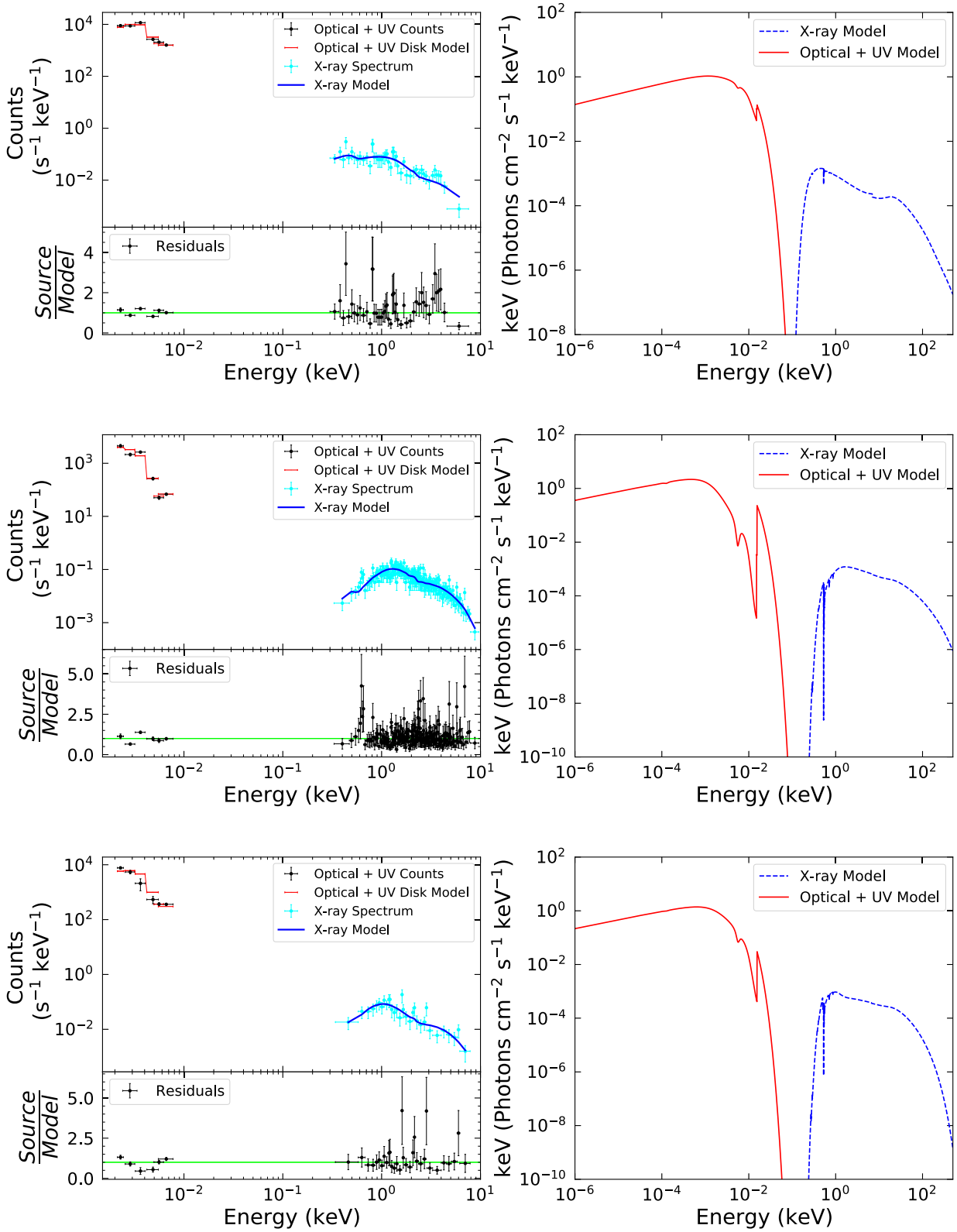

Fig. 8. Examples of the optical-to-X-ray SED fits. From top to bottom, the fits are for SWIFTJ0002.5+0323, SWIFTJ0654.6+0700, and SWIFTJ1316.9-7155. The left panel shows the counts in the optical/UV filters (black points) and the 0.3–10 keV X-ray spectrum (cyan points). The figure also shows the fit obtained using the optical/UV disk model including dust extinction (in red) and the X-ray model (in blue), along with the fit residuals (bottom left panel). The right panel shows the best-fit SED model for each source.

7. Results and discussion

In the previous sections we explained in detail the various steps we followed to systematically construct and fit the optical-to-X-ray SEDs of a sample of ∼240 unobscured AGN. In this section we focus on the outputs of our SED fitting and explore some of the important scaling relations between them.

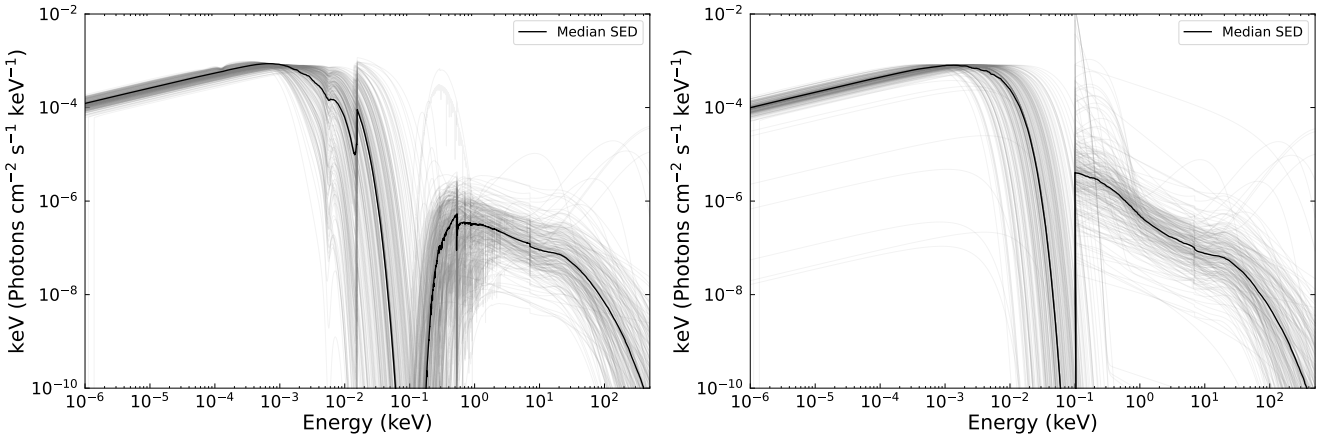

Fig. 9. Rest frame optical-to-X-ray best-fit SED models (a) with absorption and (b) without absorption, for the 236 unobscured, nearby AGN in our sample (in gray). The SEDs have been normalized by total flux. The median SED model is shown as a solid black line.

All the results reported in the following sections are for the final sample of 236 unobscured AGN with GALFIT fluxes corrected as is explained in Sect. 5.3 for the sources at $z > 0.05$. However, we checked all our results for the sample without employing these corrections and did not find any qualitative differences. We also confirmed all our results to hold for a cleaner sample of 190 AGN excluding the distant sources that need to be corrected. In Sect. 7.1 we present the SED models for our sample of unobscured AGN. In Sect. 7.2 we study the parameters that describe the optical/UV disk emission, such as the temperature of the accretion disk (Sect. 7.2.1) and the extinction due to host galaxy (Sect. 7.2.2). And finally, in Sects. 7.3 and 7.4 we present the optical-to-X-ray spectral index (α_{ox}) and various bolometric corrections (κ_λ), respectively, and explore their dependence on different physical properties of AGN, such as black hole mass, bolometric luminosity, and Eddington ratio.

7.1. Diversity in SED models

In Fig. 9a, we show all the optical-to-X-ray SED models for our sample, as well as the rest-frame median SED model (in solid black). In the adjacent panel (Fig. 9b), we show the intrinsic, absorption-corrected SED models for our sample along with the median, absorption-corrected SED (in solid black). All the SEDs have been normalized by the total flux. Comparing the two panels, we can clearly see the absorption features due to the host galaxy and the Milky Way in the optical/UV and soft X-rays. A reflection feature around 7 keV is visible in both cases. As has been mentioned in many previous works on broadband SED fitting (e.g., Elvis et al. 1994; Richards et al. 2006; Vasudevan et al. 2009), and also visible in Fig. 9, there exists a large variety in the shapes of AGN SEDs that one needs to take into account to explore the full range of properties exhibited by the AGN population. A more detailed analysis of SED shapes of unobscured AGN based on their physical properties, such as black hole mass, luminosity, and Eddington ratio will be presented in another upcoming publication (Gupta et al., in prep.). Additionally, a complete study of the X-ray-to-far-IR SEDs of all *Swift*/BAT AGN is ongoing (Rojas et al., in prep.).

7.2. Optical/UV disk emission

The optical/UV part of the multiwavelength AGN SED corresponds to the emission that is believed to originate from the accretion disk, at different radii, as material spirals into the central SMBH (e.g., Shields 1978; Malkan & Sargent 1982; Ward et al. 1987). This emission is expected to be the largest contributor to the total accretion luminosity of the AGN. In the following two sections, we look in detail at the parameters constrained from the optical/UV SED fitting; that is, the maximum disk temperature (Sect. 7.2.1), and the dust extinction due to the host galaxy (Sect. 7.2.2).

7.2.1. Disk temperature

The standard accretion disk model suggested by Shakura & Sunyaev (1973) considers a geometrically thin and optically thick structure for the disk with a temperature gradient, such that higher temperatures are expected at closer proximity to the SMBH, until the innermost stable circular orbit. Based on our SED fitting analysis using a multi-temperature accretion disk model, we obtained the maximum disk temperatures for our sample of unobscured AGN with a median $kT_{max} = 2.70 \pm 0.01$ eV (see Fig. 10a). The range of kT_{max} values from this work are in agreement with those calculated using non-LTE (local thermodynamic equilibrium) AGN disk models (Hubeny et al. 2000) for a wide range of black hole masses and Eddington ratios (see Bonning et al. 2007, 2013). When plotted against the redshift of the source, we see an increase in the value of kT_{max} with z (as is shown in Fig. 10b). This positive correlation between kT_{max} and z (see Table 2) does not necessarily imply that higher redshift sources have higher disk temperatures. In fact, it is an effect of the flux-limited nature of the *Swift*/BAT AGN sample. Since more distant sources have to be brighter to be detected, this results in a sample where farther away sources are more luminous and have higher disk temperatures.

We also explore possible correlations of kT_{max} of the accretion disk with other properties of the AGN, such as bolometric luminosity, black hole mass, and Eddington ratio. From the broadband SED fitting, we use the X-ray flux from 0.1 to 500 keV (L_x) and the optical/UV flux from 10^{-7} to 0.1 keV (L_{uvo}) to estimate the total accretion luminosity or the bolometric luminosity ($L_{bol} = L_x + L_{uvo}$) for our unobscured AGN sample (see Table A.9). All luminosities are calculated using the distances listed in Table A.1. The Eddington ratios for all our AGN (reported in Table A.9) are calculated using $\lambda_{Edd} = L_{bol}/L_{Edd}$.

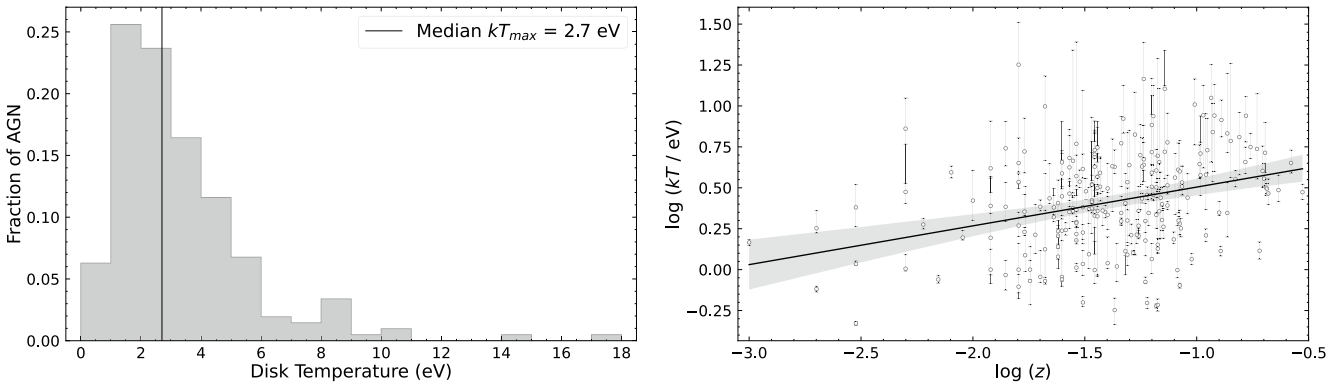

(a) (b)

Fig. 10. Maximum disk temperature ($kT_{\rm max}$) as obtained after fitting the optical/UV SEDs of our source sample with a dust-extinction-corrected thermal disk model (described in Sect. 6). (a) Distribution of the best-fit values of $kT_{\rm max}$. The median value of $kT_{\rm max}$ from this distribution is 2.7 eV. (b) $kT_{\rm max}$ as a function of the redshift of the source. The solid black line shows the best-fit relation (Sect. 7.2.1, Table 2) and the shaded gray region displays the uncertainty on the regression.

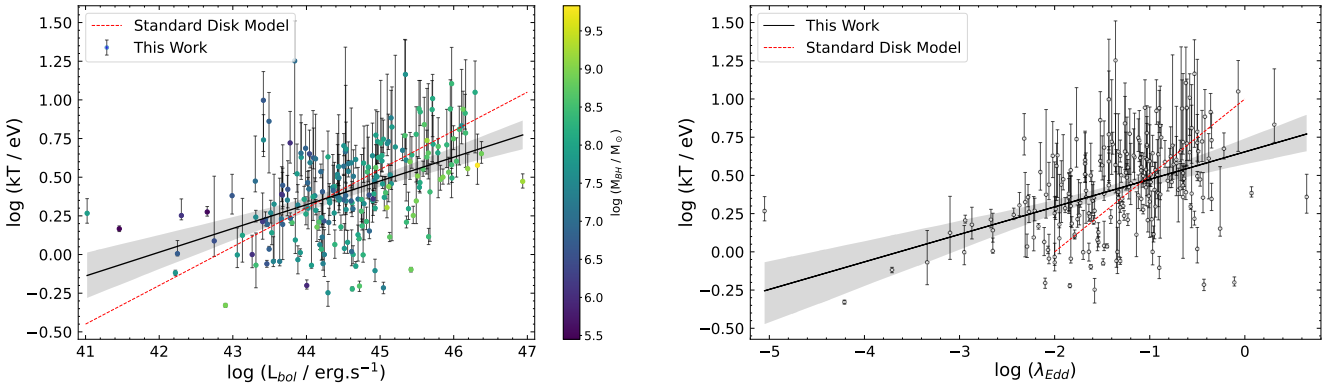

(a) (b)

Fig. 11. Maximum disk temperature ($kT_{\rm max}$) as a function of (a) the bolometric luminosity (color-coded with black hole mass), and (b) the Eddington ratio. The solid black line shows the best-fit relation (Sect. 7.2.1, Table 2) and the shaded gray region is the one sigma confidence interval. The dashed red line is the theoretical relation between (a) $kT_{\rm max}$ and $L_{\rm bol}$ ($T_{\rm max} \propto L_{\rm bol}^{1/4}$) and (b) $kT_{\rm max}$ and $\lambda_{\rm Edd}$ ($T_{\rm max} \propto \lambda_{\rm Edd}^{1/4}$), as is expected from the standard Shakura & Sunyaev (1973) disk model for a fixed black hole mass.

To be consistent with the BASS DR2 (see Koss et al. 2022b), we define the Eddington luminosity as

$$L_{\rm Edd} = 1.5 \times 10^{38} \times \frac{M_{\rm BH}}{M_\odot}\ {\rm erg\ s^{-1}}. \quad (2)$$

As part of the BASS DR2, Mejía-Restrepo et al. (2022) calculated the black hole masses using the virial method and reverberation mapping for almost all *Swift*/BAT type I AGN in the 70-month catalog. We have these black hole mass estimates for 235/236 sources in our sample and we use them throughout this work.

We find a strong positive correlation of the disk temperature with both $L_{\rm bol}$ and $\lambda_{\rm Edd}$ (Fig. 11, Table 2). This is not surprising as under the assumption of the standard disk model (Shakura & Sunyaev 1973) employed here to fit the optical/UV SED, we would expect sources with larger luminosities and Eddington ratios (up to the Eddington limit) to have hotter disks. This is a reasonable assumption for our sample since it does not probe high Eddington ratios ($\lambda_{\rm Edd} > 1$), and only has a few sources (<15%) extending to the low Eddington ratio regime of $\lambda_{\rm Edd} < 0.01$ where the standard disk model might fail (e.g., Koratkar & Blaes 1999; Narayan 2005; Yuan & Narayan 2014). Theoretically, the maximum value of the effective temperature of the Shakura & Sunyaev (1973) disk relates with the luminosity and the black hole mass as $T_{\rm max} \propto L_{\rm bol}^{1/4} M_{\rm BH}^{-1/2}$ (see review by Novikov & Thorne 1973). This relation can be further modified as $T_{\rm max}^4 \propto \lambda_{\rm Edd} M_{\rm BH}^{-1}$. However, we do not find any such dependence of $kT_{\rm max}$ on $M_{\rm BH}$. This is shown in Fig. 11a, where the points are color-coded with the black hole mass, but the only visible trend of $M_{\rm BH}$ is with $L_{\rm bol}$ (intrinsic to our sample). We show the theoretical relations (considering a fixed black hole mass) in Fig. 11 as a dashed red line, along with our best-fit regression lines (in black). The slopes of our relations (0.15 ± 0.02 and 0.18 ± 0.03) are slightly flatter compared to the theoretical expectation (0.25), which could be due to the lack of any information on the accretion efficiency of our sources. Furthermore, this also adds on to the already established concerns on the applicability of the Shakura & Sunyaev (1973) disk model to a large AGN population such as ours, spanning wide ranges in luminosity, black hole mass, and Eddington ratio.

7.2.2. Host galaxy dust extinction

One of the components (ZDUST) of our optical/UV SED model takes into account the intrinsic dust extinction of the source

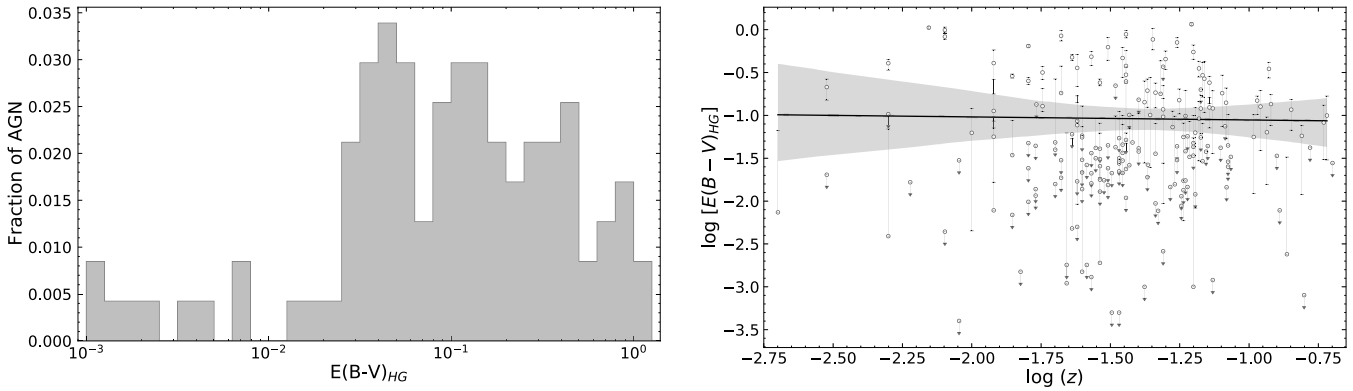

(a) (b)

Fig. 12. The intrinsic dust extinction of the AGN emission in the optical/UV due to the host galaxy, quantified by the parameter $E(B-V)_{\rm HG}$, calculated from the optical/UV SED fitting (described in Sect. 6). (a) Distribution of the best-fit values of $E(B-V)_{\rm HG}$ and (b) $E(B-V)_{\rm HG}$ as a function of the redshift (upper limits shown as downward arrows). The solid black line shows the best-fit relation excluding the upper limits and the shaded gray region marks the one sigma confidence interval. We find a similar relation if we include the upper limits using survival analysis and hence, do not show it here.

emission due to its host galaxy. This is quantified by the parameter $E(B-V)_{\rm HG}$. For 188 sources (∼80%), our SED fitting was able to constrain the value of $E(B-V)_{\rm HG}$ (with 90 upper limits), while for the rest it was either obtained or fixed to be zero (see Sect. 6 for details). We use survival analysis (e.g., Feigelson & Nelson 1985; Shimizu et al. 2017) to include the effects of upper limits while calculating the correlations in this section. In Fig. 12, we show the distribution of $E(B-V)_{\rm HG}$ and also how it changes with redshift. We do not find any dependence of the intrinsic dust extinction experienced by the disk emission on the redshift. The Fig. 12b only shows the linear relation (in black) obtained after excluding the upper limits, as their inclusion also gives a similar result. We also checked if $E(B-V)_{\rm HG}$ correlates with any other physical properties of the AGN, such as $L_{\rm bol}$, $M_{\rm BH}$, and $\lambda_{\rm Edd}$ but did not find any significant trends.

While in the optical/UV, $E(B-V)_{\rm HG}$ quantifies the extent of extinction undergone by the overall AGN disk emission, in the X-rays the line-of-sight column density ($N_{\rm H}$) describes the level of obscuration experienced by the more compact corona emission produced near the innermost portions of the accretion disk. To determine if there exists any link between the two wavelength-dependent forms of obscuration, we plot them against each other in Fig. 13 and obtain a weak positive correlation between them (see Table 2). We show both linear fits, with or without upper limits included, in the figure. It is worth mentioning here that even if both parameters quantify the level of obscuration of the emission at respective energies, considering that this emission originates in different regions of the AGN (at different physical scales), the material responsible for the extinction or obscuration could be different. Additionally, the lack of a strong correlation could also be rooted in the different spatial extents of the obscurers responsible in each waveband. The X-ray corona can be affected by individual BLR clouds (e.g., Risaliti et al. 2002; Bianchi et al. 2012), dust clumps in the torus (e.g., Markowitz et al. 2014; Ramos Almeida & Ricci 2017), in addition to the gas and dust surrounding the AGN, whereas the reddening of the disk requires more large-scale and extended structures.

7.3. Optical-to-X-ray spectral index ($\alpha_{\rm ox}$)

The relation between the optical/UV and X-ray emission of AGN has long been an area of extensive investigation to better understand the energy generation mechanism in AGN (e.g., Tananbaum et al. 1979; Avni & Tananbaum 1982, 1986; Wilkes et al. 1994; Yuan et al. 1998). In this context, the optical-to-X-ray spectral index or $\alpha_{\rm ox}$ is widely used to explore how the optical/UV disk emission couples with the X-ray coronal emission of AGN (e.g., Lusso & Risaliti 2016). This parameter can be used to quantify the shape of the AGN SED and as a proxy for bolometric corrections, since it is relatively easy to calculate from limited data. $\alpha_{\rm ox}$ is defined as:

$$-0.3838 \times \log\left[L_\nu(2500\,\text{Å})/L_\nu(2\,\text{keV})\right] \quad (3)$$

where L_ν is the luminosity at the specific wavelength or energy in units of erg s^{-1} Hz^{-1} (e.g., Strateva et al. 2005; Steffen et al. 2006). Over the years, many studies have been carried out focusing on how $\alpha_{\rm ox}$ evolves with redshift, and the AGN luminosity. Although no strong dependence has been reported with redshift (however, also refer to Bechtold et al. 2003 and Rankine et al. 2024), studies have shown that $\alpha_{\rm ox}$ has a significant anticorrelation with UV luminosity (e.g., Strateva et al. 2005; Steffen et al. 2006; Vasudevan & Fabian 2009; Lusso et al. 2010; Grupe et al. 2010; Temple et al. 2023). Some studies have also investigated if the way we define $\alpha_{\rm ox}$ (using the 2500 Å and 2 keV luminosities) is the most suitable, considering the purely historical choice of the two points (e.g., Young et al. 2010; Signorini et al. 2023; Jin et al. 2024). We explore this issue briefly at the end of this section.

To calculate $\alpha_{\rm ox}$ using Eq. (3), we estimate the monochromatic fluxes and luminosities at 2500 Å and 2 keV using the best-fit models obtained from the broadband SED fitting. We first have a look at the well-established correlation between the two luminosities ($L_{2500\,\text{Å}}$ and $L_{2\,\text{keV}}$). Most studies have narrowed down the correlation between the UV and X-ray luminosity to $L_{2\,\text{keV}} \propto L^{\beta}_{2500\,\text{Å}}$, where β ranges between 0.7 to 0.9 (e.g., Avni & Tananbaum 1986; Wilkes et al. 1994; Strateva et al. 2005; Steffen et al. 2006; Just et al. 2007; Lusso et al. 2010; Stalin et al. 2010; Marchese et al. 2012). Slightly larger values for β (>0.9) have been reported by some works (e.g., Green et al. 2009; Jin et al. 2012). This nonlinear correlation between the X-ray and the UV luminosity implies that optically bright AGN emit fewer X-rays (per UV luminosity) compared to optically faint sources (e.g., Avni & Tananbaum 1982). This

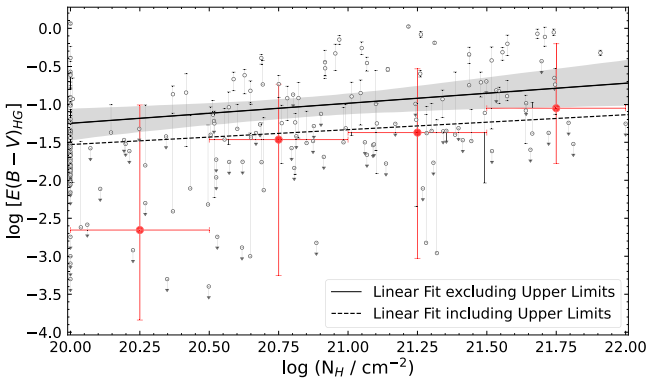

Fig. 13. Host galaxy dust extinction in the optical/UV $[E(B-V)_{\rm HG}]$ as a function of the X-ray column density ($N_{\rm H}$). Upper limits in $E(B-V)_{\rm HG}$ are shown as downward arrows. The solid black line shows the weak correlation between the two quantities if we exclude the upper limits (Sect. 7.2.2, Table 2) and the shaded gray region represents the uncertainty on the regression relation. The red points are the median $E(B-V)_{\rm HG}$ values (including upper limits) in bins of $N_{\rm H}$ and the dashed black line is the linear fit using survival analysis to include the contribution from all upper limits.

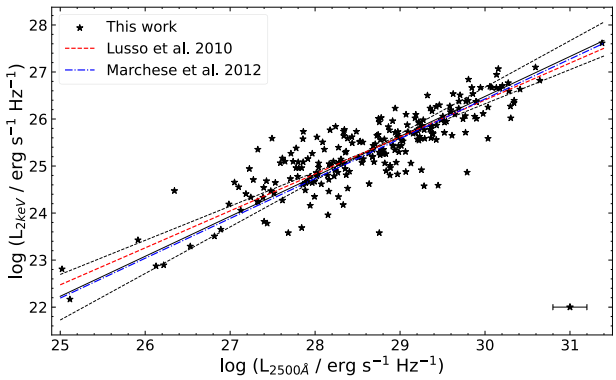

Fig. 14. Monochromatic luminosity at 2500 Åvs. the monochromatic luminosity at 2 keV. The two best-fit relations (Eqs. (4) and (5)) and the final bisector regression from our work (Eq. (6)) are shown as dashed and solid black lines, respectively. We also show the relation reported by Lusso et al. (2010; for their photometrically selected sample) and Marchese et al. (2012) as a dashed red line and a dash-dotted blue line, respectively. The typical uncertainties on $L_{2\,\rm keV}$ are less than 5% and those on $L_{2500\,\text{Å}}$ are shown in the bottom right corner (also valid for subsequent plots including $L_{2\,\rm keV}$ and $L_{2500\,\text{Å}}$).

Table 2. Correlation results for Figs. 10b, 11, 12b, and 13, described in Sect. 7.2.

Correlation	R-Value [a]	P-Value [b]	Scatter
$kT_{\rm max} - z$	0.32	1.76×10^{-6}	0.29
$kT_{\rm max} - L_{\rm bol}$	0.47	4.32×10^{-13}	0.27
$kT_{\rm max} - \lambda_{\rm Edd}$	0.45	9.95×10^{-12}	0.27
$E(B-V)_{\rm HG} - z$	−0.02	0.85	–
$E(B-V)_{\rm HG} - N_{\rm H}$	0.25	0.02	–

Notes. We also report the one sigma dispersion (or scatter in dex) for parameters with significant correlations. [a]The Pearson's correlation coefficient. [b]The probability of the data set appearing if the null hypothesis is correct.

relation between the UV and X-ray luminosity is extremely useful to investigate possible links between the accretion disk and the hot corona, respectively. Additionally, the strong X-ray-UV luminosity relation is also fundamental for recent cosmological studies that intend to use quasars as standard candles and extend the Hubble diagram to higher redshifts (e.g., Risaliti & Lusso 2015; Lusso & Risaliti 2017; Lusso et al. 2020; Signorini et al. 2023).

We estimate the best fit regression relation between $L_{2500\,\text{Å}}$ and $L_{2\,\rm keV}$ using the Python package `linmix`, and by including the errors on the dependent variable. We first treat $L_{2500\,\text{Å}}$ as the independent variable and get:

$$\log(L_{2\,\rm keV}) = (0.726 \pm 0.029) \times \log(L_{2500\,\text{Å}}) + (4.544 \pm 0.821) \quad (4)$$

We then estimate the same relation by considering $L_{2\,\rm keV}$ as the independent variable and find

$$\log(L_{2\,\rm keV}) = (0.990 \pm 0.039) \times \log(L_{2500\,\text{Å}}) + (3.025 \pm 1.006) \quad (5)$$

The final relation is the bisector of the above two regressions (as was described by Isobe et al. 1990):

$$\log(L_{2\,\rm keV}) = (0.850 \pm 0.013) \times \log(L_{2500\,\text{Å}}) + 0.985 \quad (6)$$

In Fig. 14, we plot the rest-frame monochromatic luminosity at 2 keV as a function of the rest-frame monochromatic luminosity at 2500 Å along with the three best-fit relations mentioned above. When comparing our results with the literature, it is difficult to find an agreement with all previous works considering the wide range of values that have been reported for the slope of this correlation. We find that our results are the most consistent with Stalin et al. (2010; $\beta = 0.870 \pm 0.001$) and Marchese et al. (2012; $\beta = 0.847 \pm 0.036$) for their sample of X-ray-selected type I AGN. However, in comparison with other works that found $\beta < 0.8$ (e.g., Steffen et al. 2006; $\beta = 0.721 \pm 0.011$; Just et al. 2007; $\beta = 0.709 \pm 0.010$; Lusso et al. 2010; $\beta = 0.760 \pm 0.022$), we find a steeper correlation between the X-ray and UV luminosity. This discrepancy in the computed slope could be attributed to several factors including selection effects, fitting techniques, variability, sample size, redshift range, etc. For example, our sample consists of hard-X-ray-selected AGN, further classified as unobscured based on their X-ray column density, whereas, most of the studies that obtained a shallower slope focused on optically selected AGN (e.g., Steffen et al. 2006; Just et al. 2007). It has been discussed by Yuan et al. (1998) and Tang et al. (2007) that intrinsic dispersions in the optical and X-ray luminosity can affect the overall correlation in optically selected, flux-limited samples. The slope quoted by Green et al. (2009; $\beta = 1.117 \pm 0.017$) is for their sample of optically selected quasars that have a low X-ray detection factor. However, for their sub-sample with a 100% detection rate in the X-rays (zLxBox), they obtain a slope ($\beta = 0.842 \pm 0.017$) consistent with ours. When the X-ray-selected sample studied by Lusso et al. (2010) is further separated into spectroscopically and photometrically classified sources, they obtain a larger value for β (0.782 ± 0.033 and 0.786 ± 0.033), closer to our estimates.

Next, we plot the distribution in $\alpha_{\rm ox}$ for our AGN sample in Fig. 15a. We obtain $\alpha_{\rm ox}$ values ranging from −2.0 to −0.7, with a median at −1.28 (also see Table A.9). We do not see any significant trend in $\alpha_{\rm ox}$ with redshift (Fig. 15b, Table 3) as confirmed by most previous works (but see Yuan et al. 1998 and Bechtold et al. 2003). Following the strong, nonlinear relation established between the X-ray and UV luminosity, we expect the ratio of these luminosities to correlate with the UV luminosity.

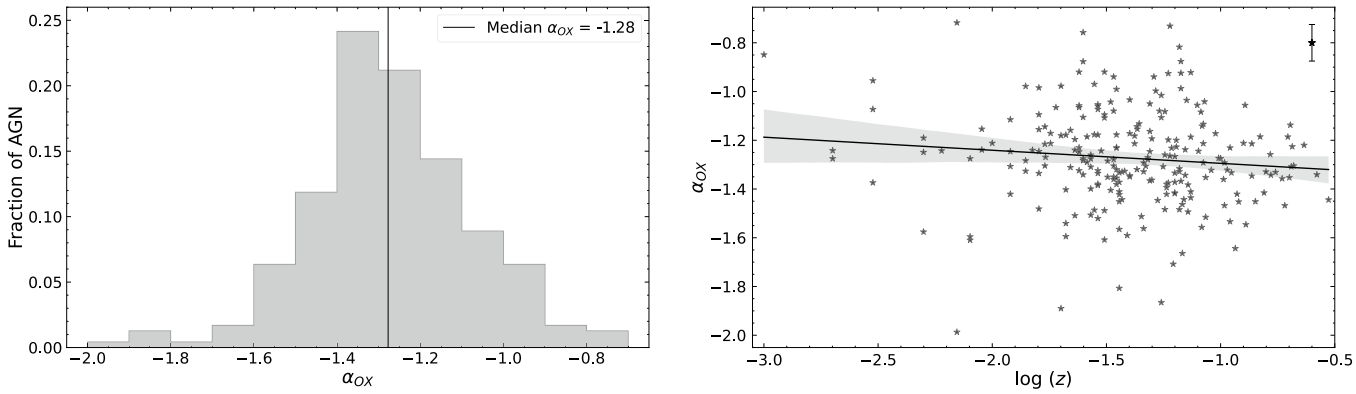

(a) (b)

Fig. 15. Optical-to-X-ray spectral index (α_{ox}) for our sample of hard-X-ray-selected nearby, unobscured AGN. (a) Distribution of α_{ox} and (b) α_{ox} as a function of redshift. The solid black line shows the best-fit linear relation to the data and the shaded gray region shows the uncertainty in the linear regression. We do not find any significant correlation between the two parameters. The typical errors on α_{ox} are shown on the top right corner (also valid for subsequent plots including α_{ox}).

In Fig. 16a, we show α_{ox} as a function of the monochromatic 2500 Å luminosity and the best-fit relation computed as follows:

$$\alpha_{ox} = (-0.105 \pm 0.011) \times \log(L_{2500\,\text{Å}}) + (1.745 \pm 0.315). \quad (7)$$

Grupe et al. (2010) found a similar slope (-0.114 ± 0.014) for their sample of soft-X-ray-selected AGN with simultaneous optical-to-X-ray SEDs. This relation is, however, shallower compared to the one estimated by Steffen et al. (2006; -0.137 ± 0.008) and Lusso et al. (2010; -0.154 ± 0.010), and steeper compared to Green et al. (2009; -0.061 ± 0.009) and Stalin et al. (2010; -0.065 ± 0.019). Additionally, when compared with higher redshift samples (up to $z \sim 5$), our slope is shallower than those reported by Timlin et al.(2020; -0.199 ± 0.011) and Timlin et al.(2021; -0.179 ± 0.013). Apart from sample selection and redshift effects mentioned previously, the difference in slopes could also be attributed to the fact that we cover lower luminosity regimes with our AGN sample. We have sources going down to 10^{25} erg s^{-1} Hz^{-1}, with ~25% sources below 10^{28} erg s^{-1} Hz^{-1}, which is almost three orders of magnitude below the luminosity range covered by most other works. In fact, we get a slightly shallower slope (-0.097 ± 0.018), which is comparable with Stalin et al. (2010), if we exclude the low luminosity sources ($<10^{28}$ erg s^{-1} Hz^{-1}). Lusso et al. (2010) also found a lower slope (-0.142 ± 0.012) for their photometrically selected sample that extends to lower luminosity values. This effect of having low luminosity sources in our sample is also prominent in Fig. 16b, where we plot α_{ox} as a function of the 2 keV monochromatic luminosity. In agreement with other works, we do not find any significant correlation between α_{ox} and $L_{2\,\text{keV}}$:

$$\alpha_{ox} = (-0.004 \pm 0.015) \times \log(L_{2\,\text{keV}}) + (-1.172 \pm 0.388). \quad (8)$$

However, even in this case, we go down to luminosities of 10^{22} erg s^{-1} Hz^{-1}, which is up to two orders magnitudes lower when compared to Steffen et al. (2006) and Lusso et al. (2010). This could explain the flatter slope we obtain for our best-fit regression relation compared to those inferred by Steffen et al. (2006; -0.077 ± 0.015) and Lusso et al. (2010; -0.019 ± 0.013). Our results are consistent with Green et al. (2009), who found a slope of -0.003 ± 0.010 for their main sample, but with a different intercept value (-1.384 ± 0.261).

Lastly, we check if there exists any dependence of α_{ox} on the Eddington ratio. A correlation between α_{ox} and λ_{Edd} was first reported by Lusso et al. (2010; although with a large dispersion), where they found that sources with higher λ_{Edd} showed higher ratios of UV to X-ray luminosity. This correlation was further confirmed by Grupe et al. (2010) and Jin et al. (2012), but with a flatter slope and a higher significance. On the contrary, Vasudevan et al. (2009) did not find any such relation for their sample of hard-X-ray-selected AGN. We illustrate the relation between α_{ox} and λ_{Edd} for our sample in Fig. 17a. We obtain a significant negative correlation (see Table 3) between the two quantities, where the best-fit linear regression is given as:

$$\alpha_{ox} = (-0.075 \pm 0.017) \times \log(\lambda_{Edd}) + (-1.374 \pm 0.026). \quad (9)$$

Our findings are in agreement with those of Grupe et al. (2010; -0.11 ± 0.02) and Jin et al. (2012; -0.079 ± 0.038). We find a shallower slope for the correlation, compared to Lusso et al. (2010; -0.133 ± 0.023), but with larger significance (p-value $= 2.42 \times 10^{-5}$). A possible reason for this could be that our sample consists of many low UV luminosity sources (similar to Grupe et al. 2010 and Jin et al. 2012), whereas the sample analyzed by Lusso et al. (2010) are majorly bright in the UV. As a result, they have many sources with $\alpha_{ox} < -1.5$ further increasing the dispersion in their relation. When compared to Vasudevan et al. (2009) who analyzed a sample of 26 low-absorption AGN, we have much better statistics (~1 dex improvement) that allows us to constrain this possible anticorrelation better. However, considering the large scatter visible in Fig. 17a and also reported in previous works, one should be cautious when using the $\alpha_{ox} - \lambda_{Edd}$ relation (Eq. (9)) to estimate λ_{Edd}. We also investigated whether α_{ox} correlates with either the black hole mass (M_{BH}) or the bolometric luminosity (L_{bol}). We do not find any significant correlation of α_{ox} with M_{BH}. However, we obtain an anticorrelation between α_{ox} and L_{bol} (Fig. 17b), with the best-fit relation as follows:

$$\alpha_{ox} = (-0.062 \pm 0.014) \times \log(L_{bol}) + (1.486 \pm 0.617). \quad (10)$$

This correlation is similar to the one obtained between α_{ox} and λ_{Edd} in terms of the slope (0.062 and 0.075), intercept (1.486 and 1.374), dispersion (~0.2), and significance (~10^{-5}), suggesting that the underlying physics responsible for these two relations could be the same and possibly related to the energy generation mechanism of AGN, where more luminous sources (with higher Eddington ratios, up to the Eddington limit) emit more in the UV relative to their X-ray emission.

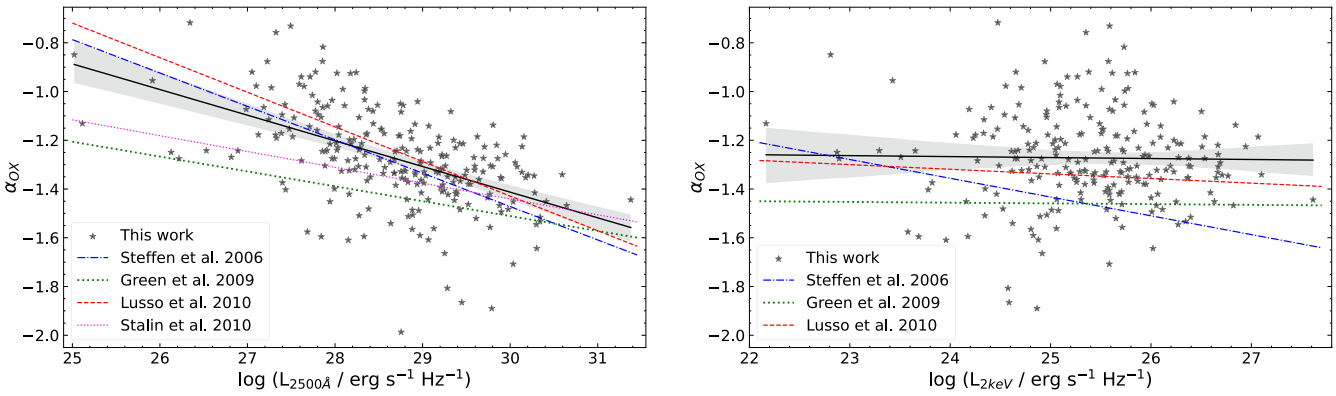

(a) (b)

Fig. 16. α_{ox} as a function of the rest-frame monochromatic luminosity at (a) 2500 Å (UV) and (b) 2 keV (X-ray). We find a tight anticorrelation between α_{ox} and $L_{2500\,Å}$ (shown as the solid black line in the left panel) but no significant relation with $L_{2\,keV}$ (shown as a solid black line in the right panel). For comparison, we also plot the best-fit relations from Steffen et al. (2006; dash-dotted blue line), Green et al. (2009; thick dotted green line), Lusso et al. (2010; dashed red line), and Stalin et al. (2010; dotted magenta line). The shaded gray region shows the one sigma confidence interval for our best-fit linear regression.

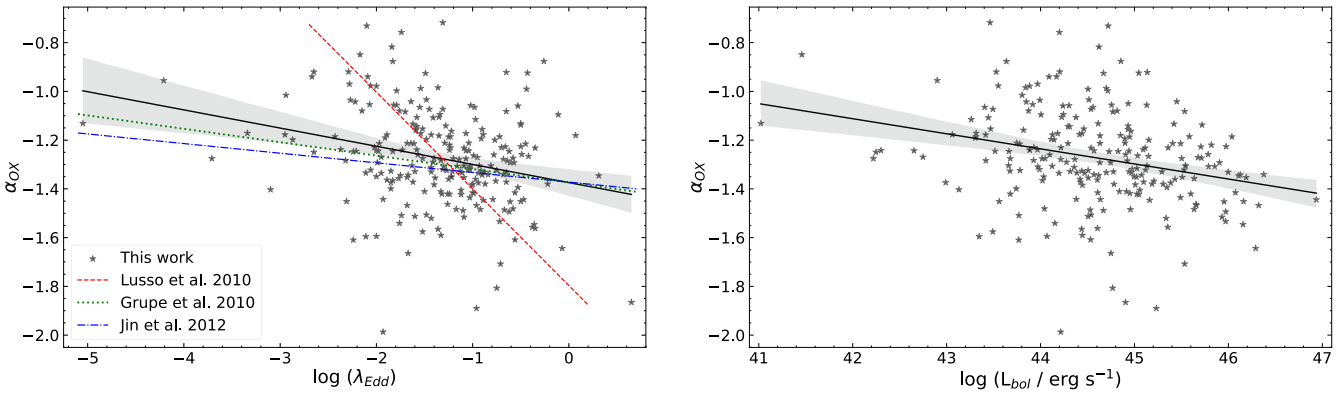

(a) (b)

Fig. 17. α_{ox} as a function of (a) Eddington ratio and (b) bolometric luminosity. We find a strong anticorrelation of α_{ox} with both the parameters (see Table 3). The solid black lines show our best-fit relations and the shaded gray regions are the one sigma confidence interval for each relation. Our linear relation between α_{ox} and λ_{Edd} is flatter when compared to the one reported by Lusso et al. (2010; dashed red line), but consistent with Grupe et al. (2010; dotted green line) and Jin et al. (2012; dash-dotted blue line).

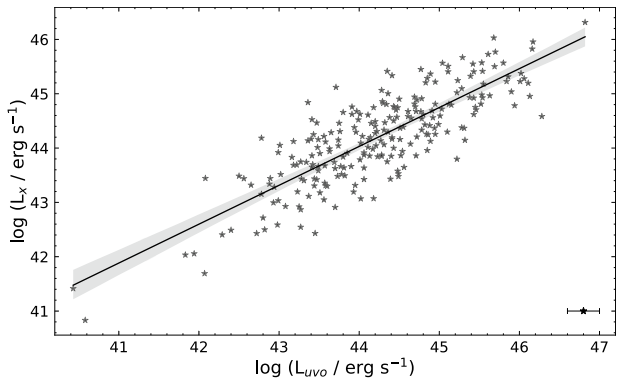

Fig. 18. Optical/UV disk luminosity (L_{uvo}) against the X-ray luminosity (L_X). The solid black line shows our best-fit relation and the shaded gray region is the one sigma confidence interval. The typical errors on L_x are less than 5% and those on L_{uvo} are shown in the bottom right corner.

The method of calculating α_{ox} using the luminosities at 2500 Å and 2 keV as representing the disk and coronal emission, respectively goes back to the 1970s (Schmidt 1968). However, over the years, we have managed to acquire observations over the entire electromagnetic spectrum, allowing us to constrain the total disk and coronal emission. Through this work, we provide a linear relation between the two major contributors of AGN emission as follows:

$$\log(L_x) = (0.716 \pm 0.032) \times \log(L_{uvo}) + (12.543 \pm 1.434). \quad (11)$$

This equation (also shown in Fig. 18) can be used to estimate either the disk luminosity from X-ray spectral fitting or the X-ray coronal luminosity if a fit disk model is available.

7.4. Bolometric corrections

We calculated the bolometric corrections in different energy bands by taking a ratio of the bolometric luminosity ($L_{bol} = L_x + L_{uvo}$) and the intrinsic luminosity in the specific energy range ($\kappa_\lambda = L_{bol}/L_\lambda$).

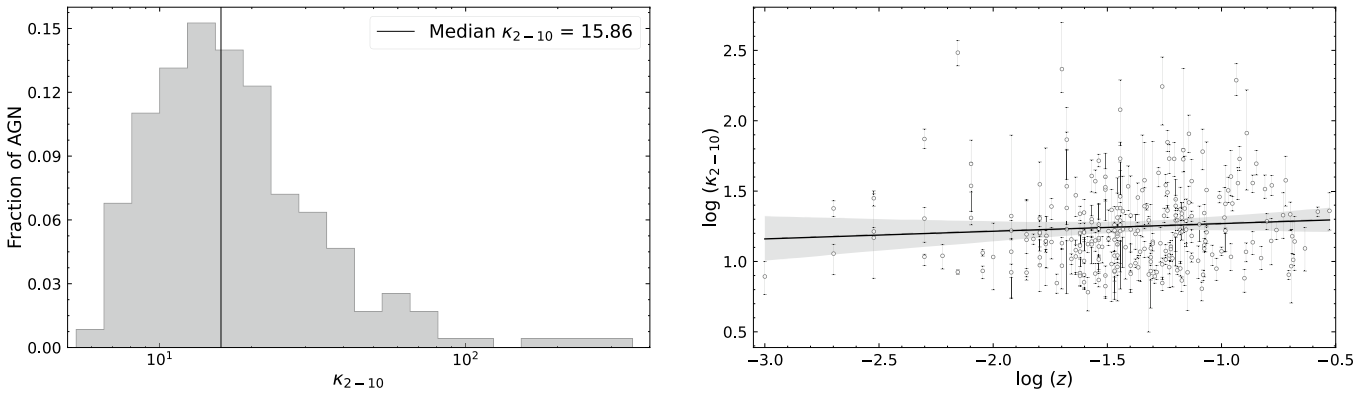

(a) (b)

Fig. 19. Soft X-ray bolometric correction (κ_{2-10}) for our sample of hard-X-ray-selected nearby, unobscured AGN. (a) Distribution of κ_{2-10} and (b) κ_{2-10} as a function of the redshift. The solid black line shows the best-fit relation to the data and the shaded gray region represents the uncertainty in the linear fit. We do not find any significant dependence of κ_{2-10} on redshift.

Table 3. Correlation results for Figs. 14, 15b, 16, 17, and 18, described in Sect. 7.3.

Correlation	R-Value [a]	P-Value [b]	Scatter (dex)
$L_{2\,\mathrm{keV}} - L_{2500\,\text{Å}}$	0.86	4.29×10^{-69}	0.45
$\alpha_{\mathrm{ox}} - z$	−0.11	0.09	–
$\alpha_{\mathrm{ox}} - L_{2500\,\text{Å}}$	−0.53	1.46×10^{-18}	0.15
$\alpha_{\mathrm{ox}} - L_{2\,\mathrm{keV}}$	−0.02	0.80	–
$\alpha_{\mathrm{ox}} - \lambda_{\mathrm{Edd}}$	−0.27	2.42×10^{-5}	0.17
$\alpha_{\mathrm{ox}} - L_{\mathrm{bol}}$	−0.28	1.21×10^{-5}	0.17
$L_{\mathrm{uvo}} - L_{\mathrm{x}}$	0.82	4.02×10^{-59}	0.50

Notes. We also report the one sigma dispersion (or scatter in dex) for parameters with significant correlations. [a]The Pearson's correlation coefficient. [b]The probability of the data set appearing if the null hypothesis is correct.

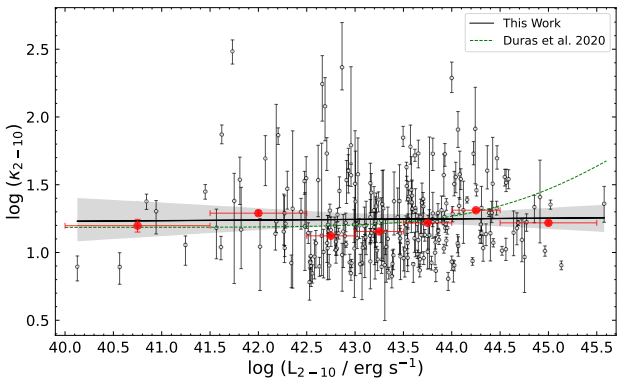

Fig. 20. 2–10 keV bolometric correction (κ_{2-10}) against the intrinsic 2–10 keV luminosity. The red points show the median value of κ_{2-10} in bins of L_{2-10}. The solid black line shows our best-fit relation and the shaded gray region is the one sigma confidence interval. The dashed green line shows the relation reported by Duras et al. (2020), which is consistent with our results up to $L_{2-10} \sim 10^{45}$ erg/s.

7.4.1. X-ray

For the X-rays, we report bolometric corrections in three energy bins, the 0.2–2 keV ($\kappa_{0.2-2}$), 2–10 keV (κ_{2-10}), and the 14–195 keV (κ_{14-195}). In this section we focus on κ_{2-10}, while the other two X-ray bolometric corrections are discussed in Sect. 7.4.3.

In Fig. 19a, we show the distribution in the values of κ_{2-10} for our sample (also see Table A.9). We do not find any dependence of κ_{2-10} on the redshift (Fig. 19b). We obtain a median value of $\kappa_{2-10} = 15.86 \pm 0.17$, albeit with scatter up to 0.3 dex. Compared to Vasudevan & Fabian (2009), who reported a median $\kappa_{2-10} = 20$, our median κ_{2-10} is slightly lower. A possible reason behind this could be the difference in the fitting techniques employed while fitting the optical/UV part of the SED. Even though we used the same disk model, in their analysis, Vasudevan & Fabian (2009) fixed the parameter corresponding to the normalization of the disk emission (given by Eq. (1)). For their models, they calculated K_{uvo} by substituting M with the black hole mass estimates from reverberation mapping, using the luminosity distances for D, and assuming the inclination angle to be 0 deg (for face-on disks of low-absorption AGN), and the color-to-effective temperature ratio to be unity. Fixing the normalization parameter can drastically affect the overall SED fitting as the only parameter left to vary is the disk temperature (discussed in Sect. 7.2.1). We further checked the implication of fixing the normalization by following the approach taken by Vasudevan & Fabian (2009) for our AGN sample and obtained higher values for κ_{2-10}, consistent with those reported by Vasudevan & Fabian (2009). However, once again, we do not recommend fixing the normalization in such disk models as that can strongly alter the SED fitting. Moreover, assuming a common inclination angle and color-to-temperature ratio for the entire sample could work for small samples like those analyzed by Vasudevan & Fabian (2009) and Vasudevan et al. (2009). But doing the same for a sample as large as ours cannot be justified and can severely bias the final results.

We also plot κ_{2-10} as a function of the intrinsic 2–10 keV luminosity in Fig. 20. Across five orders of magnitude in the X-ray luminosity, we do not see any significant trend in the value of κ_{2-10}. This is in agreement with Duras et al. (2020), who estimated $\kappa_{2-10} \sim 15-18$ for $\log(L_{2-10}/\mathrm{erg\,s^{-1}}) \sim 40-44$ and only find a significant increase in κ_{2-10} up to 30–70 for $\log(L_{2-10}/\mathrm{erg\,s^{-1}}) > 45$. Now although one might be tempted to just use the median value of κ_{2-10} to estimate the bolometric luminosity from the intrinsic 2–10 keV luminosity, we would like to emphasize that doing so could be problematic, owing to the visible scatter of ∼0.3 dex in κ_{2-10}. We confirm that this scatter is not due to sources with high Galactic extinction (∼20 sources have $E[B-V] > 0.3$). Moreover, the scatter cannot be

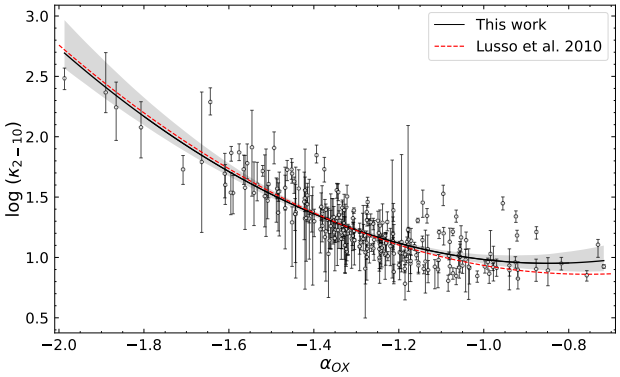

Fig. 21. 2–10 keV bolometric correction (κ_{2-10}) against α_{ox}. The solid black line shows the best-fit relation we obtained (Sect. 7.4.1, Table 4), which is in good agreement with the one estimated by Lusso et al. (2010; dashed red line). The shaded gray region shows the one sigma confidence interval for our best-fit relation.

due to variability as our analysis uses contemporaneous observations in the multiple bands. Hence, the scatter in κ_{2-10} is intrinsic to our AGN sample and could be due to either inclination angle or black hole spin, quantities not explicitly constrained in our SED fitting (see Sect. 6). Additionally, κ_{2-10} changes significantly with the bolometric luminosity and the Eddington ratio of the source, also confirmed by previous works (e.g., Vasudevan et al. 2009; Lusso et al. 2010; Duras et al. 2020). A detailed study of the main parameters regulating κ_{2-10} and how it correlates with various physical properties of AGN will be presented in Gupta et al. (in prep.).

Lusso et al. (2010) reported a strong correlation between κ_{2-10} and α_{ox}. This relation could be extremely useful considering that independent estimates of bolometric luminosities ($\kappa_\lambda \times L_\lambda$) require one to have access to a wealth of multiband data, whereas α_{ox} can be calculated from just the monochromatic luminosity at 2500 Å and 2 keV. Furthermore, the relation of κ_{2-10} with α_{ox} has a smaller scatter (0.15 dex) compared to the one with L_{2-10} mentioned above. In Fig. 21, we show this $\alpha_{ox} - \kappa_{2-10}$ relation obtained from our work, which is in excellent agreement with Lusso et al. (2010). The best-fit relation (shown as a solid black line in Fig. 21) between α_{ox} and κ_{2-10} is represented by a second-degree polynomial as follows:

$$\log(\kappa_{2-10}) = (1.339 \pm 0.143) \times \alpha_{ox}^2 + (2.267 \pm 0.370) \times \alpha_{ox} + (1.911 \pm 0.239). \quad (12)$$

7.4.2. Optical/UV

Based on the optical/UV wavelength regime of the broadband SED, we also calculated bolometric corrections in the optical and UV energy bands. In Table A.10, we list the optical/UV bolometric corrections in the six *Swift*/UVOT filters (V, B, U, UVW1, UVM2, and UVW2). These bolometric corrections were calculated by taking a ratio of the bolometric luminosity and the intrinsic luminosity in the corresponding *Swift*/UVOT waveband (L_λ; wavelength range for each band is listed in Table 1). We also report the 4400 Å bolometric correction ($\kappa_{4400\,Å} = L_{bol}/L_{4400\,Å}$; in the optical *B*-band) as has been done by many previous works (e.g., Hopkins et al. 2007; Lusso et al. 2012; Shen et al. 2020; Duras et al. 2020). First, we explore if these bolometric corrections change with redshift and do not find any significant dependence of κ_λ on z. Since we do not expect the energy generation mechanism of AGN to change over such a small redshift range as that of our sample ($0.001 < z < 0.3$), absence of a correlation between κ_λ and z further confirms that our SED analysis is consistent throughout the redshift range of our sample. Even though the *Swift*/BAT AGN sample is flux-limited, due to which the farthest sources are the faintest and we had to apply corrections to the GALFIT-estimated AGN fluxes (described in Sect. 5.3) for the sources above $z = 0.05$, our results are not influenced by it. This also verifies that the corrections that we calculated for GALFIT fluxes did not introduce any biases to our analysis.

Next, we check if any of the optical/UV bolometric correction factors show a dependence on L_λ, L_{bol}, M_{BH}, or λ_{Edd}. We first focus on $\kappa_{4400\,Å}$ so as to compare our results with other similar studies from the literature. In Fig. 22, we show $\kappa_{4400\,Å}$ as a function of $L_{4400\,Å}$ and L_{bol}. In agreement with past studies (e.g., Lusso et al. 2012; Duras et al. 2020), we do not find any significant correlation of $\kappa_{4400\,Å}$ with either the intrinsic monochromatic luminosity at 4400 Å or the bolometric luminosity (see Table 4). Shen et al. (2020), however, reported a luminosity dependent $\kappa_{4400\,Å}$, as they found higher values of $\kappa_{4400\,Å}$ for lower luminosity sources ($L_{bol} < 10^{44}$ erg/s). This dependence can be attributed to the fact that they used the observed luminosity (instead of the intrinsic luminosity) at 4400 Å to calculate $\kappa_{4400\,Å}$, due to which the lower luminosity sources that are affected by possible extinction from the surrounding material would have higher $\kappa_{4400\,Å}$ due to lower values of observed $L_{4400\,Å}$. Whereas, the higher luminosity sources ($L_{bol} > 10^{44}$ erg/s) have $\kappa_{4400\,Å}$ values similar to ours. Hence, we recommend the constant value fit that gives a value of $\kappa_{4400\,Å} = 7.9 \pm 0.3$. Additionally, $\kappa_{4400\,Å}$ also does not show any dependence on M_{BH} or λ_{Edd}. Lastly, we investigate the same trends for the bolometric correction factors in the six *Swift*/UVOT filters (κ_V, κ_B, κ_U, κ_{W1}, κ_{M2}, and κ_{W2}). In the following part of the discussion, we first report all our findings and then later discuss their physical implications.

In Fig. 23, we show the optical/UV bolometric corrections against the intrinsic luminosity in their respective filters and in Figs. 24 and 25, we show their dependence on the bolometric luminosity and the Eddington ratio, respectively. Similar to $\kappa_{4400\,Å}$, κ_B ($\lambda_B = 4392$ Å) does not show any correlation with L_B, L_{bol}, M_{BH}, or λ_{Edd} (top right panel in Figs. 23, 24, and 25). Bolometric corrections of the highest-energy optical filter U and the lowest-energy UV filter W1 show a strong negative correlation with the intrinsic luminosities in their respective bands (middle panel in Fig. 23, Tables 4 and 5). They do not show dependence on any other properties of the AGN. The *V* filter bolometric correction factor shows a weak positive correlation with the bolometric luminosity and the Eddington ratio (top left panel in Figs. 24 and 25). The bolometric corrections for the high-energy UV filters, κ_{M2} and κ_{W2}, show significant anticorrelations with the intrinsic luminosities in their respective energy bands (bottom panel in Fig. 23, Tables 4 and 5) and with λ_{Edd} (bottom panel in Fig. 25, Tables 4 and 5), while κ_{W2} also shows a strong dependence on L_{bol} (see lower right panel in Fig. 24 and Tables 4 and 5). They do not show any dependence on M_{BH}.

Based on the trends mentioned above, we can draw some important conclusions. Firstly, we should pay attention to how the lowest-energy bolometric corrections (κ_V and κ_B) do not correlate with any physical properties of the AGN. While those at the highest energies (κ_{M2} and κ_{W2}) show strong correlations with our parameters of interest, except black hole mass. Studies have shown that compared to a disk model based on single-temperature blackbody emission, a multi-temperature accretion disk model better describes the optical/UV spectrum of AGN (e.g., Shields 1978; Malkan 1983). Assuming the disk to have a

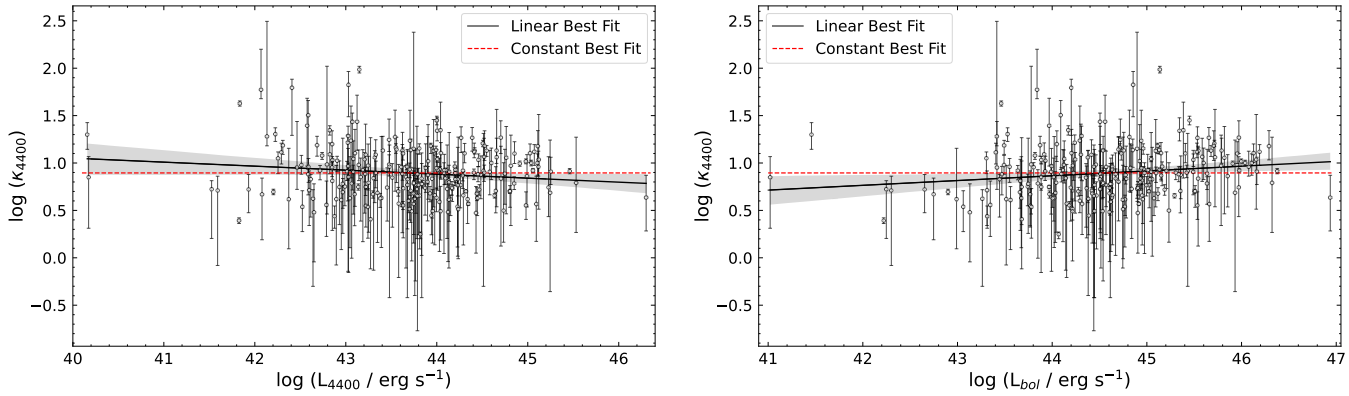

(a) (b)

Fig. 22. 4400 Å bolometric correction as a function of (a) the 4400 Å monochromatic luminosity and (b) the bolometric luminosity. We find a very weak correlation in both cases (Sect. 7.4.2, Table 4) shown as the black line. Hence, we show the best fit with a constant value as well (dashed red line). For both cases, we get a value of $\kappa_{4400\,\text{Å}} = 7.9 \pm 0.3$.

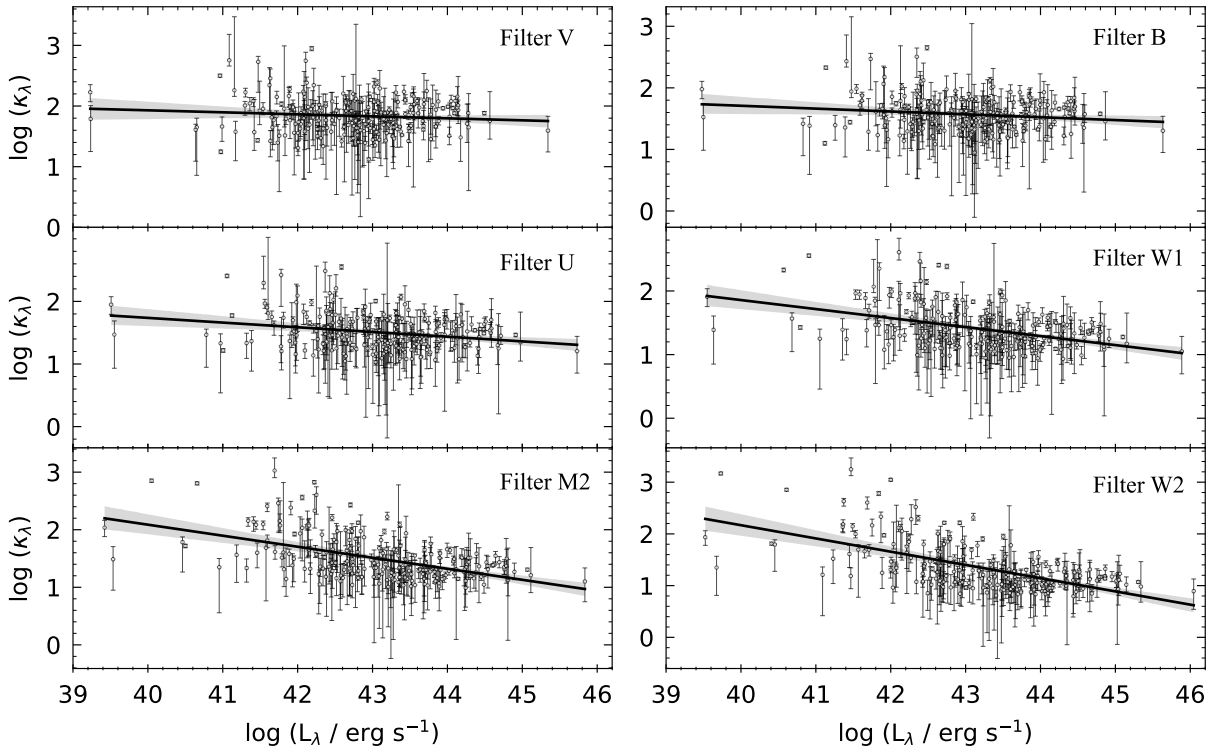

Fig. 23. Six optical/UV bolometric corrections as a function of the intrinsic luminosity in their respective filters. The solid lines show our best-fit relations. A significant anticorrelation with luminosity is observed for bolometric corrections in the filters U, W1, M2, and W2. This dependence is stronger as we go to higher energies (Sect. 7.4.2, Table 4).

radial temperature profile [$T_{\rm eff}(R) \propto R^{-p}$; $p = 0.75$ for the standard Shakura & Sunyaev (1973) disk], with smaller radii being at higher temperatures, we naturally expect the highest-energy UV photons to originate mainly in the inner regions of the accretion disk, much closer to the central SMBH. Whereas, the cooler outer regions of the disk would mainly emit the lower-energy optical photons (e.g., Collier et al. 1998; Sergeev et al. 2005). This effect of the gradient in the disk temperature with distance from the central black hole on the wavelength of the emitted photons has been discussed in detail by several studies on reverberation mapping, where time lag measurements between different continuum wavelengths (wavelength-dependent lags) have been used to estimate the size of the accretion disk and other inner regions of AGN (e.g., Cackett et al. 2007; also see Cackett et al. 2021 for a review). Many such studies estimated accretion disk sizes to be larger than what is expected from the Shakura & Sunyaev (1973) disk model and some of them argued that a possible reason for this could be the diffused emission from the larger BLR contributing to the photometric measurements, especially in the optical (e.g., Cackett et al. 2018, 2022; Chelouche et al. 2019). In this situation, we cannot be certain that the lower energy band of the broadband SED is solely dominated by emission arising in the disk without substantial contamination from the more extended regions. Hence explaining why the corresponding bolometric corrections are not strongly correlated with properties of the AGN, such as their total energy

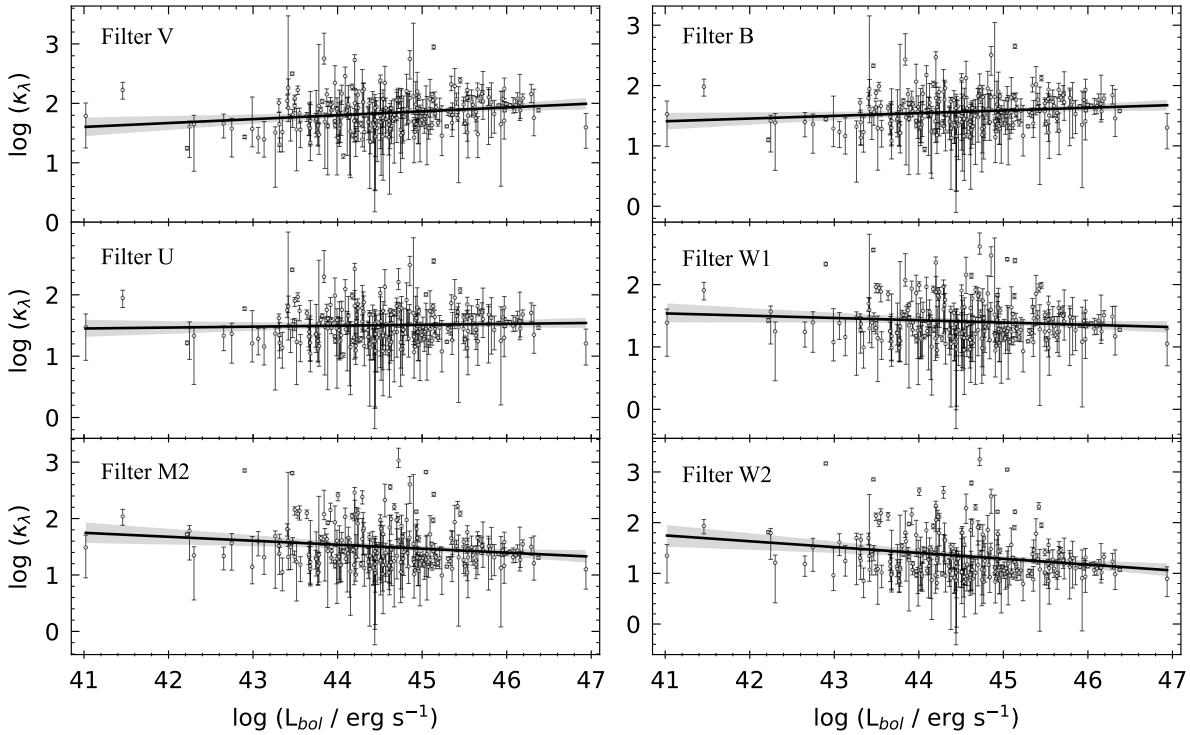

Fig. 24. Six optical/UV bolometric corrections as a function of the bolometric luminosity. The solid lines show the best-fit relations. We only find a significant correlation with $L_{\rm bol}$ for the highest-energy UV filter W2 (Sect. 7.4.2, Table 4).

output (from accretion) or their mass normalized accretion rate. On the contrary, the higher-energy UV bands predominately trace the accretion disk emission and therefore, the corresponding κ_λ correlate with quantities like $\lambda_{\rm Edd}$ (proxy of the accretion rate) and $L_{\rm bol}$ (total emission of the AGN). The observed negative correlation suggests that sources with larger accretion luminosities have more emission coming from the low wavelength, high-energy disk photons produced at shorter radii, and this is evident in the lower values of κ_λ for these sources.

Secondly, we consistently do not find a dependence on $M_{\rm BH}$ for any of the optical/UV (or X-ray) bolometric corrections. This indicates that the mass of the central SMBH does not control or influence the total radiation emitted by the accreting material at different wavelengths probed here. The main driving factor here is in fact the Eddington ratio. This emphasizes the importance and requirement of detailed studies of AGN physics in different regimes of $\lambda_{\rm Edd}$. Finally, a significant scatter is visible in all optical/UV bolometric corrections (~0.1–1 dex; see Table 6). Similar to the X-ray bolometric correction (κ_{2-10}), we confirm that this scatter is not due to sources with high Galactic extinction and would like to reiterate the importance of including the respective scatters while calculating $L_{\rm bol}$ from κ_λ for individual sources, to avoid miscalculations. We report the median values for all the optical/UV bolometric corrections, with uncertainties and dispersions, in Table 6. We also provide scaling relations of all the optical/UV bolometric corrections with $\alpha_{\rm ox}$ in Table 7.

7.4.3. Additional

In this section we list some additional bolometric corrections calculated in this work that could be useful to estimate bolometric luminosities depending on the data at hand. In the X-rays, we report the values of bolometric correction in the 0.2–2 keV (soft X-rays: $\kappa_{0.2-2}$) and the 14–195 keV (hard X-rays: κ_{14-195}) energy bands. We obtain a median value of $\kappa_{0.2-2} = 17.4 \pm 0.3$ and $\kappa_{14-195} = 6.0 \pm 0.1$. Similar to κ_{2-10} (see Sect. 7.4.1), $\kappa_{0.2-2}$ stays constant with the 0.2–2 keV intrinsic luminosity across five orders of magnitude ($10^{40} < L_{0.2-2}/{\rm erg\,s^{-1}} < 10^{45}$). However, for the hard X-ray bolometric correction, an anticorrelation is recovered between κ_{14-195} and L_{14-195} (see Fig. 26 and Table 4). This could probably just be an obvious consequence of how we define bolometric corrections and because of the large range of this specific energy band. The best-fit relation (shown as a black line in Fig. 26) is defined as follows:

$$\log(\kappa_{14-195}) = (-0.11 \pm 0.03) \times \log(L_{14-195}) + (5.55 \pm 1.20). \quad (13)$$

We checked if $\kappa_{0.2-2}$ and κ_{14-195} correlate with any other physical properties of AGN, such as $L_{\rm bol}$, $M_{\rm BH}$, and $\lambda_{\rm Edd}$. We found a significant dependence of both $\kappa_{0.2-2}$ and κ_{14-195} on $L_{\rm bol}$ and $\lambda_{\rm Edd}$ (shown in Figs. 27 and 28, respectively and Table 4). The best-fit linear regressions (shown as black lines) are as follows:

$$\log(\kappa_{0.2-2}) = (0.13 \pm 0.03) \times \log(L_{\rm bol}) + (-4.33 \pm 1.16) \quad (14)$$

$$\log(\kappa_{0.2-2}) = (0.11 \pm 0.03) \times \log(\lambda_{\rm Edd}) + (1.43 \pm 0.05) \quad (15)$$

$$\log(\kappa_{14-195}) = (0.08 \pm 0.03) \times \log(L_{\rm bol}) + (-2.82 \pm 1.26) \quad (16)$$

$$\log(\kappa_{14-195}) = (0.13 \pm 0.04) \times \log(\lambda_{\rm Edd}) + (1.04 \pm 0.05). \quad (17)$$

We also provide scaling relations of $\alpha_{\rm ox}$ with both $\kappa_{0.2-2}$ and κ_{14-195} in Table 7.

In the optical/UV wavelength bands, we report three additional bolometric corrections at 2500 Å ($\kappa_{2500\,\text{Å}}$), 3000 Å ($\kappa_{3000\,\text{Å}}$), and 5100 Å ($\kappa_{5100\,\text{Å}}$). The median values with errors and dispersions are listed in Table 6. We also list the corresponding coefficients for the best-fit relation with $\alpha_{\rm ox}$ in Table 7.

8. Summary and conclusion

In this paper, we present one of the largest studies to date of optical-to-X-ray wavelength SEDs for a sample of

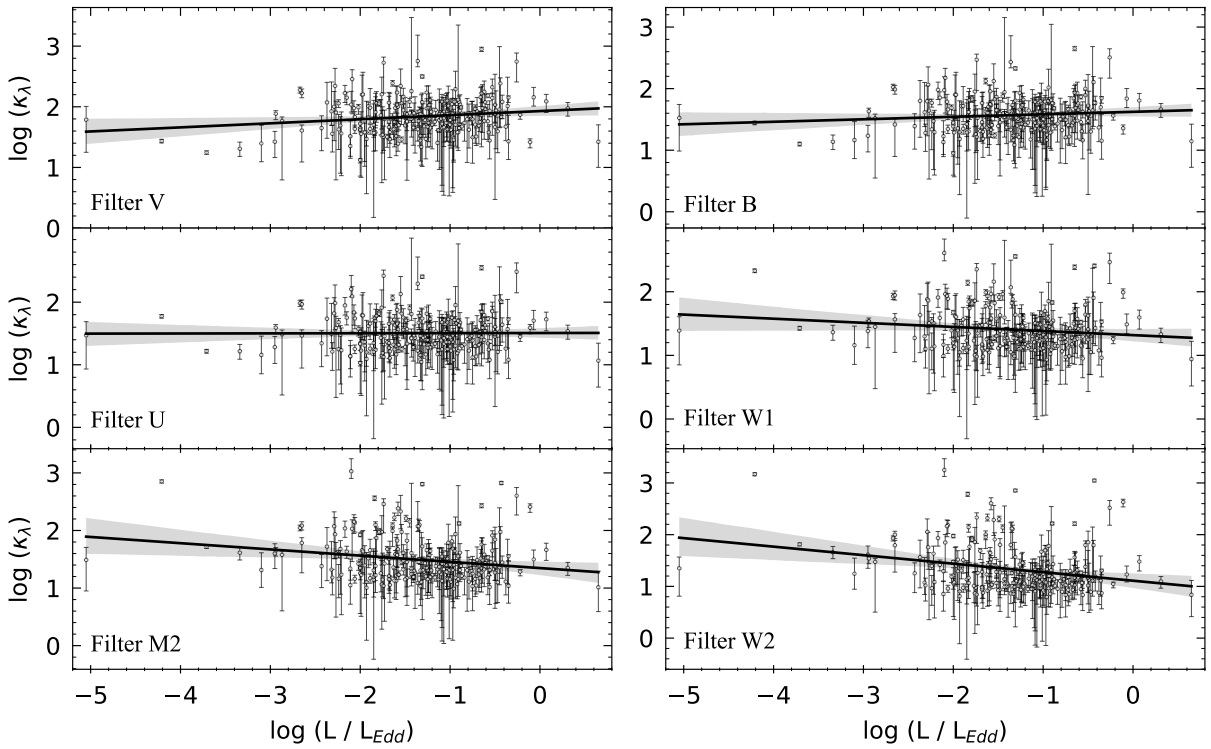

Fig. 25. Six optical/UV bolometric corrections as a function of the Eddington ratio. The solid lines show the best-fit relations. We only find a significant correlation with $\lambda_{\rm Edd}$ for the highest-energy UV filters M2 and W2 (Sect. 7.4.2, Table 4).

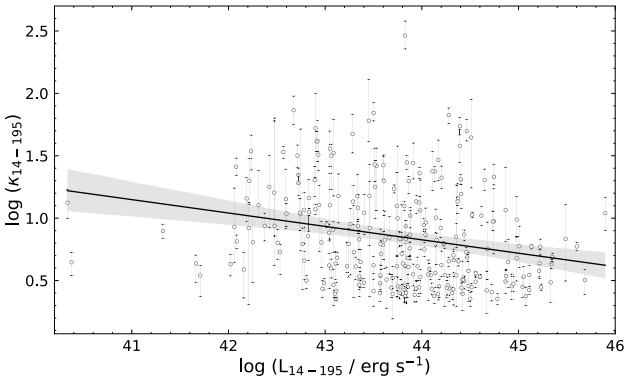

Fig. 26. 14–195 keV bolometric correction (κ_{14-195}) against the intrinsic luminosity in the 14–195 keV energy bin (L_{14-195}). The solid black line shows the best-fit relation we obtained (Sect. 7.4.3, Table 4). The shaded gray region shows the one sigma confidence interval for our best-fit relation.

236 unobscured, hard-X-ray-selected, nearby AGN from the 70-month *Swift*/BAT catalog. We compiled simultaneous optical, UV, and X-ray observations for all sources to mitigate any issues arising due to differences in the variability timescales at different wavelengths. We extracted the 0.3–10 keV X-ray spectra and magnitudes and fluxes in the six *Swift*/UVOT filters: V, B, U, UVW1, UVM2, and UVW2 for all our sources. We corrected the optical/UV fluxes for galactic dust extinction as well as host galaxy contamination. The latter was done by fitting the 2D surface brightness of the source images using a PSF and a Sérsic profile with GALFIT to fit the AGN and the host galaxy, respectively. We also performed numerous simulations by creating fake populations of type I AGN and fitting them using GALFIT, to quantitatively inspect the reliability of the AGN magnitudes calculated by GALFIT. As a result of these simulations, we were able to calculate correction factors in each of the six *Swift*/UVOT filters, which can be used to correct the GALFIT-estimated PSF fluxes. We constructed and fit the multiwavelength AGN SEDs (10^{-7} to 500 keV) using a dust-reddened multi-temperature blackbody to model the optical/UV accretion disk and a variety of X-ray models consisting of multiple components to account for the primary X-ray emission and the reprocessed secondary emission. We then used the best-fit SED models to calculate important quantities used to describe AGN properties, such as the total accretion luminosity or bolometric luminosity of our sources, intrinsic optical, UV, and X-ray luminosities, optical-to-X-ray spectral indices, multiwavelength bolometric corrections, and Eddington ratios. Compared to similar past studies (e.g., Vasudevan & Fabian 2009; Vasudevan et al. 2009), we have improved the sample size by almost one dex, and hence expanded the range of luminosities and Eddington ratios that can be probed (both span five orders of magnitude), adopted improved SED fitting techniques, and implemented more detailed procedures to remove contamination due to the host galaxy to AGN light in the optical/UV using GALFIT. The main results of this study are summarized as follows:

– We report total aperture optical/UV source magnitudes (Table A.4) and fluxes (Table A.3), along with errors, in the six *Swift*/UVOT filters (Sect. 3.1) for all 292 unobscured AGN in our original sample. For the final sample of 236 sources, we report AGN magnitudes (Table A.7) and fluxes (Table A.6) devoid of the host galaxy light, estimated from the image decomposition and three-component fitting done using GALFIT (Sect. 5). The results of our X-ray spectral fitting in the 0.3–10 keV band (Sect. 4) are summarized in Table A.5, listing values of the photon index (Γ) and the intrinsic 2–10 keV X-ray flux for all AGN in our initial sample. Best-fit values of parameters from the optical/UV SED fitting (Sect. 6), such as

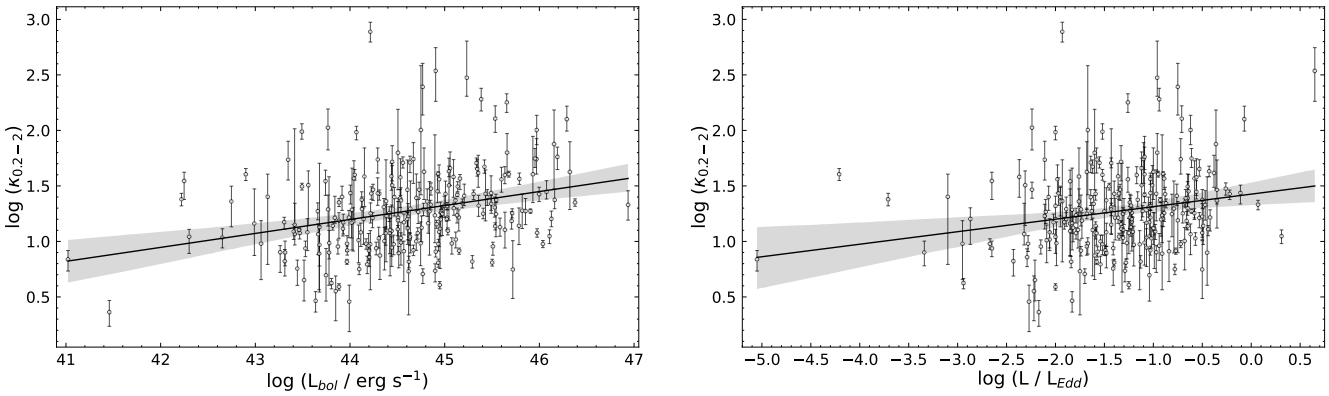

(a) (b)

Fig. 27. 0.2–2 keV bolometric correction as a function of (a) the bolometric luminosity and (b) the Eddington ratio. We find a significant correlation in both cases (Sect. 7.4.3, Table 4) shown as the black line. The shaded region is the one sigma confidence interval for the linear regression line.

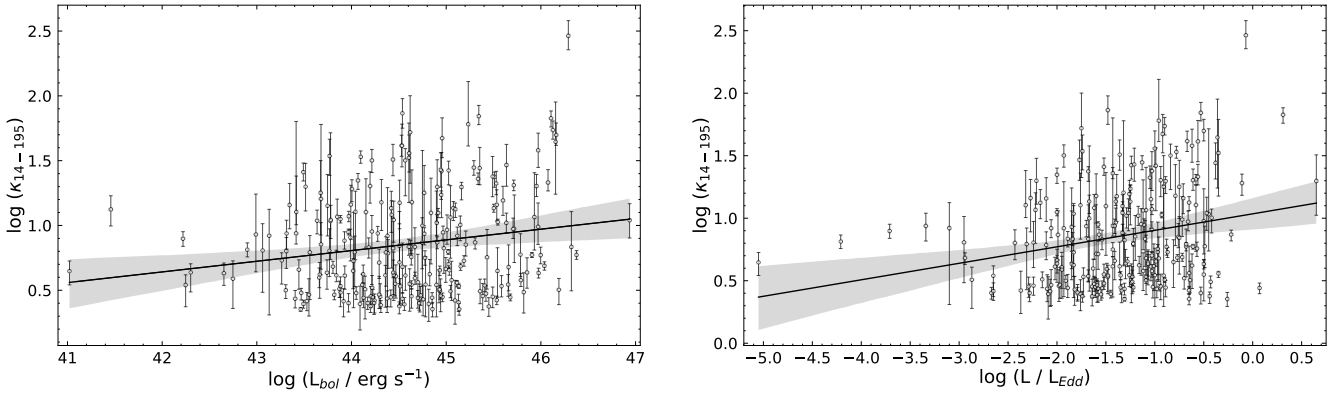

(a) (b)

Fig. 28. 14–195 keV bolometric correction as a function of (a) the bolometric luminosity and (b) the Eddington ratio. We find a significant correlation in both cases (Sect. 7.4.3, Table 4) shown as the black line. The shaded region is the one sigma confidence interval for the linear regression line.

the maximum disk temperature, host galaxy extinction, and the intrinsic flux in the optical + UV energy range (10^{-7} to 0.1 keV) are presented in Table A.8.

- Some important quantities, including monochromatic luminosities at 2500 Å and 2 keV, the optical-to-X-ray spectral index (α_{ox}), bolometric luminosity, black hole mass, and Eddington ratio, are reported for the 236 unobscured AGN in our sample in Table A.9. Eight different multiwavelength bolometric corrections are provided for all sources in Tables A.9 and A.10, and their median values with uncertainties are also given in Table 6.
- We confirm the strong correlation observed between the X-ray and UV monochromatic luminosity at 2 keV and 2500 Å for AGN, given by $L_{2\,keV} \propto L^{\beta}_{2500\,Å}$ with $\beta = 0.850 \pm 0.013$ (Eq. (6), Fig. 14).
- We calculated the optical-to-X-ray spectral index for our AGN sample, finding a median $\alpha_{ox} = -1.28$. We find no dependence of α_{ox} on redshift or $L_{2\,keV}$ (Figs. 15b and 16b), and confirm the strong anticorrelation between α_{ox} and $L_{2500\,Å}$ (Eq. (7), Fig. 16a). We find weak anticorrelations between α_{ox} and both λ_{Edd} and L_{bol} (Eqs. (9) and (10), Fig. 17), and no correlation with M_{BH}.
- We computed 2–10 keV X-ray bolometric corrections for our unobscured AGN sample, finding a median $\kappa_{2-10} = 15.9 \pm 0.2$. We obtained a scatter of 0.3 dex at one sigma in the value of κ_{2-10} for our AGN sample (Fig. 20), which could be due to quantities such as the inclination angle and/or black hole spin that were not constrained in our SED fitting. More findings on how κ_{2-10} relates to AGN properties will be presented in a forthcoming dedicated paper.
- We present a tight (scatter = 0.15 dex) second-order relation between κ_{2-10} and α_{ox}, which can be useful to calculate L_{bol} in the absence of multiband data, solely from the intrinsic, monochromatic luminosities at 2 keV and 2500 Å (Eq. (12), Fig. 21).
- For the optical/UV energies, we list seven different bolometric corrections: the 4400 Å optical bolometric correction and one for each of the six *Swift*/UVOT filters. None of these κ_{λ} show any dependence on redshift, which negates any biases due to redshift in our SED fitting analysis. We explore if and how these optical/UV bolometric corrections correlate with different physical properties of AGN. Our main finding is that the highest-energy UV bolometric corrections (κ_{M2} and κ_{W2}) show significant negative correlations with both L_{bol} and λ_{Edd}, while the lowest-energy ones (κ_V, κ_B, and $\kappa_{4400\,Å}$) show no clear dependence on any of the AGN accretion properties (Figs. 24 and 25, Tables 4 and 5). This result can be explained if we assume the following:

Table 4. Correlation results for Figs. 19b, 20, 21, 22, 23, 24, 25, 26, 27, and 28, described in Sect. 7.4.

Correlation	R-Value [(a)]	P-Value [(b)]	Scatter (dex)
$\kappa_{2-10} - z$	0.08	0.25	–
$\kappa_{2-10} - L_{2-10}$	0.13	0.84	–
$\alpha_{ox} - \kappa_{2-10}$	−0.86	6.51×10^{-69}	0.15 [(c)]
$\kappa_{4400\,Å} - L_{4400\,Å}$	−0.14	0.03	–
$\kappa_{4400\,Å} - L_{bol}$	0.15	0.02	–
$\kappa_U - L_U$	−0.25	9.50×10^{-5}	0.27
$\kappa_{W1} - L_{W1}$	−0.42	9.86×10^{-12}	0.30
$\kappa_{M2} - L_{M2}$	−0.52	2.24×10^{-17}	0.33
$\kappa_{W2} - L_{W2}$	−0.61	6.09×10^{-25}	0.37
$\kappa_{W2} - L_{bol}$	−0.22	5.80×10^{-4}	0.45
$\kappa_{M2} - \lambda_{Edd}$	−0.20	1.80×10^{-3}	0.38
$\kappa_{W2} - \lambda_{Edd}$	−0.26	7.68×10^{-5}	0.45
$\kappa_{0.2-2} - L_{bol}$	0.30	2.56×10^{-6}	0.36
$\kappa_{0.2-2} - \lambda_{Edd}$	0.22	8.43×10^{-4}	0.37
$\kappa_{14-195} - L_{14-195}$	−0.25	1.19×10^{-4}	0.38
$\kappa_{14-195} - L_{bol}$	0.19	3.80×10^{-3}	0.39
$\kappa_{14-195} - \lambda_{Edd}$	0.24	1.91×10^{-4}	0.38

Notes. We also report the one sigma dispersion (or scatter in dex) for parameters with significant correlations. [(a)]The Pearson's correlation coefficient. [(b)]The probability of the data set appearing if the null hypothesis is correct. [(c)]Best-fit achieved using a second-order polynomial.

Table 5. Coefficients for the best-fit relation of various optical/UV bolometric corrections (κ_λ) with the intrinsic luminosity in their respective bands (L_λ), the bolometric luminosity (L_{bol}), and the Eddington ratio (λ_{Edd}), described in Sect. 7.4.2.

Correlation	A	B
$\kappa_U - L_U$	−0.07 ± 0.02	4.74 ± 0.81
$\kappa_{W1} - L_{W1}$	−0.14 ± 0.02	7.52 ± 0.85
$\kappa_{M2} - L_{M2}$	−0.19 ± 0.02	9.75 ± 0.90
$\kappa_{W2} - L_{W2}$	−0.26 ± 0.02	12.41 ± 0.95
$\kappa_{W2} - L_{bol}$	−0.12 ± 0.03	6.47 ± 1.47
$\kappa_{M2} - \lambda_{Edd}$	−0.11 ± 0.03	1.35 ± 0.05
$\kappa_{W2} - \lambda_{Edd}$	−0.16 ± 0.04	1.11 ± 0.06

Notes. The format for the linear relations is: $\log(y) = A \times \log(x) + B$, where y is κ_λ and x is either L_λ, L_{bol}, or λ_{Edd}.

(a) the standard Shakura & Sunyaev (1973) disk model with a multi-temperature blackbody emission, and (b) possible contamination in the lower-energy optical photometric bands from the diffused emission produced in the BLR (Sect. 7.4.2). Furthermore, the lack of any kind of dependence of κ_λ on black hole mass implies that it is not in any way a controlling factor for the amount of radiation emitted via accretion among the wavelength ranges probed here.

– Our results show significant scatter (∼0.1–1 dex) in all bolometric correction factors (Table 6). This scatter cannot be attributed either to sources with high Galactic extinction or to different variability timescales between the multiwavelength emission of AGN. We therefore strongly recommend the inclusion of the reported dispersion values while calculating L_{bol} from κ_λ for individual sources and the use of appropriate scaling relations of κ_λ when carrying out population studies.

Table 6. Median values of all the X-ray and optical/UV bolometric corrections with respective uncertainties and one sigma dispersions (Sect. 7.4).

κ_λ	Median Value	Errors	Dispersion (dex)
κ_{2-10}	15.9	0.16	0.30
$\kappa_{4400\,Å}$	7.9	0.32	0.10
κ_V	65.4	0.47	0.14
κ_B	35.5	0.25	0.12
κ_U	29.3	0.22	0.16
κ_{W1}	21.4	0.27	0.38
κ_{M2}	24.0	0.60	0.67
κ_{W2}	15.2	0.96	1.07
$\kappa_{0.2-2}$	17.4	0.33	0.56
κ_{14-195}	6.0	0.12	0.57
$\kappa_{2500\,Å}$	5.7	0.09	0.45
$\kappa_{3000\,Å}$	6.0	0.05	0.22
$\kappa_{5100\,Å}$	8.8	0.06	0.13

Notes. Using the median bolometric corrections without appropriately including the dispersions in their values could lead to errors in calculations. The dispersion in dex lists the typical errors in estimating L_{bol} when using a monochromatic indicator (κ_λ) for a single source. Kindly refer to Sect. 7.4 for more details.

Table 7. Coefficients for the best-fit relation of various bolometric corrections with the optical-to-X-ray spectral index (α_{ox}) described in Sect. 7.4.

κ_λ	A	B	C
κ_{2-10}	1.34 ± 0.14	2.27 ± 0.37	1.91 ± 0.24
$\kappa_{4400\,Å}$	0.78 ± 0.07	1.89 ± 0.09	–
κ_V	0.68 ± 0.08	2.71 ± 0.10	–
κ_B	0.82 ± 0.07	2.61 ± 0.09	–
κ_U	0.87 ± 0.18	3.26 ± 0.45	4.20 ± 0.29
κ_{W1}	1.44 ± 0.16	5.04 ± 0.42	5.44 ± 0.27
κ_{M2}	1.81 ± 0.18	6.21 ± 0.48	6.40 ± 0.31
κ_{W2}	2.27 ± 0.24	7.67 ± 0.61	7.34 ± 0.39
$\kappa_{0.2-2}$	1.86 ± 0.25	3.58 ± 0.66	2.75 ± 0.43
κ_{14-195}	−1.22 ± 0.10	−0.70 ± 0.13	–
$\kappa_{2500\,Å}$	1.54 ± 0.17	5.37 ± 0.43	5.12 ± 0.28
$\kappa_{3000\,Å}$	1.09 ± 0.16	3.94 ± 0.42	4.04 ± 0.27
$\kappa_{5100\,Å}$	0.72 ± 0.08	1.88 ± 0.10	–

Notes. The format for linear relations is: $\log(\kappa_\lambda) = A \times \alpha_{ox} + B$ and the format for a second-degree best-fit relation is: $\log(\kappa_\lambda) = A \times \alpha_{ox}^2 + B \times \alpha_{ox} + C$.

Through this large multiwavelength study, we have attempted to perform a comprehensive broadband SED fitting analysis of a representative sample of AGN in the local Universe, to provide the community estimates of some useful quantities, such as bolometric luminosities, Eddington ratios, optical-to-X-ray spectral indices, and multiband bolometric corrections, as well as some important relations between these quantities. Given the time and resources, we have made an effort to keep this study as exhaustive as possible by including appropriate tools to take into account possible sources of errors that might affect our analysis, including AGN variability, dust extinction, and host galaxy contamination. We have also tried to demonstrate here the important role such studies can play in improving our knowledge about the accretion and emission mechanisms in AGN. With the wealth of available archival data and by employing more sophisticated

theoretical and computational models, we can also extract information about the host galaxy. To give a few examples, there exist SED fitting codes such as CIGALE/X-CIGALE (Noll et al. 2009; Boquien et al. 2019; Yang et al. 2020, 2022), AGNFITTER (Calistro Rivera et al. 2016; Martínez-Ramírez et al. 2024), or FORTESFIT (Rosario et al. 2018), AGN-galaxy templates provided by Richards et al. (2006), Assef et al. (2010), or Temple et al. (2021), and theoretical accretion disk models (e.g., Done et al. 2012; Slone & Netzer 2012) that can simultaneously constrain the star formation history of the host galaxy and the accretion properties of the AGN (e.g., accretion rates and efficiency). An extensive effort in this direction could prove to be an interesting milestone in our understanding of the AGN-galaxy coevolution scenario. Two such studies are ongoing: one is focused on modeling the X-ray-to-far-IR SEDs of the BASS DR2 AGN using CIGALE (Rojas et al., in prep.) and the other on modeling our optical-to-X-ray SEDs using Done et al. (2012) models (Kallová et al., in prep.).

Data availability

All the optical-to-X-ray SED fits generated in this work are available here. Full versions of Tables A.1 to A.10 are available at the CDS via anonymous ftp to `cdsarc.cds.unistra.fr` (`130.79.128.5`) or via `https://cdsarc.cds.unistra.fr/viz-bin/cat/J/A+A/691/A203`

Acknowledgements. We would like to thank the anonymous referee for their useful suggestions that helped improve this manuscript. This work made use of data from the NASA/IPAC Infrared Science Archive and NASA/IPAC Extragalactic Database (NED), which are operated by the Jet Propulsion Laboratory, California Institute of Technology, under contract with the National Aeronautics and Space Administration. This research has made use of data and/or software provided by the High Energy Astrophysics Science Archive Research Center (HEASARC), which is a service of the Astrophysics Science Division at NASA/GSFC and the High Energy Astrophysics Division of the Smithsonian Astrophysical Observatory. This research also made use of `photutils`, an Astropy package for the detection and photometry of astronomical sources (Bradley et al. 2021). We acknowledge financial support from: a 2018 grant from the ESO-Government of Chile Joint Committee (KKG); the Belgian Federal Science Policy Office (BELSPO) in the framework of the PRODEX Programme of the European Space Agency (KKG); ANID CATA-BASAL project FB210003 (CR, RJA, FEB); ANID FONDECYT Regular grant #1230345 (CR), #1231718 (RJA), and #1200495 (FEB); NASA ADAP award 80NSSC19K0749 (MJK); ANID Millennium Science Initiative Program - ICN12_009 (FEB); ANID FONDECYT Postdoctorado grant #3220516 (MJT), #3210157 (AFR), and #3230310 (YD); the European Research Council (ERC) under the European Union's Horizon 2020 research and innovation program, grant agreement #950533 (BT); the Israel Science Foundation, grant #1849/19 (BT); the Korea Astronomy and Space Science Institute under the R&D program supervised by the Ministry of Science and ICT, Project #2024-1-831-01 (KO); the National Research Foundation of Korea, NRF-2020R1C1C1005462 (KO).

References

Alloin, D., Pelat, D., Phillips, M., & Whittle, M. 1985, ApJ, 288, 205
Ananna, T. T., Urry, C. M., Treister, E., et al. 2020, ApJ, 903, 85
Antonucci, R. 1993, ARA&A, 31, 473
Arnaud, K. A. 1996, ASP Conf. Ser., 101, 17
Assef, R. J., Kochanek, C. S., Brodwin, M., et al. 2010, ApJ, 713, 970
Astropy Collaboration (Price-Whelan, A. M., et al.) 2022, ApJ, 935, 167
Avni, Y., & Tananbaum, H. 1982, ApJ, 262, L17
Avni, Y., & Tananbaum, H. 1986, ApJ, 305, 83
Baek, J., Chung, A., Schawinski, K., et al. 2019, MNRAS, 488, 4317
Barthelmy, S. D., Barbier, L. M., Cummings, J. R., et al. 2005, Space Sci. Rev., 120, 143
Baumgartner, W. H., Tueller, J., Markwardt, C. B., et al. 2013, ApJS, 207, 19
Bechtold, J., Siemiginowska, A., Shields, J., et al. 2003, ApJ, 588, 119
Beloborodov, A. M. 1999, ASP Conf. Ser., 161, 295
Bianchi, S., Maiolino, R., & Risaliti, G. 2012, Adv. Astron., 2012, 782030
Bonning, E. W., Cheng, L., Shields, G. A., Salviander, S., & Gebhardt, K. 2007, ApJ, 659, 211
Bonning, E. W., Shields, G. A., Stevens, A. C., & Salviander, S. 2013, ApJ, 770, 30
Boquien, M., Burgarella, D., Roehlly, Y., et al. 2019, A&A, 622, A103
Bradley, L., Sipőcz, B., Robitaille, T., et al. 2021, `https://doi.org/10.5281/zenodo.4624996`
Breeveld, A. A., Curran, P. A., Hoversten, E. A., et al. 2010, MNRAS, 406, 1687
Brightman, M., Baloković, M., Ballantyne, D. R., et al. 2017, ApJ, 844, 10
Burrows, D. N., Hill, J. E., Nousek, J. A., et al. 2005, Space Sci. Rev., 120, 165
Cackett, E. M., Horne, K., & Winkler, H. 2007, MNRAS, 380, 669
Cackett, E. M., Chiang, C.-Y., McHardy, I., et al. 2018, ApJ, 857, 53
Cackett, E. M., Bentz, M. C., & Kara, E. 2021, iScience, 24, 102557
Cackett, E. M., Zoghbi, A., & Ulrich, O. 2022, ApJ, 925, 29
Calistro Rivera, G., Lusso, E., Hennawi, J. F., & Hogg, D. W. 2016, ApJ, 833, 98
Calzetti, D., Armus, L., Bohlin, R. C., et al. 2000, ApJ, 533, 682
Cardelli, J. A., Clayton, G. C., & Mathis, J. S. 1989, ApJ, 345, 245
Cash, W. 1979, ApJ, 228, 939
Chelouche, D. 2013, ApJ, 772, 9
Chelouche, D., Pozo Nuñez, F., & Kaspi, S. 2019, Nat. Astron., 3, 251
Collier, S., & Peterson, B. M. 2001, ApJ, 555, 775
Collier, S. J., Horne, K., Kaspi, S., et al. 1998, ApJ, 500, 162
den Brok, J. S., Koss, M. J., Trakhtenbrot, B., et al. 2022, ApJS, 261, 7
Done, C., Davis, S. W., Jin, C., Blaes, O., & Ward, M. 2012, MNRAS, 420, 1848
Duras, F., Bongiorno, A., Ricci, F., et al. 2020, A&A, 636, A73
Elvis, M., Wilkes, B. J., McDowell, J. C., et al. 1994, ApJS, 95, 1
Feigelson, E. D., & Nelson, P. I. 1985, ApJ, 293, 192
Freeman, K. C. 2008, in Formation and Evolution of Galaxy Bulges, eds. M. Bureau, E. Athanassoula, & B. Barbuy, 245, 3
Green, P. J., Aldcroft, T. L., Richards, G. T., et al. 2009, ApJ, 690, 644
Grupe, D., Komossa, S., Leighly, K. M., & Page, K. L. 2010, ApJS, 187, 64
Gupta, K. K., Ricci, C., Tortosa, A., et al. 2021, MNRAS, 504, 428
Haardt, F., & Maraschi, L. 1991, ApJ, 380, L51
HI4PI Collaboration (Ben Bekhti, N., et al.) 2016, A&A, 594, A116
Ho, L. C. 2008, ARA&A, 46, 475
Hopkins, P. F., Richards, G. T., & Hernquist, L. 2007, ApJ, 654, 731
Hubeny, I., Agol, E., Blaes, O., & Krolik, J. H. 2000, ApJ, 533, 710
Ichikawa, K., Ricci, C., Ueda, Y., et al. 2019, ApJ, 870, 31
Isobe, T., Feigelson, E. D., Akritas, M. G., & Babu, G. J. 1990, ApJ, 364, 104
Jin, C., Ward, M., & Done, C. 2012, MNRAS, 425, 907
Jin, C., Lusso, E., Ward, M., Done, C., & Middei, R. 2024, MNRAS, 527, 356
Just, D. W., Brandt, W. N., Shemmer, O., et al. 2007, ApJ, 665, 1004
Kawamuro, T., Ricci, C., Imanishi, M., et al. 2022, ApJ, 938, 87
Kelly, B. C. 2007, ApJ, 665, 1489
Kinney, A. L., Bohlin, R. C., Calzetti, D., Panagia, N., & Wyse, R. F. G. 1993, ApJS, 86, 5
Koratkar, A., & Blaes, O. 1999, PASP, 111, 1
Kormendy, J., & Richstone, D. 1995, ARA&A, 33, 581
Koss, M., Mushotzky, R., Veilleux, S., et al. 2011, ApJ, 739, 57
Koss, M., Trakhtenbrot, B., Ricci, C., et al. 2017, ApJ, 850, 74
Koss, M. J., Trakhtenbrot, B., Ricci, C., et al. 2022a, ApJS, 261, 1
Koss, M. J., Ricci, C., Trakhtenbrot, B., et al. 2022b, ApJS, 261, 2
Koss, M. J., Trakhtenbrot, B., Ricci, C., et al. 2022c, ApJS, 261, 6
Krawczyk, C. M., Richards, G. T., Mehta, S. S., et al. 2013, ApJS, 206, 4
Krimm, H. A., Holland, S. T., Corbet, R. H. D., et al. 2013, ApJS, 209, 14
Kuraszkiewicz, J. K., Wilkes, B. J., Hooper, E. J., et al. 2003, ApJ, 590, 128
Lamperti, I., Koss, M., Trakhtenbrot, B., et al. 2017, MNRAS, 467, 540
Lawrence, A. 2012, MNRAS, 423, 451
Lusso, E., & Risaliti, G. 2016, ApJ, 819, 154
Lusso, E., & Risaliti, G. 2017, A&A, 602, A79
Lusso, E., Comastri, A., Vignali, C., et al. 2010, A&A, 512, A34
Lusso, E., Comastri, A., Simmons, B. D., et al. 2012, MNRAS, 425, 623
Lusso, E., Risaliti, G., Nardini, E., et al. 2020, A&A, 642, A150
Magdziarz, P., & Zdziarski, A. A. 1995, MNRAS, 273, 837
Makishima, K., Maejima, Y., Mitsuda, K., et al. 1986, ApJ, 308, 635
Malkan, M. A. 1983, ApJ, 268, 582
Malkan, M. A., & Sargent, W. L. W. 1982, ApJ, 254, 22
Marchese, E., Della Ceca, R., Caccianiga, A., et al. 2012, A&A, 539, A48
Marconi, A., Risaliti, G., Gilli, R., et al. 2004, IAU Symp., 222, 49
Markowitz, A. G., Krumpe, M., & Nikutta, R. 2014, MNRAS, 439, 1403
Marshall, A., Auger-Williams, M. W., Banerji, M., Maiolino, R., & Bowler, R. 2022, MNRAS, 515, 5617
Martínez-Ramírez, L. N., Rivera, G. C., Lusso, E., et al. 2024, A&A, 688, A46
Massaro, E., Giommi, P., Leto, C., et al. 2009, A&A, 495, 691
McKaig, J., Ricci, C., Paltani, S., et al. 2023, MNRAS, 526, 5072
Mejía-Restrepo, J. E., Trakhtenbrot, B., Koss, M. J., et al. 2022, ApJS, 261, 5
Miller, J. A., Cackett, E. M., Goad, M. R., et al. 2023, ApJ, 953, 137
Mitchell, J. A. J., Done, C., Ward, M. J., et al. 2023, MNRAS, 524, 1796

Mitsuda, K., Inoue, H., Koyama, K., et al. 1984, PASJ, 36, 741
Narayan, R. 2005, Ap&SS, 300, 177
Netzer, H. 2013, The Physics and Evolution of Active Galactic Nuclei (Cambridge, UK: Cambridge University Press)
Noll, S., Burgarella, D., Giovannoli, E., et al. 2009, A&A, 507, 1793
Novikov, I. D., & Thorne, K. S. 1973, Black Holes (Les Astres Occlus), 343
Oh, K., Koss, M. J., Ueda, Y., et al. 2022, ApJS, 261, 4
Padovani, P., Alexander, D. M., Assef, R. J., et al. 2017, A&ARv, 25, 2
Paliya, V. S., Koss, M., Trakhtenbrot, B., et al. 2019, ApJ, 881, 154
Pei, Y. C. 1992, ApJ, 395, 130
Peng, C. Y., Ho, L. C., Impey, C. D., & Rix, H.-W. 2002, AJ, 124, 266
Peng, C. Y., Ho, L. C., Impey, C. D., & Rix, H.-W. 2010, AJ, 139, 2097
Poole, T. S., Breeveld, A. A., Page, M. J., et al. 2008, MNRAS, 383, 627
Ramos Almeida, C., & Ricci, C. 2017, Nat. Astron., 1, 679
Rankine, A. L., Aird, J., Ruiz, A., & Georgakakis, A. 2024, MNRAS, 527, 9004
Reeves, J., Done, C., Pounds, K., et al. 2008, MNRAS, 385, L108
Ricci, C., & Trakhtenbrot, B. 2023, Nat. Astron., 7, 1282
Ricci, C., Ueda, Y., Koss, M. J., et al. 2015, ApJ, 815, L13
Ricci, C., Trakhtenbrot, B., Koss, M. J., et al. 2017, ApJS, 233, 17
Ricci, C., Ho, L. C., Fabian, A. C., et al. 2018, MNRAS, 480, 1819
Ricci, F., Treister, E., Bauer, F. E., et al. 2022, ApJS, 261, 8
Ricci, C., Chang, C.-S., Kawamuro, T., et al. 2023, ApJ, 952, L28
Richards, G. T., Lacy, M., Storrie-Lombardi, L. J., et al. 2006, ApJS, 166, 470
Risaliti, G., & Elvis, M. 2004, Astrophys. Space Sci. Lib., 308, 187
Risaliti, G., & Lusso, E. 2015, ApJ, 815, 33
Risaliti, G., Elvis, M., & Nicastro, F. 2002, ApJ, 571, 234
Rosario, D. J., Burtscher, L., Davies, R. I., et al. 2018, MNRAS, 473, 5658
Runnoe, J. C., Brotherton, M. S., & Shang, Z. 2012a, MNRAS, 422, 478
Runnoe, J. C., Brotherton, M. S., & Shang, Z. 2012b, MNRAS, 426, 2677
Saccheo, I., Bongiorno, A., Piconcelli, E., et al. 2023, A&A, 671, A34
Schlegel, D. J., Finkbeiner, D. P., & Davis, M. 1998, ApJ, 500, 525
Schmidt, M. 1968, ApJ, 151, 393
Sergeev, S. G., Doroshenko, V. T., Golubinskiy, Y. V., Merkulova, N. I., & Sergeeva, E. A. 2005, ApJ, 622, 129
Setoguchi, K., Ueda, Y., Toba, Y., et al. 2023, ApJ, submitted [arXiv:2312.03552]
Shakura, N. I., & Sunyaev, R. A. 1973, A&A, 500, 33
Shang, Z., Brotherton, M. S., Wills, B. J., et al. 2011, ApJS, 196, 2
Shen, X., Hopkins, P. F., Faucher-Giguère, C.-A., et al. 2020, MNRAS, 495, 3252
Shields, G. A. 1978, Nature, 272, 706
Shimizu, T. T., Mushotzky, R. F., Meléndez, M., et al. 2017, MNRAS, 466, 3161
Signorini, M., Risaliti, G., Lusso, E., et al. 2023, A&A, 676, A143
Slone, O., & Netzer, H. 2012, MNRAS, 426, 656
Stalin, C. S., Petitjean, P., Srianand, R., et al. 2010, MNRAS, 401, 294
Steffen, A. T., Strateva, I., Brandt, W. N., et al. 2006, AJ, 131, 2826
Strateva, I. V., Brandt, W. N., Schneider, D. P., Vanden Berk, D. G., & Vignali, C. 2005, AJ, 130, 387
Svoboda, J., Beuchert, T., Guainazzi, M., et al. 2015, A&A, 578, A96
Tananbaum, H., Avni, Y., Branduardi, G., et al. 1979, ApJ, 234, L9
Tang, S. M., Zhang, S. N., & Hopkins, P. F. 2007, MNRAS, 377, 1113
Temple, M. J., Hewett, P. C., & Banerji, M. 2021, MNRAS, 508, 737
Temple, M. J., Matthews, J. H., Hewett, P. C., et al. 2023, MNRAS, 523, 646
Thorne, K. S. 1974, ApJ, 191, 507
Timlin, J. D., Brandt, W. N., Ni, Q., et al. 2020, MNRAS, 492, 719
Timlin, J. D., III, Brandt, W. N., & Laor, A. 2021, MNRAS, 504, 5556
Ueda, Y., Akiyama, M., Ohta, K., & Miyaji, T. 2003, ApJ, 598, 886
Ulrich, M.-H., Maraschi, L., & Urry, C. M. 1997, ARA&A, 35, 445
Urry, C. M., & Padovani, P. 1995, PASP, 107, 803
Vasudevan, R. V., & Fabian, A. C. 2009, MNRAS, 392, 1124
Vasudevan, R. V., Mushotzky, R. F., Winter, L. M., & Fabian, A. C. 2009, MNRAS, 399, 1553
Vasudevan, R. V., Fabian, A. C., Gandhi, P., Winter, L. M., & Mushotzky, R. F. 2010, MNRAS, 402, 1081
Virtanen, P., Gommers, R., Oliphant, T. E., et al. 2020, Nat. Methods, 17, 261
Ward, M., Elvis, M., Fabbiano, G., et al. 1987, ApJ, 315, 74
Wilkes, B. J., Tananbaum, H., Worrall, D. M., et al. 1994, ApJS, 92, 53
Yang, G., Boquien, M., Buat, V., et al. 2020, MNRAS, 491, 740
Yang, G., Boquien, M., Brandt, W. N., et al. 2022, ApJ, 927, 192
Young, M., Elvis, M., & Risaliti, G. 2010, ApJ, 708, 1388
Yuan, F., & Narayan, R. 2014, ARA&A, 52, 529
Yuan, W., Siebert, J., & Brinkmann, W. 1998, A&A, 334, 498
Zdziarski, A. A., Johnson, W. N., & Magdziarz, P. 1996, MNRAS, 283, 193
Życki, P. T., Done, C., & Smith, D. A. 1999, MNRAS, 309, 561

Appendix A: Additional material

Table A.1. Sources in our sample with simultaneous optical/UV and X-ray observations.

BAT ID	Swift ID	Counterpart Name	R.A.	Dec.	Redshift	Distance	$\log(N_H/cm^{-2})$
2	SWIFTJ0001.6-7701	2MASXJ00014596-7657144	0.4420	−76.9540	0.0584	261.7	≤ 20.00
3	SWIFTJ0002.5+0323	NGC7811	0.6103	3.3519	0.0255	111.2	≤ 20.00
6	SWIFTJ0006.2+2012	Mrk335	1.5814	20.2030	0.0258	113.2	20.48
10	SWIFTJ0021.2-1909	LEDA1348	5.2814	−19.1682	0.0956	439.9	21.98
14	SWIFTJ0026.5-5308	LEDA433346	6.6695	−53.1633	0.0629	283.7	≤ 20.00
16	SWIFTJ0029.2+1319	PG0026+129	7.3071	13.2678	0.1420	671.7	≤ 20.00
19	SWIFTJ0034.5-7904	RHS3	8.5697	−79.0890	0.0740	335.9	≤ 20.00
34	SWIFTJ0051.6+2928	UGC524	12.8959	29.4013	0.0360	157.9	≤ 20.00
36	SWIFTJ0051.9+1724	Mrk1148	12.9782	17.4329	0.0640	287.5	20.30
39	SWIFTJ0054.9+2524	PG0052+251	13.7172	25.4275	0.1550	739.5	≤ 20.00

Notes. We have listed the BAT and Swift IDs, counterpart names, coordinates (in degrees, J2000), redshifts, luminosity distances in Mpc (Koss et al. 2022b), and X-ray column density values from R17 for all the sources. The table in its entirety is available at the CDS.

Table A.2. Observation IDs of the observations used for each source.

BAT ID	Swift ID	Obs. ID	UVOT Exposure (s)	XRT Exposure (s)	UVOT Filters
2	SWIFTJ0001.6-7701	00080854001	4419	4485	Only UV
3	SWIFTJ0002.5+0323	00047107014	1600	1625	All
6	SWIFTJ0006.2+2012	00090006004	7917	8136	All
10	SWIFTJ0021.2-1909	00040691001	6485	6493	U, UVW1
14	SWIFTJ0026.5-5308	00041141001	2669	2670	UVW1, UVM2
16	SWIFTJ0029.2+1319	00080859001	5976	6000	All
19	SWIFTJ0034.5-7904	00080861001	4782	4806	All
34	SWIFTJ0051.6+2928	00080867001	6222	6297	All
36	SWIFTJ0051.9+1724	00080868001	6696	6800	All
39	SWIFTJ0054.9+2524	00080869001	6117	6146	All

Notes. For each observation, the total exposure times with *Swift*/UVOT and *Swift*/XRT, and the available *Swift*/UVOT filters are also reported. The table in its entirety is available at the CDS.

Table A.3. Source fluxes as calculated by the *Swift*/UVOT command `uvotsource` via 5" aperture photometry.

BAT ID	Swift ID	F_U	F_V	F_B	F_{W1}	F_{W2}	F_{M2}
2	SWIFTJ0001.6-7701	–	–	–	2.40 ± 0.21	3.30 ± 0.2	2.49 ± 0.15
3	SWIFTJ0002.5+0323	3.18 ± 0.12	3.66 ± 0.15	3.29 ± 0.11	4.03 ± 0.13	4.73 ± 0.14	4.11 ± 0.12
6	SWIFTJ0006.2+2012	16.16 ± 0.36	7.43 ± 0.17	9.86 ± 0.19	22.65 ± 0.45	28.35 ± 0.56	23.56 ± 0.51
10	SWIFTJ0021.2-1909	0.19 ± 0.02	–	–	0.06 ± 0.01	–	–
14	SWIFTJ0026.5-5308	–	–	–	1.33 ± 0.17	–	1.06 ± 0.07
16	SWIFTJ0029.2+1319	4.93 ± 0.11	2.56 ± 0.10	3.26 ± 0.09	5.97 ± 0.16	8.16 ± 0.20	5.93 ± 0.18
19	SWIFTJ0034.5-7904	9.65 ± 0.25	4.64 ± 0.15	5.79 ± 0.15	12.81 ± 0.25	17.38 ± 0.38	13.74 ± 0.35
34	SWIFTJ0051.6+2928	1.74 ± 0.07	3.41 ± 0.12	2.75 ± 0.08	1.64 ± 0.07	1.61 ± 0.04	1.36 ± 0.07
36	SWIFTJ0051.9+1724	6.08 ± 0.13	2.46 ± 0.11	3.24 ± 0.11	7.83 ± 0.22	10.08 ± 0.21	7.39 ± 0.23
39	SWIFTJ0054.9+2524	5.25 ± 0.15	2.12 ± 0.09	3.05 ± 0.09	6.53 ± 0.18	10.49 ± 0.25	6.63 ± 0.14

Notes. These flux values include potential contribution from the host galaxy to the AGN (within 5" region; see Sect. 3.1). Flux units: 10^{-15} erg cm^{-2} s^{-1} Å^{-1}. The table in its entirety is available at the CDS.

Table A.4. Source magnitudes as calculated by the *Swift*/UVOT command `uvotsource` via 5" aperture photometry.

BAT ID	Swift ID	M_V	M_B	M_U	M_{W1}	M_{M2}	M_{W2}
2	SWIFTJ0001.6-7701	–	–	–	17.16 ± 0.03	17.37 ± 0.03	17.30 ± 0.03
3	SWIFTJ0002.5+0323	15.01 ± 0.05	15.61 ± 0.04	16.16 ± 0.04	16.60 ± 0.03	16.83 ± 0.03	16.91 ± 0.03
6	SWIFTJ0006.2+2012	14.24 ± 0.02	14.42 ± 0.02	14.39 ± 0.02	14.72 ± 0.02	14.93 ± 0.02	14.96 ± 0.02
10	SWIFTJ0021.2-1909	–	–	19.21 ± 0.06	21.20 ± 0.08	–	–
14	SWIFTJ0026.5-5308	–	–	–	17.80 ± 0.08	18.30 ± 0.03	–
16	SWIFTJ0029.2+1319	15.40 ± 0.04	15.62 ± 0.03	15.68 ± 0.02	16.17 ± 0.03	16.43 ± 0.03	16.32 ± 0.03
19	SWIFTJ0034.5-7904	14.76 ± 0.04	15.00 ± 0.03	14.95 ± 0.03	15.34 ± 0.02	15.52 ± 0.03	15.50 ± 0.02
34	SWIFTJ0051.6+2928	15.09 ± 0.04	15.81 ± 0.03	16.81 ± 0.04	17.57 ± 0.05	18.03 ± 0.05	18.08 ± 0.02
36	SWIFTJ0051.9+1724	15.44 ± 0.05	15.63 ± 0.04	15.45 ± 0.02	15.88 ± 0.03	16.19 ± 0.03	16.09 ± 0.02
39	SWIFTJ0054.9+2524	15.61 ± 0.05	15.69 ± 0.03	15.61 ± 0.03	16.07 ± 0.03	16.31 ± 0.02	16.04 ± 0.03

Notes. These magnitude values include potential contribution from the host galaxy to the AGN (within 5" region; see Sect. 3.1). The table in its entirety is available at the CDS.

Table A.5. Results of the X-ray spectral fitting (Sect. 4).

BAT ID	Swift ID	Γ	F_{2-10}	Model	Statistic/dof
2	SWIFTJ0001.6-7701	$1.55^{+1.01}_{-0.64}$	$2.90^{+0.48}_{-0.44}$	A1 + `ZXIPCF`	86.84/113
3	SWIFTJ0002.5+0323	$1.97^{+0.24}_{-0.16}$	$3.19^{+0.37}_{-0.34}$	A2	134.4/148
6	SWIFTJ0006.2+2012	$2.34^{+0.03}_{-0.04}$	$10.8^{+0.21}_{-0.21}$	A1	796.5/597
10	SWIFTJ0021.2-1909	$1.60^{+0.18}_{-0.18}$	$9.03^{+0.50}_{-0.48}$	B1	360.5/445
14	SWIFTJ0026.5-5308	$1.70^{+0.35}_{-0.23}$	$1.97^{+0.25}_{-0.23}$	A1	130.7/139
16	SWIFTJ0029.2+1319	$2.20^{+0.17}_{-0.17}$	$5.44^{+0.22}_{-0.21}$	A2	335.2/397
19	SWIFTJ0034.5-7904	$2.36^{+0.11}_{-0.07}$	$6.14^{+0.22}_{-0.21}$	A2	390.3/390
34	SWIFTJ0051.6+2928	$1.99^{+0.25}_{-0.23}$	$1.71^{+0.13}_{-0.13}$	A2	197.3/253
36	SWIFTJ0051.9+1724	$1.91^{+0.10}_{-0.03}$	$16.6^{+0.40}_{-0.40}$	A2	564.5/578
39	SWIFTJ0054.9+2524	$1.97^{+0.18}_{-0.15}$	$5.58^{+0.24}_{-0.23}$	A2	328.9/403

Notes. We have reported the main outputs of the fitting here, including the best-fit values of the photon index, the 2–10 keV intrinsic fluxes with errors, the model used to get the best fit, and the value of the statistic and the degrees of freedom of the fit. Flux units: 10^{-12} erg cm^{-2} s^{-1}. The table in its entirety is available at the CDS.

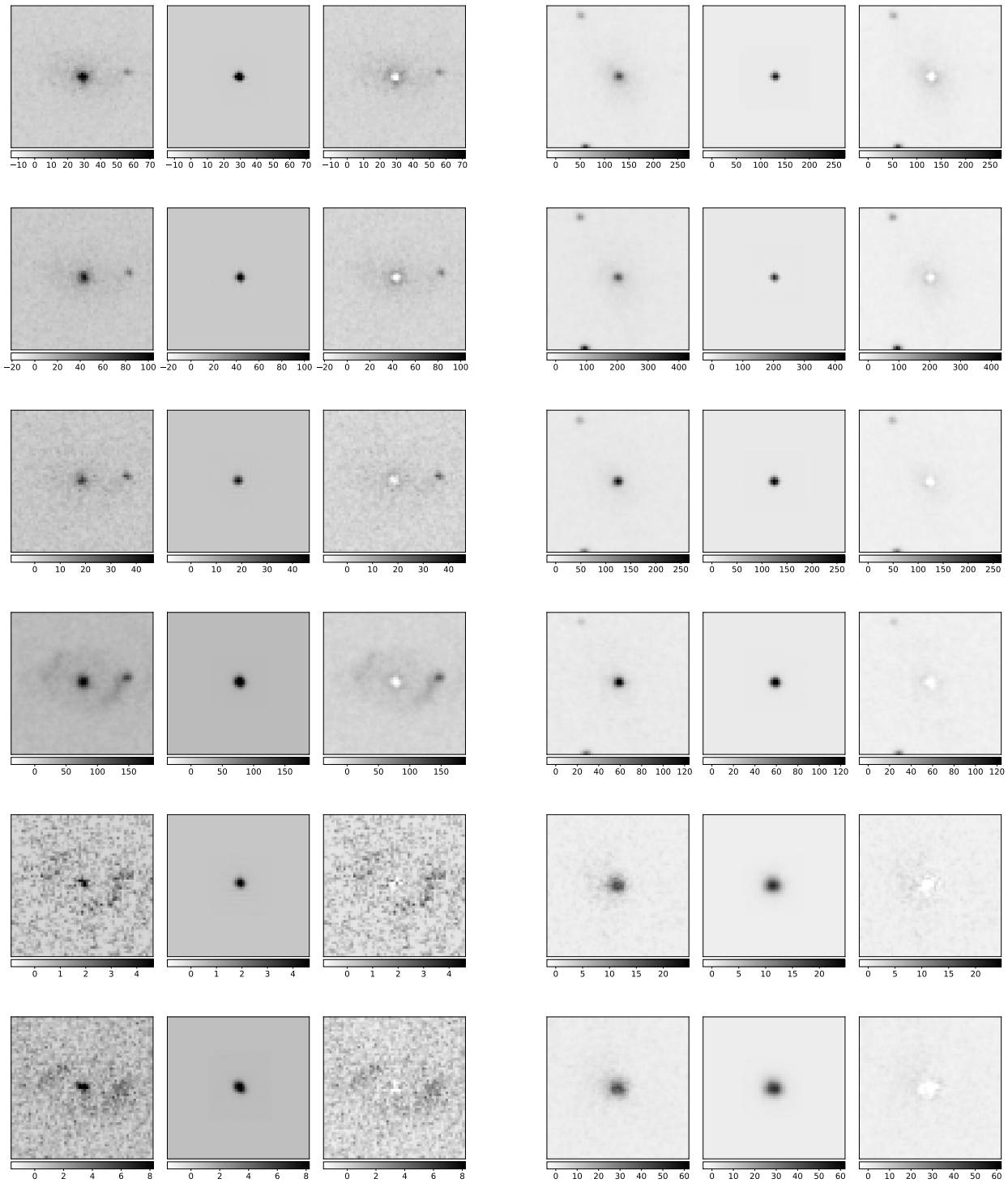

(a) (b)

Fig. A.1. Examples of source image fitting with GALFIT using a sky + PSF + Sérsic profile (Sect. 5): (a) SWIFTJ2226.8+3628 and (b) SWIFTJ0640.4-2554. In each panel, the left image is the source image, the middle one is the model, and the right one is the fit-residual. We show the fit in all six *Swift*/UVOT filters from top to bottom in order (V, B, U, UVW1, UVM2, and UVW2). The colorbars represent the counts per pixel.

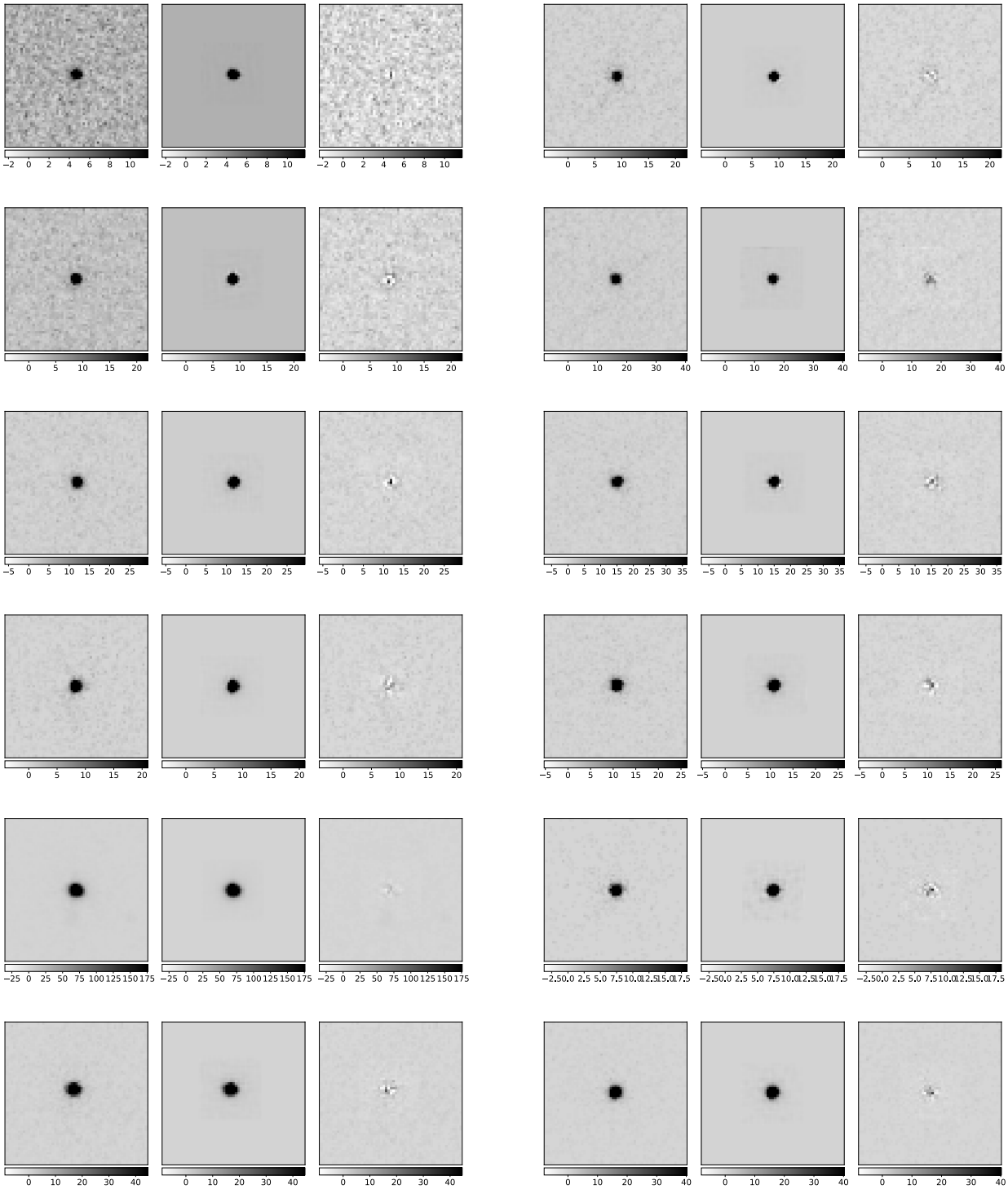

(a) (b)

Fig. A.2. Examples of source image fitting with GALFIT using a sky + PSF profile for high redshift sources: (a) SWIFTJ1723.2+3418 and (b) SWIFTJ1421.4+4747. We corrected the GALFIT-estimated fluxes for such sources (Sect. 5.3) as GALFIT was unable to fit a Sérsic profile to these sources and hence, missed some AGN flux. In each panel, the left image is the source, the middle one is the model, and the right one is the fit-residual. We show the fit in all six *Swift*/UVOT filters from top to bottom in order (V, B, U, UVW1, UVM2, and UVW2). The colorbars represent the counts per pixel.

Table A.6. Corrected AGN fluxes as estimated by GALFIT image decomposition (Sect. 5).

BAT ID	Swift ID	F_V	F_B	F_U	F_{W1}	F_{M2}	F_{W2}	Flag
3	SWIFTJ0002.5+0323	0.75 ± 0.07	0.82 ± 0.06	1.59 ± 0.10	1.59 ± 0.14	2.17 ± 0.11	2.24 ± 0.15	-
6	SWIFTJ0006.2+2012	5.82 ± 0.13^o	6.70 ± 0.15^o	10.89 ± 0.46	19.63 ± 1.14^o	22.33 ± 0.76^o	24.60 ± 1.19^o	-
16	SWIFTJ0029.2+1319	3.17 ± 0.15^o	3.07 ± 0.08^o	3.77 ± 0.16^o	4.90 ± 0.35^o	6.50 ± 0.25^o	5.96 ± 0.52^o	c
19	SWIFTJ0034.5-7904	0.89 ± 0.07	1.09 ± 0.05	2.53 ± 0.21	10.28 ± 0.75^o	13.99 ± 0.60^o	12.30 ± 1.09^o	c
34	SWIFTJ0051.6+2928	1.17 ± 0.06	1.11 ± 0.05	1.16 ± 0.07	1.14 ± 0.10	1.00 ± 0.06	1.23 ± 0.07^o	-
36	SWIFTJ0051.9+1724	3.45 ± 0.24^o	3.01 ± 0.07^o	4.55 ± 0.20^o	6.91 ± 0.44^o	7.60 ± 0.31^o	6.26 ± 0.58^o	c
39	SWIFTJ0054.9+2524	1.68 ± 0.05	2.80 ± 0.06^o	4.76 ± 0.21^o	5.40 ± 0.38^o	7.24 ± 0.38^o	7.60 ± 0.66^o	c
43	SWIFTJ0059.4+3150	1.17 ± 0.07	0.46 ± 0.90	0.97 ± 0.14^o	4.00 ± 0.30^p	3.64 ± 0.16^o	3.55 ± 0.17	-
45	SWIFTJ0101.5-0308	0.40 ± 0.04	0.14 ± 0.04	0.36 ± 0.04^o	0.29 ± 0.05^o	0.27 ± 0.03^o	0.32 ± 0.04^o	-
51	SWIFTJ0105.7-1414	1.93 ± 0.14	2.50 ± 0.21	3.57 ± 0.12	6.08 ± 0.43	11.56 ± 2.29	8.87 ± 0.54	c

Notes. The last column shows, in the form of flags (c), if the GALFIT-estimated fluxes were corrected using corrections calculated in Sect. 5.3 to create the final SEDs. All fluxes are in units of 10^{-15} erg cm^{-2} s^{-1} Å^{-1}. The table in its entirety is available at the CDS. $^{(o)}$A sky + PSF model was used to get the best GALFIT residual as GALFIT was unable to fit a Sérsic profile and hence, the corresponding correction was employed (see Fig. 5), if and when needed. $^{(p)}$UVOT pipeline-estimated flux was used in the final SED.

Table A.7. Corrected AGN magnitudes as estimated by GALFIT image decomposition (Sect. 5).

BAT ID	Swift ID	M_V	M_B	M_U	M_{W1}	M_{M2}	M_{W2}	Flag
3	SWIFTJ0002.5+0323	16.74 ± 0.09	17.12 ± 0.05	16.91 ± 0.03	17.61 ± 0.03	17.52 ± 0.02	17.72 ± 0.02	-
6	SWIFTJ0006.2+2012	14.51 ± 0.01^o	14.84 ± 0.00^o	14.82 ± 0.01	14.88 ± 0.00^o	14.99 ± 0.00^o	15.12 ± 0.00^o	-
16	SWIFTJ0029.2+1319	15.17 ± 0.04^o	15.69 ± 0.004^o	15.97 ± 0.01^o	16.39 ± 0.01^o	16.33 ± 0.005^o	16.66 ± 0.04^o	c
19	SWIFTJ0034.5-7904	16.54 ± 0.08	16.81 ± 0.03	16.40 ± 0.05	15.58 ± 0.02^o	15.50 ± 0.01^o	15.87 ± 0.04^o	c
34	SWIFTJ0051.6+2928	16.25 ± 0.04	16.79 ± 0.03	17.25 ± 0.03	17.97 ± 0.03	18.36 ± 0.03	18.37 ± 0.01^o	-
36	SWIFTJ0051.9+1724	15.08 ± 0.06^o	15.71 ± 0.002^o	15.77 ± 0.01^o	16.01 ± 0.01^o	16.16 ± 0.01^o	16.60 ± 0.05^o	c
39	SWIFTJ0054.9+2524	15.86 ± 0.02	15.79 ± 0.0003^o	15.72 ± 0.01^o	16.28 ± 0.01^o	16.21 ± 0.004^o	16.39 ± 0.04^o	c
43	SWIFTJ0059.4+3150	16.25 ± 0.05	17.75 ± 0.18	17.45 ± 0.12^o	16.61 ± 0.02^p	16.96 ± 0.01^o	17.22 ± 0.00	-
45	SWIFTJ0101.5-0308	17.43 ± 0.11	19.01 ± 0.31	18.51 ± 0.09^o	19.44 ± 0.12^o	19.78 ± 0.09^o	19.82 ± 0.09^o	-
51	SWIFTJ0105.7-1414	15.71 ± 0.07	15.91 ± 0.07	16.03 ± 0.00	16.15 ± 0.01	15.70 ± 0.18	16.23 ± 0.01	c

Notes. The last column shows in the form of flags (c) if the GALFIT-estimated magnitudes were corrected using corrections calculated in Sect. 5.3 to create the final SEDs. We report an uncertainty of 0.00 when it is very low ($\lesssim 10^{-6}$ mag). The table in its entirety is available at the CDS. $^{(o)}$A sky + PSF model was used to get the best GALFIT residual as GALFIT was unable to fit a Sérsic profile and hence, the corresponding correction was employed (see Fig. 5), if and when needed. $^{(p)}$UVOT pipeline-estimated magnitude was used in the final SED.

Table A.8. Results of the optical/UV SED fitting (Sect. 6).

BAT ID	Swift ID	$kT_{\rm max}$	$E(B-V)_{\rm HG}$	$F_{\rm uvo}$	Flag
3	SWIFTJ0002.5+0323	$2.8^{+2.3}_{-0.8}$	$0.058^{+0.070}_{-0.058}$	$1.85^{+0.97}_{-0.65}$	-
6	SWIFTJ0006.2+2012	$3.9^{+1.5}_{-0.3}$	< 0.014	$17.6^{+5.05}_{-10.6}$	-
16	SWIFTJ0029.2+1319	$6.1^{+12.1}_{-2.5}$	$0.117^{+0.037}_{-0.050}$	$24.0^{+5.24}_{-3.37}$	-
19	SWIFTJ0034.5-7904	2.7	< 0.001	$3.05^{+0.13}_{-0.15}$	t
34	SWIFTJ0051.6+2928	$3.7^{+4.3}_{-1.3}$	$0.298^{+0.065}_{-0.061}$	$8.28^{+2.06}_{-1.55}$	-
36	SWIFTJ0051.9+1724	$2.9^{+0.3}_{-0.2}$	< 0.012	$6.13^{+0.28}_{-0.47}$	-
39	SWIFTJ0054.9+2524	$6.4^{+2.7}_{-2.7}$	$0.058^{+0.018}_{-0.046}$	$15.7^{+3.81}_{-1.67}$	-
43	SWIFTJ0059.4+3150	$5.5^{+2.5}_{-1.2}$	< 0.007	$3.89^{+4.64}_{-0.92}$	-
45	SWIFTJ0101.5-0308	$2.8^{+1.2}_{-1.2}$	$0.268^{+0.154}_{-0.160}$	$1.45^{+1.82}_{-0.70}$	-
51	SWIFTJ0105.7-1414	$4.0^{+0.9}_{-0.6}$	0.000	$5.50^{+0.13}_{-0.13}$	e

Notes. We have listed the best-fit values of the disk temperature ($kT_{\rm max}$ in eV), the extinction due to the host galaxy $E(B-V)_{\rm HG}$, and the total, intrinsic optical/UV flux (from 10^{-7}–0.1 keV) with errors. The last column shows, in the form of flags, if the disk temperature was fixed to its median value of 2.7 eV (t) and if the host galaxy extinction was fixed to zero (e) during the fitting. Flux units: 10^{-11} erg cm^{-2} s^{-1}. The table in its entirety is available at the CDS.

Table A.9. Useful outputs from the broadband SED fitting.

BAT ID	Swift ID	$L_{2500\,\text{Å}}$	$L_{2\,\rm keV}$	$L_{\rm bol}$	$M_{\rm BH}$	$\alpha_{\rm ox}$	$\kappa_{4400\text{Å}}$	κ_{2-10}	$\lambda_{\rm Edd}$
3	SWIFTJ0002.5+0323	43.07	42.35	43.68	6.70	$-1.27^{+0.10}_{-0.14}$	$5.59^{+4.92}_{-3.35}$	$10.09^{+4.73}_{-3.60}$	−1.20
6	SWIFTJ0006.2+2012	43.99	43.11	44.57	7.23	$-1.34^{+0.14}_{-0.07}$	$5.86^{+2.94}_{-4.10}$	$22.26^{+10.38}_{-5.22}$	−0.84
16	SWIFTJ0029.2+1319	45.49	44.32	46.16	8.49	$-1.45^{+0.04}_{-0.06}$	$8.12^{+3.38}_{-2.19}$	$49.53^{+8.32}_{-11.80}$	−0.50
19	SWIFTJ0034.5-7904	44.26	43.78	44.95	8.02	$-1.19^{+0.02}_{-0.02}$	$6.56^{+0.54}_{-0.59}$	$10.70^{+0.81}_{-0.80}$	−1.25
34	SWIFTJ0051.6+2928	43.96	42.49	44.44	7.62	$-1.56^{+0.07}_{-0.09}$	$4.63^{+2.22}_{-1.68}$	$53.75^{+13.46}_{-16.65}$	−1.36
36	SWIFTJ0051.9+1724	44.43	43.91	45.15	7.75	$-1.20^{+0.02}_{-0.01}$	$7.38^{+0.59}_{-0.91}$	$8.66^{+0.61}_{-0.50}$	−0.77
39	SWIFTJ0054.9+2524	45.36	44.28	46.08	8.46	$-1.41^{+0.04}_{-0.07}$	$9.13^{+4.19}_{-1.86}$	$32.70^{+4.55}_{-8.44}$	−0.56
43	SWIFTJ0059.4+3150	42.69	41.96	43.42	7.56	$-1.28^{+0.06}_{-0.30}$	$8.96^{+18.44}_{-3.69}$	$14.26^{+2.90}_{-12.71}$	−2.32
45	SWIFTJ0101.5-0308	43.90	42.75	44.38	8.13	$-1.44^{+0.19}_{-0.39}$	$4.19^{+9.42}_{-3.79}$	$23.78^{+17.03}_{-32.21}$	−1.93
51	SWIFTJ0105.7-1414	44.30	43.48	45.03	7.88	$-1.32^{+0.01}_{-0.01}$	$8.37^{+0.48}_{-0.47}$	$16.79^{+1.26}_{-1.29}$	−1.03

Notes. We have reported the 2500 Å, 2 keV, and the bolometric luminosities with their errors. We also present the black hole masses ($M_{\rm BH}$) of our sources as estimated by Mejía-Restrepo et al. (2022) in units of $\log(M_{\rm BH}/{\rm M}_\odot)$. Finally, we list the estimated value of the optical-to-X-ray spectral indices ($\alpha_{\rm ox}$; Sect. 7.3), the 2–10 keV X-ray bolometric corrections (κ_{2-10}; Sect. 7.4.1), the 4400 Å optical bolometric corrections ($\kappa_{4400\text{Å}}$; Sect. 7.4.2), and the Eddington ratios ($\lambda_{\rm Edd}$ in log). Luminosity units: 10^{-42} erg s^{-1}. The table in its entirety is available at the CDS.

Table A.10. Estimated values of the optical and UV bolometric corrections (described in Sect. 7.4.2).

BAT ID	Swift ID	κ_V	κ_B	κ_U	κ_{W1}	κ_{M2}	κ_{W2}
3	SWIFTJ0002.5+0323	50.67	26.02	21.04	14.94	16.98	10.68
6	SWIFTJ0006.2+2012	54.23	27.10	21.09	14.00	15.22	8.98
16	SWIFTJ0029.2+1319	76.37	37.31	28.12	17.68	18.57	10.40
19	SWIFTJ0034.5-7904	59.30	30.56	24.84	17.82	20.36	12.93
34	SWIFTJ0051.6+2928	42.70	21.41	16.75	11.22	12.27	7.30
36	SWIFTJ0051.9+1724	67.06	34.31	27.61	19.44	21.96	13.70
39	SWIFTJ0054.9+2524	85.93	41.90	31.51	19.72	20.66	11.53
43	SWIFTJ0059.4+3150	83.93	41.17	31.22	19.83	20.95	11.85
45	SWIFTJ0101.5-0308	38.02	19.52	15.78	11.21	12.74	8.01
51	SWIFTJ0105.7-1414	77.48	38.66	30.01	19.85	21.52	12.65

Notes. The table in its entirety is available at the CDS.

Appendix B: GALFIT simulations

The AGN flux can be contaminated by the host galaxy's light. To extract reliable AGN flux measurements, we used GALFIT to fit the 2D surface brightness of our sources. However, considering the wide variety of sources in our sample, varying over redshift, morphology and total magnitude, we carried out some simulations to check the reliability of the flux values estimated by GALFIT. We simulated a population of fake type I AGN (similar to a procedure on optical images of Koss et al. 2011) covering the same redshift range as our original sample of type 1 AGN ($0.001 < z < 0.3$). We used ten Seyfert 2 galaxies, classified so by the optical classification provided by Koss et al. (2017), with X-ray column densities above 10^{23} cm^{-2} to eliminate the possibility of any significant optical/UV radiation coming from the SMBH at the center. We pre-processed, aspect corrected, and reduced the raw *Swift*/UVOT images of these ten sources in the three UV filters (UVW1, UVM2, UVW2), for start. The final sky images were then used to extract the total galaxy magnitudes of these sources to be used in GALFIT later. We then randomly selected a field star from our images and placed it at the center of the galaxy to replicate a type I AGN. The magnitude of the star was varied by changing its normalization to reciprocate different AGN light ratios (AGN magnitude to total magnitude calculated using 5" aperture photometry), ranging from 10% to 95%. We calculated the star's magnitude using GALFIT before placing it on the galaxy to get estimates of the star flux that would later be compared to the PSF flux estimated by GALFIT. We included different possible morphologies in this sample of ten galaxies: edge-on galaxies, face-on galaxies, and indeterminate. We did not go with the traditional galaxy morphology classification of elliptical and spiral galaxies because on scales as small as the ones in our UVOT images, GALFIT cannot really distinguish between bulge-dominated and disk-dominated morphologies. Also, we are not interested in fitting the extended features of the host galaxy, such as spiral arms, starburst regions and clumps. Instead, we included Seyfert 2s with different orientations to understand GALFIT's response to circular (face-on) versus elliptical (edge-on) galaxy shapes in 2D. In total, we simulated 270 type I AGN across the three *Swift*/UVOT UV filters with ten different AGN light ratios.

The GALFIT analysis of these 270 simulated AGN was done following the same procedure as the one followed for our original sample (described in Sect. 5):

1. A relatively empty region was selected from the image to fit the background using the sky component in GALFIT. In the case of crowded fields, a bad pixel mask was incorporated into the GALFIT parameter file to mask the background sources.
2. A region around the source with the same dimension as the one used in the previous step was selected and fit using the sky and PSF component in GALFIT. Like before, a bad pixel mask was used to mask the light from all the extra sources around our galaxy of interest. The sky estimated in the previous step was used as the input sky value in this step. However, we left the sky value to vary in general and fixed it only in cases when it was way off from the one estimated in the previous step. To fit the PSF component, GALFIT requires a PSF image that it, in turn, fits to the image. The PSF image was created using the `photutils` package in Python. This package uses a defined set of stars from the field of the source and reiterates over these star profiles to produce a PSF image. We used three to six bright background stars to create a PSF image for each of our ten sources in each UV filter. The input value used for the PSF magnitude was the one calculated by GALFIT previously for the star in the absence of any host galaxy. All the residuals were visually examined to check for incredibly useless fits.
3. Finally, the same source region as before was fit using the sky, PSF, and Sérsic profile component in GALFIT. The sky and PSF input parameters used were the ones we obtained from the previous step. The input Sérsic magnitude was defined as the galaxy magnitude obtained from the UVOT pipeline. The input value for effective Sérsic radius was visually determined from the source images. The input values for the coordinates of the Sérsic profile were put as the ones for the PSF profile from the results of the previous step. We started with an input Sérsic index value of 2.5 and moved to 2.0, 1.5, 1.0, 0.5, 3.0, 3.5, and 4.0 in cases when GALFIT was not able to converge. All the other parameters of the Sérsic profile were left to their default values. In multiple cases, when GALFIT was unable to converge with these input parameters, we fixed the controversial parameters (generally, axis ratio or effective radius, sometimes the coordinates of the Sérsic profile) to specific acceptable values so as to get GALFIT to converge and produce reliable fits, estimates, and residuals. All the residuals were visually inspected to confirm the reliability of the fits. In some cases, even after multiple repetitions, when GALFIT was not able to fit all the three components to the source, we quote results from step 2; that is, just the sky + PSF fits.

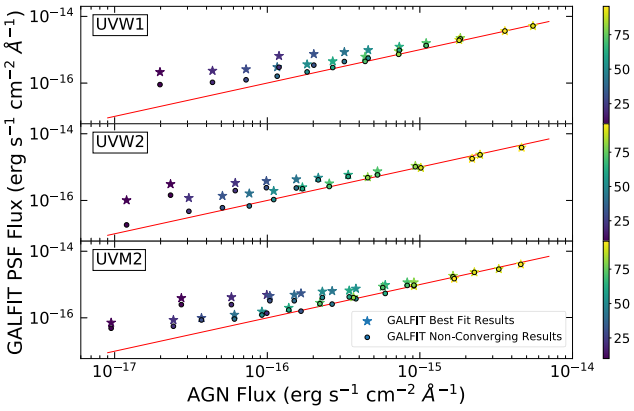

Fig. B.1. Comparing the simulated AGN (star) flux to the PSF flux estimated by GALFIT for the three UV filters. The star symbols show the best-fit results without a Sérsic profile, while the circle symbols show the results when the fitting with a Sérsic profile does not converge but we still get better constraints on the PSF profile compared to the fit without a Sérsic profile. The $x = y$ line is shown in red. The color bar indicates the AGN light ratio in percent.

In Figs. B.2, B.3, and B.4, we plot our results from the GALFIT analysis of these 270 simulated type I AGN for the UVW1, UVM2, and UVW2 filters, respectively. In each case, the plot on the left shows the AGN (PSF) flux estimated by GALFIT with respect to the actual flux of the star used as an AGN replica in these fake type I galaxies, while the plots on the right show the same information but segregated into different redshift bins. The symbols are color-coded based on the AGN to total light ratio. In general, the figures show a broad agreement between the AGN fluxes estimated by GALFIT and the actual star flux. However, significant deviations (up to 1 dex) appear at fluxes $< 10^{-15}$ erg cm^{-2} s^{-1} Å^{-1} and specifically for AGN light ratios below 80% in that flux regime. Deviations from the $x = y$ line (up to 0.3 dex) are also seen at the highest

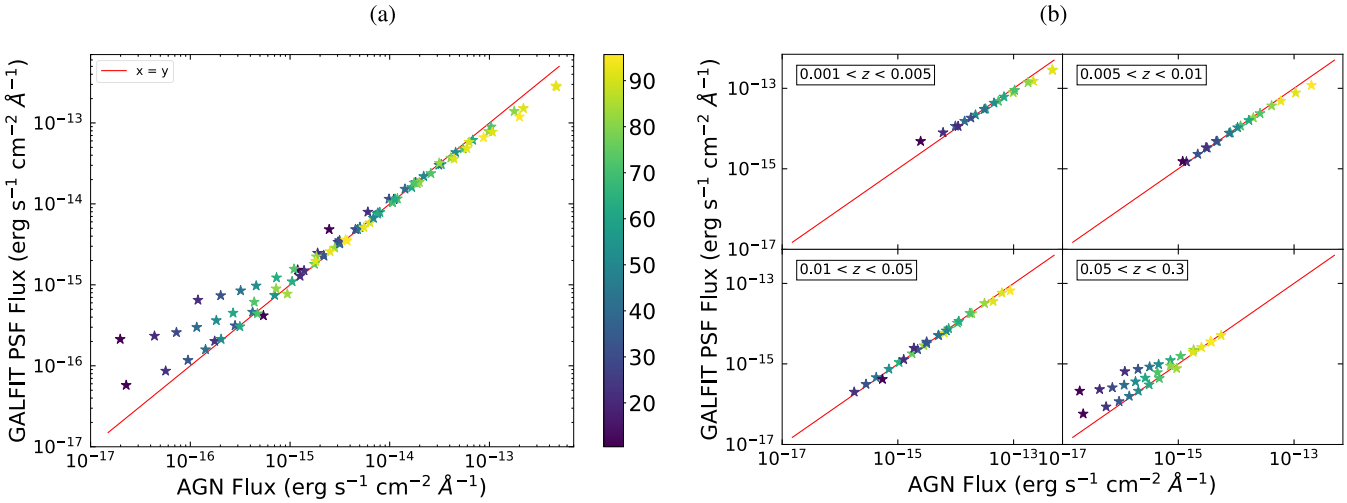

Fig. B.2. Comparison of the simulated AGN (star) flux to the PSF flux estimated by GALFIT in UVOT filter UVW1, for (a) all simulated AGN and (b) sources divided into different redshift bins. The $x = y$ line is shown in red. The color bar indicates the AGN light ratio in percent.

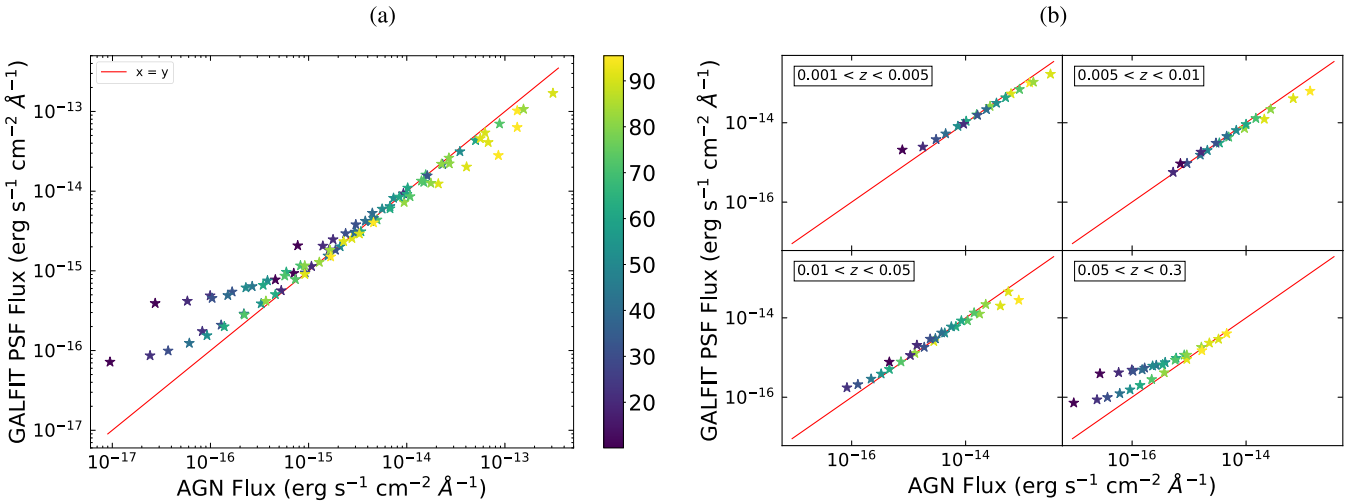

Fig. B.3. Comparison of the simulated AGN (star) flux to the PSF flux estimated by GALFIT in UVOT filter UVM2, for (a) all simulated AGN and (b) sources divided into different redshift bins. The $x = y$ line is shown in red. The color bar indicates the AGN light ratio in percent.

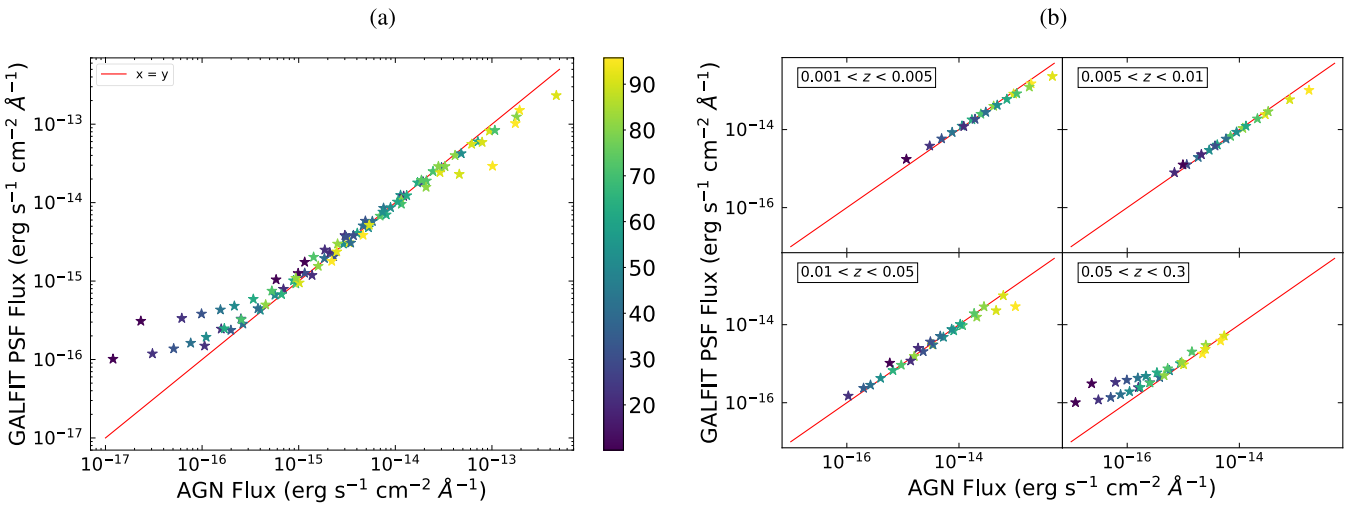

Fig. B.4. Comparison of the simulated AGN (star) flux to the PSF flux estimated by GALFIT in UVOT filter UVW2, for (a) all simulated AGN and (b) sources divided into different redshift bins. The $x = y$ line is shown in red. The color bar indicates the AGN light ratio in percent.

fluxes ($> 10^{-13}$ erg cm^{-2} s^{-1} Å^{-1}) and AGN light ratios around and above 90%. The differences at higher fluxes are more prominent for filters UVW2 and UVM2 as compared to the UVW1 filter. However, looking at the redshift-specific plots, it is evident that the large differences in the GALFIT estimates when compared to the star flux are restricted to the highest redshift range ($0.05 < z < 0.3$). On closer inspection, we found that these are, without exception, the sources for which GALFIT was not able to fit a Sérsic profile to the source, and the flux estimates are thereby from the sky + PSF fit only. This could be because of the very faint detection of the host galaxy at such large distances, the whole galaxy is pretty much undetected. The significant difference in the fluxes is therefore quite understandable, considering the fact that GALFIT tried to fit the host as well the AGN light at the center with only the PSF component, and hence gives much larger flux values for the AGN compared to the expected star's flux at the center. In the case of small deviations seen at the highest flux and AGN light ratios above 90%, in filters UVW2 and UVM2 for redshift range $0.01 < z < 0.05$, these cases again correspond to scenarios where GALFIT was not able to get reliable Sérsic fits for the source images. This could be because the AGN, in these cases, is responsible for most of the light coming from the galaxy, and hence the AGN flux is extremely high when compared to the host galaxy flux. As a result, GALFIT is not able to fit the host galaxy in the background of such a strong central AGN light source that dominates the entire galaxy. Therefore, we get GALFIT flux estimates that are lower than the actual AGN flux.

In Fig. B.5, we plot the simulated AGN flux versus the GALFIT estimated PSF flux for the three UV filters in different morphology classes. We have also included redshift information in these plots in the form of different symbols. At first look, based on these plots, it might seem like GALFIT works much better for edge-on galaxies as compared to the indeterminates and face-on galaxies in filters UVW1 and UVM2, and for filter UVW2, it works quite nicely for both edge-ons and face-ons. However, if we take a look at the redshift distribution in all these plots, it is abundantly clear that the differences in the flux estimates are strongly dependent on the redshift. The simulated edge-on galaxies of our test sample are all lying in the lower redshift bins and hence give good fit results. Whereas, the indeterminates belong to the highest redshift range. The few sources that show significant deviations from the $x = y$ line with face-on orientation are also part of the highest redshift bin.

Based on the results we obtained from these simulations in the UV filters, we repeat a similar analysis for the three *Swift*/UVOT optical filters but only in the highest redshift bin. This is a reasonable approach, considering that the sources in our sample are brighter in the optical compared to the UV (see Fig. B.6). And as the UV simulations show that it is only the faintest sources that the GALFIT-estimated magnitudes are not reliable, we calculate the optical corrections for the same set of sources ($z > 0.05$).

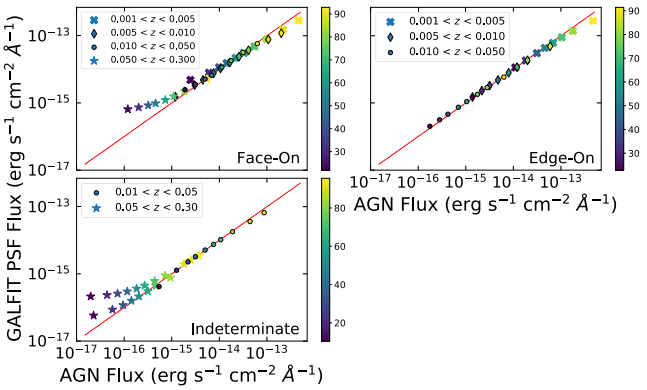

(a) UVW1

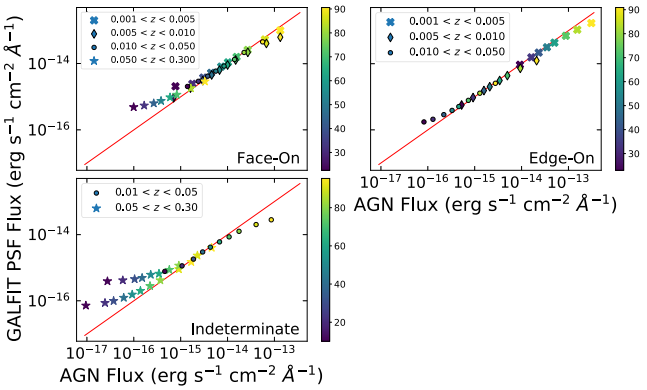

(b) UVM2

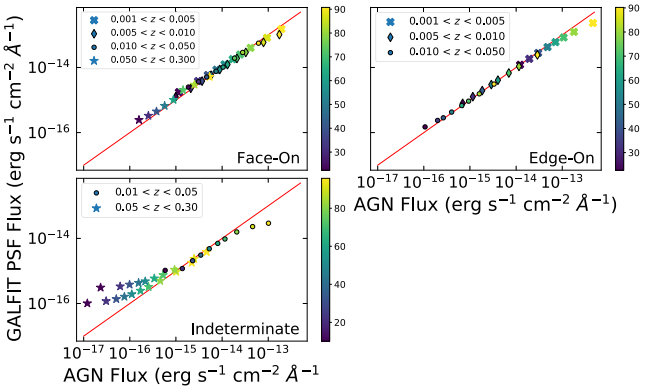

(c) UVW2

Fig. B.5. Comparison of the simulated AGN (star) flux to the PSF flux estimated by GALFIT for filters (a) UVW1, (b)UVM2, and (c) UVW2. The three subplots in each figure show the three different morphologies considered and the different symbols correspond to the redshift range. The $x = y$ line is shown in red. The color bar indicates the AGN light ratio in percent.

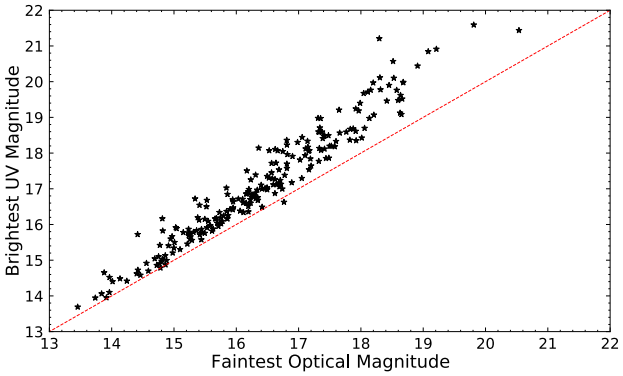

Fig. B.6. Source magnitudes in the faintest optical band against the brightest UV band. It is evident from this figure that the AGN in our sample are brighter in the optical when compared to the UV and even the faintest optical band is brighter than the brightest UV band. Therefore, based on the GALFIT simulations carried out in the UV band to obtain the correction factors for GALFIT-estimated PSF magnitudes and fluxes, only the faintest and farthest sources need to be corrected in the optical as well. The $x = y$ line is shown in red.

Appendix C: Comparison with HST

Thanks to ongoing follow-up observations of type I *Swift*/BAT AGN with optical HST imaging (as part of the optical campaign of BASS), we have high-quality HST images in filter F225W (similar to UVM2) for several sources in our sample (∼ 20). We select four sources (SWIFTJ0630.7+6342, SWIFTJ1535.9+5751, SWIFTJ1708.6+2155, and SWIFTJ1925.0+5041) that have HST observations in the F225W filter, contemporaneous with our *Swift*/UVOT observations. We fit the HST images with GALFIT following the procedure mentioned in Sect. 5.2 and extract their AGN flux to compare with those obtained from the *Swift*/UVOT images in the UV filter M2. Considering the high resolution of HST images with detailed and extended galaxy profiles, we focus on fitting just a small region around the nucleus to estimate the AGN flux. For all four sources, the magnitudes estimated from the HST images are within 0.1 mag of the ones from the UVOT images. This is acceptable, since the central wavelengths of the two filters are slightly different (F225W: 2371 Å and UVM2: 2246 Å). Therefore, we can conclude that the GALFIT-estimated AGN magnitudes for our *Swift*/UVOT images are consistent with those from the HST images. An effort to study AGN SEDs constructed using HST wide band optical imaging for type I *Swift*/BAT AGN (∼ 140) is ongoing.